AD-A086 698 GEORGIA INST OF TECH ATLANTA SCHOOL OF PHYSICS F/G 20/5
CROSS SECTIONS FOR IONIZATION OF RARE GAS EXCIMERS BY ELECTRON --ETC(U)
MAR 80 M R FLANNERY, K J MCCANN F33615-78-C-2028
UNCLASSIFIED AFWAL-TR-80-2015 NL

1 of 2
AD A086698

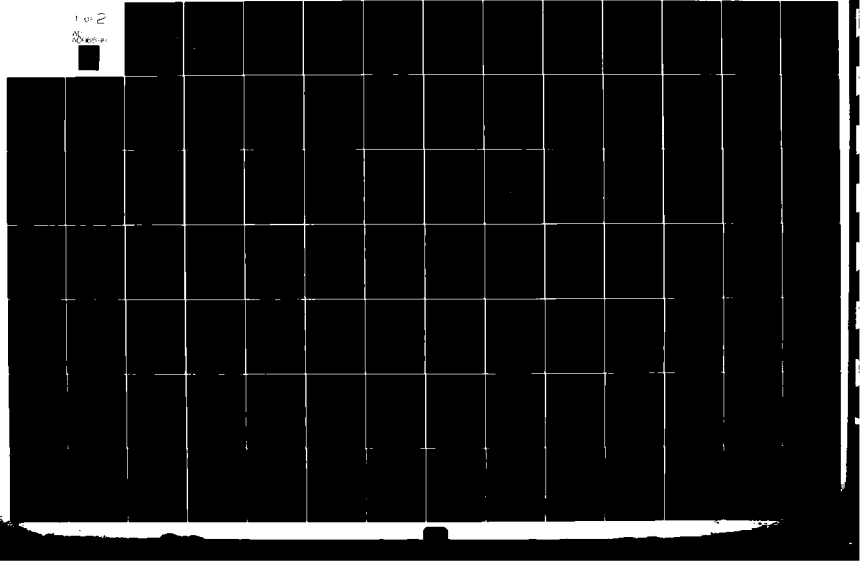

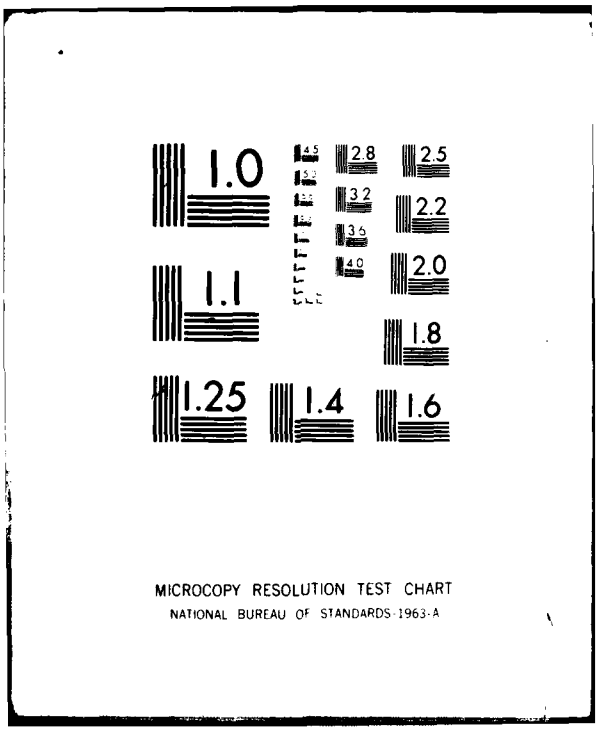
1.0
1.1
1.25
1.4
1.6
1.8
2.0
2.2
2.5
2.8
3.2
3.6
4.0
4.5
MICROCOPY RESOLUTION TEST CHART
NATIONAL BUREAU OF STANDARDS-1963-A

AFWAL-TR-80-2015

LEVEL II

CROSS SECTIONS FOR IONIZATION OF RARE GAS EXCIMERS BY ELECTRON IMPACT AND ATOMIC AND MOLECULAR PROCESSES IN EXCIMER LASERS

M. Raymond Flannery
K. J. McCann

School of Physics
Georgia Institute of Technology
Atlanta, Georgia 30332

March 1980

TECHNICAL REPORT AFWAL-TR-80-2015

Final Report for Period 1 April 1978 - 30 September 1979

Approved for public release; distribution unlimited.

AERO-PROPULSION LABORATORY
AIR FORCE WRIGHT AERONAUTICAL LABORATORIES
AIR FORCE SYSTEMS COMMAND
WRIGHT-PATTERSON AIR FORCE BASE, OHIO 45433

NOTICE

When Government drawings, specifications, or other data are used for any purpose other than in connection with a definitely related Government procurement operation, the United States Government thereby incurs no responsibility nor any obligation whatsoever; and the fact that the government may have formulated, furnished, or in any way supplied the said drawings, specifications, or other data, is not to be regarded by implication or otherwise as in any manner licensing the holder or any other person or corporation, or conveying any rights or permission to manufacture use, or sell any patented invention that may in any way be related thereto.

This report has been reviewed by the Office of Public Affairs (ASD/PA) and is releasable to the National Technical Information Service (NTIS). At NTIS, it will be available to the general public, including foreign nations.

This technical report has been reviewed and is approved for publication.

ALAN GARSCADDEN
Project Engineer

ROBERT R. BARTHELEMY
Chief, Energy Conversion Branch

FOR THE COMMANDER

JAMES D. REAMS
Chief, Aerospace Power Division
Aero Propulsion Laboratory

"If your address has changed, if you wish to be removed from our mailing list, or if the addressee is no longer employed by your organization please notify AFWAL/POOC, W-PAFB, OH 45433 to help us maintain a current mailing list".

Copies of this report should not be returned unless return is required by security considerations, contractual obligations, or notice on a specific document.

SECURITY CLASSIFICATION OF THIS PAGE (When Data Entered)

REPORT DOCUMENTATION PAGE

READ INSTRUCTIONS BEFORE COMPLETING FORM

1. REPORT NUMBER	2. GOVT ACCESSION NO.	3. RECIPIENT'S CATALOG NUMBER
AFWAL-TR-80-2015	AD-A086698	

4. TITLE (and Subtitle)

Cross Sections for Ionization of Rare Gas Excimers by Electron Impact and Atomic and Molecular Processes in Excimer Lasers.

5. TYPE OF REPORT & PERIOD COVERED: Final, 1 Apr 1978 – 30 Sep 1979

6. PERFORMING ORG. REPORT NUMBER

7. AUTHOR(s)

M. Raymond Flannery and K. J. McCann

8. CONTRACT OR GRANT NUMBER(s)

F33615-78-C-2028

9. PERFORMING ORGANIZATION NAME AND ADDRESS

School of Physics
Georgia Institute of Technology
Atlanta, Georgia 30332

10. PROGRAM ELEMENT, PROJECT, TASK AREA & WORK UNIT NUMBERS

11. CONTROLLING OFFICE NAME AND ADDRESS

Propulsion Laboratory
Air Force Wright Aeronautical Labs.
Air Force Systems Command
Wright Patterson Air Force Base, Ohio 45433

12. REPORT DATE: February 1980

13. NUMBER OF PAGES: 113

14. Monitoring Agency Name & Address

15. SECURITY CLASS. (of this report): Unclassified

15a. DECLASSIFICATION DOWNGRADING SCHEDULE

16. DISTRIBUTION STATEMENT (of this Report)

Approved for public release; distribution unlimited.

17. DISTRIBUTION STATEMENT (of the abstract entered in Block 20, if different from Report)

18. SUPPLEMENTARY NOTES

19. KEY WORDS (Continue on reverse side if necessary and identify by block number)

Cross sections, ionization, metastable rare gas excimers, atomic and molecular processes excimer lasers.

20. ABSTRACT (Continue on reverse side if necessary and identify by block number)

Theoretical cross sections for ionization of metastable excimers - helium, neon, argon, krypton and zenon - and of metastable mercury are presented. Systematic trends in inelastic form factors and Born cross sections for collisional transitions between excited neighboring levels of atoms are discovered and discussed. Key cycles of atomic and molecular collision processes in excimer lasers are delineated and discussed.

DD FORM 1 JAN 73 1473 EDITION OF 1 NOV 65 IS OBSOLETE

SECURITY CLASSIFICATION OF THIS PAGE (When Data Entered)

404227

PREFACE

This technical report was accomplished under Project 2301, Work Unit 2301-S2-19 "Calculation of Electron Impact Cross Sections from Metastable States in Atomic and Molecular Gases", by the School of Physics, Georgia Institute of Technology. The Air Force Monitor was Dr. Alan Garscadden. The research for this work was performed during the period April 1978 through September 1979.

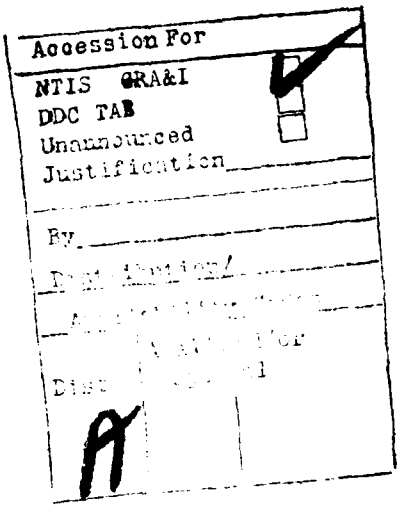

TABLE OF CONTENTS

Figure Captions

Figure 1. Radial Functions $R_\ell(r)$ in the single-center ℓ-expansion of the molecular orbital in He_2^*. The distance from the center-of-mass of the nuclei is r and the vertical line denotes position of nucleus from this center.

Figure 2. Radial Functions $R_\ell(r)$ in the single-center ℓ-expansion of the molecular orbital in Ne_2^*. The distance from the center-of-mass of the nuclei is r and the vertical line denotes position of nucleus from this center.

Figure 3. Radial Functions $R_\ell(r)$ in the single-center ℓ-expansion of the molecular orbital in Ar_2^*. The distance from the center-of-mass of the nuclei is r and the vertical line denotes position of nucleus from this center.

Figure 4. Radial Functions $R_\ell(r)$ in the single-center ℓ-expansion of the molecular orbital in Kr_2^*. The distance from the center-of-mass of the nuclei is r and the vertical line denotes position of nucleus from the center.

Figure 5. Radial Functions $R_\ell(r)$ in the single-center ℓ-expansion of the molecular orbital in Xe_2^*. The distance from the center-of-mass of the nuclei is r and the vertical line denotes position of nucleus from this center.

Figure 6. Normalized Distribution in speed of the orbital electron for metastable He_2^*. The corresponding distribution for the 2s electron of metastable He_2^* is shown for comparison.

Figure 7. Normalized Distribution in speed of the orbital electron for metastable Ne_2^*. The corresponding distribution for the 3s electron of metastable Ne_2^* is shown for comparison.

Figure 18. Cross sections ($\mathring{A}^2$) for ejection of the 6p, and the combined (6s + 6p) electrons from metastable mercury Hg^*.

Figure 19. Variation with final angular momentum ℓ' of the peak of the inelastic form factor unaveraged and averaged over ℓ for $10\ell \rightarrow 20\ell'$ transitions.

Figure 20. Cross section ($\mathring{A}^2$) for $10 \rightarrow 20$ transitions as a function of electron-impact energy E in units of the energy $\Delta\varepsilon$ of transition _____ Born approximation. --- Binary encounter approximation SQ.

Figure 21. Maximum form factors and maximum electron-impact cross sections for $10\ell \rightarrow 11\ell'$ transitions.

Figure 22. Maximum electron-impact cross section (averaged over initial ℓ-values for $10 \rightarrow 11\ell'$ transitions as a function of ℓ'.

Figure 23. The 10s and $11\ell'$ hydrogen radial orbitals $R_{n\ell}(r)$ times r in configuration space. Note inward shift of the $11\ell'$ orbital as ℓ' is increased. Large overlap is attained between 10s and 11s orbitals.

Figure 24. As in Figure 23. Maximum overlap is attained between 10s and $11(\ell' = 6$ and $7)$ orbitals. Variation of the spherical Bessel function $j_6(Kr)$ which modulates the 10s - $11(\ell' = 6)$ overlap is also illustrated.

Figure 25. Maximum cross sections (unaveraged and averaged over ℓ) for $10\ell \rightarrow 11\ell'$ transitions in H(1s) - $H(10\ell)$ collisions.

Figure 26. Potential energy curves relevant to the excimer Xe_2^* system (adapted from Ermler et al.[27]).

Figure 27. Schematic diagram of potential-energy curves relevant to the rare gas (Rg)-halide ($H\ell$) systems.

Figure 28. Dominant Mechanisms for production and quenching of ArF^* in a typical $\vec{e}$-beam excited two-component rare gas-halide system at pressures (1-4) atm.

Figure 29. Cross sections for photodetachment of halide negative-ions (adapted by Ewing[24] from Mandl[35] and Roth[36]).

Figure 30. Photoabsorption cross sections of positive molecular ions Ne_2^+ Ar_2^+, Kr_2^+ and Xe_2^+ (adapted by Ewing[24] from Wadt and Hay[37]).

Figure 31. Cross sections for photoionization of metastable rare gas atoms Ne^*, Ar^*, Kr^* and Xe^* (after McCann and Flannery[38]).

Figure 32. Cross sections for photoionization of the $^1\Sigma_u^+$ state of Ar_2^* (after Resigno et al.[39]).

Figure 33. Dominant Mechanisms for KrF^* formation in $\vec{e}$-beam excited mixture (Ar > 90%/Kr < 10%/$F_2 \sim 0.2\%$) at pressures (1-4) atm.

Figure 34. Schematic diagram illustrating vibrational relaxation and excitation with displacement reactions (after Flannery and Winter[40]).

Figure 35. Dominant Mechanisms for KrF^* quenching in $\vec{e}$-beam excited mixtures ($Ar/Kr/F_2$) at pressures (1-4) atm.

Figure 36. Schematic diagram illustrating the mechanism of ion-ion recombination into ArF^* and mutual neutralization to Ar^* + F occurring in a gas.

Figure 37. Three-body ion-ion recombination coefficients $\alpha(cm^3\ S^{-1})$ for $Ar^+ + Y^- + Ar \rightarrow ArY^* + Ar$, ($Y^- \equiv F^-, C\ell^-, Br^-, I^-$), as a function of neutral-gas density N (in units of Loschmidt's number $N_L = 2.69 \times 10^{19}$ cm^{-3}). Negative ion denoted in each curve (after Flannery[29]).

Figure 38. Ionic recombination coefficients $\alpha(cm^3\ sec^{-1})$ for the processes $X^+ + F^- + X \rightarrow XF^* + X$(X ≡ He, Ne, Ar, Kr, Xe) as a function of neutral-gas density N (in units of Loschmidt's number N_L, (2.69×10^{19} cm^{-3}). Gas X as indicated on each curve. Note the rates for the He case have been divided by 1.6. (After Flannery and Yang [30]).

Figure 39. Ionic recombination coefficients $\alpha(cm^3\ sec^{-1})$ for the processes $X_2^+ + F^- + X \rightarrow [X_2F]^* + X$ ($X \equiv$ He, Ne, Ar, Kr, Xe) as a function of neutral-gas density N (in units of Loschmidt's number N_L, $2.69 \times 10^{19}\ cm^{-3}$). The square brackets indicate that the molecule $[X_2F]^*$ may not remain bound. Gas X is as indicated on each curve. Note the rates for the He case have been divided by 1.5. (After Flannery and Yang[31]).

Figure 40. Ionic recombination coefficients $\alpha(cm^3\ sec^{-1})$ at 300 K for $Kr^+ + F^- + M \rightarrow KrF^* + M$ ($M \equiv$ He, Ne, Ar, Kr, Xe) as a function of neutral-gas density N, in units of Loschmidt's number 2.69×10 cm^{-3}. Buffer gas M as indicated on each curve. (After Flannery and Yang[32]).

Figure 41. As in Fig. 15 except for the process $Kr_2^+ + F^- + M \rightarrow [Kr_2^+ F^-]^* + M$, where the brackets indicate that the product molecule may not remain bound. (After Flannery and Yang[32]).

Figure 42. Atomic and Molecular processes important in the formation and destruction of rare gas excimers.

Figure 43. Cross sections ($10^{-16}\ cm^2$) for collisional ionization of metastable (a) Ne^*, (b) Ar^*, (c) Kr^*, and (d) Xe^* by electrons with impact energy E (eV). BF and BH are Born results for outer-shell ionization obtained from integrations over the full and lower-half ranges of energy ε of the ejected electron. The binary encounter (quantal distribution) cross sections are denoted by BE0 for outer-shell ionization, by BE1 for ionization of one of the electrons in the np^5 shell, by BE5 for the total ionization os the np^5 shell and by BE for the sum of BE0 and BE5. Previous binary encounter (exponential distribution) results of Vriens[53] are represented by

V. ●: measurements of Dixon, Harrison, and Smith[54]. (After Ton-That and Flannery[41]).

Figure 44. Cross sections for electron impact ionization of metastable ($^{1,3}\Sigma$) excimer states of Ne_2^*, and of the atomic metastable level. (After McCann, Flannery and Hazi[55]).

Figure 45. As in Fig. 19 except for Ar_2^* and Ar^* (after McCann, Flannery and Hazi[55]).

Figure 46. As in Fig. 20 except for Xe_2^* and Xe^* (after Flannery and McCann[56]).

Tables

SECTION I

INTRODUCTION

This report describes theoretical research and results obtained from theoretical treatments of electron-impact ionization of atoms and molecules initially in their metastable states. The research described here was conducted under the auspices of USAF contract F33615-78-C-2028. While this report is complete in itself, a previous report AFAPL-TR-78-58 by M. R. Flannery provides full detailed coverage of our previous research on development and applications of theoretical descriptions of cross sections for collisions involving atoms and molecules initially in excited states.

Electron-excited atom and electron-excited molecule collisions play key roles in the kinetics of excimer such as Xe_2^* and exciplex such as KrF^* and XeF^* laser systems as well as in various types of gas discharges. They are also of fundamental significance in their own right in that they raise new and interesting questions not encountered in collisions involving species initially in their ground-states. Not only does this research field offer new and exciting possibilities for further basic theoretical developments and explorations of new issues and systematic trends that might emerge but also it provides a variety of examples for which validity criterion of specific theoretical descriptions (such as the binary encounter and impulse approximations) becomes better satisfied as the valence electron in the excited atoms or molecule becomes more excited i.e., more loosely bound to its parent ion.

In this report we shall describe our theoretical work on electron-excimer collisions, on new systematic trends noted for $n\ell \rightarrow (n+1)\ell'$ collisional excitation and our delineation and discussion of atomic and molecular collision processes in rare-gas excimer and in rare gas-halide laser systems.

SECTION II

SUMMARY OF THEORETICAL WORK PERFORMED

The following four distinct theoretical research topics were investigated:

(1) Electron-impact cross sections for ionization of metastable rare gas excimers $Rg_2^*(\equiv He_2^*, Ne_2^*, Ar_2^*, Kr_2^*, Xe_2^*)$,

$$\vec{e} + Rg_2^*(^{1,3}\Sigma_u^+) \rightarrow \vec{e} + Rg_2^+(^2\Sigma_u^+) + e \qquad (1)$$

(2) Electron-impact ionization cross sections for e-metastable Hg^* collisions,

$$e + Hg(6s\ [^2S]\ 6p\ [^3p]) \rightarrow \begin{cases} \vec{e} + Hg^+(^2S) + e \\ \vec{e} + Hg^+(5d^{10}6p) + e \end{cases} \qquad (2)$$

(3) Trends in inelastic form factors and Born cross sections for $n\ell - (n+1)\ell'$ collisional transitions, and

(4) Atomic and Molecular Collision Processes in rare gas-halide lasers and in rare-gas excimer lasers.

In topic (1) cross sections for the ionization of the metastable excimers He_2^*, Ne_2^*, Ar_2^*, Kr_2^* and Xe_2^* in $^{1,3}\Sigma_u^+$ states by electron impact are calculated in the binary-encounter approximation for collision energies E(eV) in the range $5 \leq E \leq 50$ eV. They have maximum values $\sim 10^{-15}$ cm^2 at ~ 10 eV collision energy and are within 50% higher than the cross sections for ionization of the corresponding metastable atomic states. Two-center molecular wavefunctions were required.

In topic (2) the ionization cross sections were determined from the binary encounter approximation.

In topic (3), various patterns were discovered for collisional transitions between neighboring excited levels. As ℓ' is varied for $n\ell - (n+1)\ell'$ collisional transitions, two distinct peaks are noted in both the inelastic form factor and in the Born cross section for e-excited atom collisions. These peaks merge into one peak at high ℓ. The cross sections for $n\ell \rightarrow (n+1)\ell'$ transitions in neutral-neutral transitions, however, are found to display an overall increase as ℓ' is varied from 0 to $(n'-1)$. These patterns and their origin are quite different to those given previously in our report AFAPL-TR-78-58 for $n\ell \rightarrow n'\ell'$ transitions with $n' >> n$.

In topic (4) the key cycles of atomic and molecular collision processes contributing to the formation and quenching of the excited molecular states in exciplex (such as KrF^*) and excimer (such as Xe_2^*) laser systems are delineated and discussed.

SECTION III

THEORETICAL CROSS SECTIONS FOR IONIZATION OF METASTABLE RARE GAS EXCIMERS He_2^*, Ne_2^*, Ar_2^*, Kr_2^* and Xe_2^* BY ELECTRON-IMPACT

Information on ionization of rare gases initially in atomic and molecular metastable states is very important in the kinetic modeling of excimer lasers (see Section VI and references therein). While cross sections for collision processes involving ground-state species are in general fairly well documented,[1,2] relatively little is known about electron-collision processes involving atoms and molecules initially in excited states. In a previous report (AFAPL-TR-78-58) we presented theory and calculated cross sections for ionization of the metastable atomic rare-gas systems (He^*, Ne^*, Ar^*, Kr^*, and Xe^*) by electron-impact. In this present report we investigate cross sections for ionization of the metastable rare-gas excimers ($Rg_2^* \equiv He_2^*$, Ne_2^*, Ar_2^*, Kr_2^* and Xe_2^*).

$$\vec{e} + Rg_2^*(^{1,3}\Sigma_u^+) \rightarrow \vec{e} + Rg_2^+(^2\Sigma_u^+) + e \qquad (1)$$

as a function of impact energy E of the incident electron and explore any similarity the calculated cross sections bear to those for the corresponding atomic cases previously reported.

3.1 Theoretical Method

As demonstrated by direct calculation of the electronic orbitals for the excimer systems, the excited electron in the $^{1,3}\Sigma_u^+$ molecular states in process (1) behaves very similar to a Rydberg electron attached to its parent $^2\Sigma_u^+$ ion, with a binding energy I $\sim$ 3-4 eV. The situation therefore fulfills the essential criteria for validity of the binary-encounter method[3-5] in which specific account is taken of the distribution in speed of the valence electron. The method assumes that ionization is achieved via a binary collision between

the incident electron and the electron bound to its parent nucleus with energy I. When the energy transferred to the bound electron is greater than I, then detachment occurs. The two nuclei are ignored except insofar as they generate a velocity distribution $f_n(u)$ for the molecular electron bound initially in quantum state n. In this approximation, the cross section (with all quantities in atomic units) for ejection of this Rydberg electron by collision with an incident electron of speed v is[3-5]

$$\sigma_n^I(E) = \frac{4\pi a_o^2}{3v^2} \int_I^E d\varepsilon \int_o^\infty \frac{f_n(u)}{u} \left[\frac{1}{P_-^3} - \frac{1}{P_+^3} \right] du \qquad (2)$$

The distribution in speed u of the Rydberg electron described by a molecular orbital $\phi_{n\lambda}(\underset{\sim}{r})$ is,

$$f_n(u) = \frac{1}{(2-\delta_{o|\lambda|})} \sum_\lambda \int \left| \frac{1}{(2\pi)^{3/2}} \int \phi_{n\lambda}(\underset{\sim}{r}) \exp(-i\underset{\sim}{u}\cdot\underset{\sim}{r}) \, d\underset{\sim}{r} \right|^2 u^2 \, d\hat{\underset{\sim}{u}} \qquad (3)$$

where the sum runs over the degenerate components of $\phi_{n\lambda}$ (λ = o for a σ orbital, $\lambda = \pm 1$ for π etc.), and δ_{ij} is the Kroenecker-δ symbol.

For a specified energy transfer ε to the Rydberg electron, the limits to the momentum change are

$$P^- = \max [|u'-u|, |v'-v|], \quad v' = (v^2-2\varepsilon)^{1/2} \qquad (4)$$

and

$$P^+ = \min [(u'+u), (v'+v)], \quad u' = (u^2+2\varepsilon)^{1/2} \qquad (5)$$

where u' and v' are the postcollision speeds of the two particles. Eq. (2) with the aid of (4) and (5) can be rewritten in terms of analytical differential

cross sections $\partial\sigma_n^I / \partial\varepsilon$ for energy changes ε between fixed limits specified by v and u.

One powerful advantage of the binary-encounter approach is that it inherently includes an infintie number of partial waves for the angular momentum ℓ' of the ejected electron in (1). Ionization from excited states is apparently characterized (cf Report AFAPL-TR-78-58) by contributions arising from many angular momentum states of the ejected electron.

3.2 Single Center Expansions of the Molecular Valence Orbital in Metastable Rare-Gas Excimers

The molecular orbitals were obtained with the aid of standard molecular computer codes at the Lawrence Livermore Laboratory (LLL). With the help of Dr. A. Hazi of LLL, the molecular orbitals of Ne_2^* and Ar_2^* were determined by performing separate self-consistent-field (SCF) calculations on the $^1\Sigma_u^+$ and $^3\Sigma_u^+$ excimer states. All electrons were treated explicitly. The molecular orbitals were expanded in two-center contracted Gaussian-type functions.[6] For both Ne_2^* and Ar_2^*, the basis set included several diffuse functions to describe correctly the spatial distribution of the Rydberg electron. The choice of basis functions was optimized by Hazi, Resigno and Orel in earlier studies[7,8] of the photoionization of Ne_2^* and Ar_2^*.

The molecular orbitals for He_2^*, Kr_2^* and Xe_2^* were obtained with the help of Dr. N. Winter of LLL who ran the molecular code he previously used, with Ermler, Lee and Pitzer,[9] in his investigation of potential energy curves for Xe_2, Xe_2^+, and Xe_2^*. Here the $6s\sigma_g$ Rydberg orbital for Xe_2^* was computed by the SCF approximation which included spin-orbit coupling effects.

The required orbitals for He_2^*, Ne_2^*, Ar_2^*, Kr_2^* and Xe_2^* could be conveniently

written as,

$$\Psi(\underset{\sim}{R}_A, \underset{\sim}{R}_B) = \sum_{i=1}^{N} C_i \sum_{j=1}^{M_i} \beta_{ji} F(K_i, \underset{\sim}{R}_A, \underset{\sim}{R}_B, \alpha_{ji}) \tag{6}$$

Where $\underset{\sim}{R}_A$ and $\underset{\sim}{R}_B$ are the position vectors of the valence electron from nuclei A and B respectively and tables of N, C_i, M_i, β_{ji}, and α_{ji} can be provided for each system. The label $K_i \equiv 1\text{-}4$ characterized the type of functions F used. These functions are defined by,

$$F(1, \underset{\sim}{R}_A, \underset{\sim}{R}_B, \alpha) = \left(\frac{2\alpha}{\pi}\right)^{3/4} [\exp(-\alpha R_A^2) + \exp(-\alpha R_B^2)] \tag{7a}$$

$$F(2, \underset{\sim}{R}_A, \underset{\sim}{R}_B, \alpha) = 2\alpha^{1/2} \left(\frac{2\alpha}{\pi}\right)^{3/4} [Z_A \exp(-\alpha R_A^2) - Z_B \exp(-\alpha R_B^2)] \tag{7b}$$

$$F(3, \underset{\sim}{R}_A, \underset{\sim}{R}_B, \alpha) = \frac{\alpha}{3^{1/2}} \left(\frac{2\alpha}{\pi}\right)^{3/4} [Z_A^2 \exp(-\alpha R_A^2) + Z_B^2 \exp(-\alpha R_B^2)] \tag{7c}$$

$$F(4, \underset{\sim}{R}_A, \underset{\sim}{R}_B, \alpha) = \frac{\alpha}{3^{1/2}} \left(\frac{2\alpha}{\pi}\right)^{3/4} [(X_A^2+Y_A^2) \exp(-\alpha R_A^2) + (X_B^2+Y_B^2) \exp(-\alpha R_B^2)] \tag{7d}$$

where the components of $\underset{\sim}{R}_A$ and $\underset{\sim}{R}_B$ along the internuclear direction of $\hat{\underset{\sim}{k}}$ are

$$Z_A = \underset{\sim}{R}_A \cdot \hat{\underset{\sim}{k}}, \quad Z_B = \underset{\sim}{R}_B \cdot \hat{\underset{\sim}{k}} \tag{8}$$

and are

$$X_A^2 + Y_A^2 = X_B^2 + Y_B^2 = R^2 \sin^2 \alpha, \tag{9}$$

perpendicular to $\hat{\underset{\sim}{k}}$, where γ is the angle between $\hat{\underset{\sim}{k}}$ and the vector $\underset{\sim}{R}$ joining the mid point of the nuclei to the valence electron. The parameters in (6) for the orbitals of He_2^*, Ne_2^*, Ar_2^*, Kr_2^* and Xe_2^* are presented in Tables 1-5, respectively.

In order to obtain the speed distributions, it proves convenient to express the two-center molecular wave function by a single center expansion,

$$\Psi(\underset{\sim}{R}_A, \underset{\sim}{R}_B) \equiv \phi_{n\sigma_g}(\underset{\sim}{R}) = \sum_{\ell=0}^{\infty} R_\ell(R)\, Y_{\ell o}(\hat{\underset{\sim}{R}}) \,, \quad n = 2\text{-}6 \ (He_2^* - Xe_2^*) \qquad (10)$$

where $\underset{\sim}{R}$ is the position vector of the Rydberg electron relative to the center of mass of the nuclei and the Z axis is directed along the internuclear axis. The radial functions R_ℓ obtained by this procedure are displayed in Figs. 1-5 which also shows the number of angular momentum states ℓ required to obtain convergence of (10).

3.3 Velocity Distributions of the Valence Electron in the Metastable Rare Gas Excimers ($He_2^* - Xe_2^*$)

The plane wave in (3) for the distribution $f_n(u)$ in speed u of the valence electron is expanded in terms of the spherical Bessel functions j_ℓ (ur) such that, after some analysis, the distribution is given by

$$f_{n\sigma_g}(u) = \frac{2u^2}{\pi} \sum_{\ell=0}^{\infty} \left| \int R_\ell(r)\, j_\ell(ur)\, r^2\, dr \right|^2 \qquad (11)$$

in terms of the single-center radial functions R_ℓ previously determined. In Figures 6-10 are displayed the distributions obtained from (10) and (11) for the rare-gas excimers $He_2^* - Xe_2^*$, respectively together with the distributions for the corresponding atomic cases $He^* - Xe^*$ where the orbitals used are those previously calculated by Ton-That and Flannery[3,10] in the previous report (AFAPL-TR-78-58).

The close agreement between the atomic and molecular distributions in Figures 6-10 simply reflects the Rydberg nature of the molecular orbital in the passive effect of each ionic core. The distributions (11) are automatically normalized to unity.

3.4 Final Results: Cross Sections for Electron-Impact Ionization of He_2^*, Ne_2^*, Ar_2^*, Kr_2^* and Xe_2^*

With knowledge of the speed distributions $f_n(u)$ the cross sections for the ionization process

$$\vec{e} + Rg_2^*(^{1,3}\Sigma_u^+) \rightarrow \vec{e} + Rg_2^+(^2\Sigma_u^+) + e \qquad (12)$$

can now be calculated as a function of impact energy from (2). The results are displayed in Figures 11-12 together with the Born cross section previously presented by Ton-That and Flannery in AFAPL-TR-78-58 for the corresponding atomic cases. The difference between the singlet and triplet cross sections in the figures originates entirely from the use in (2) of the different ionization potentials used. The cross sections $\sim 10^{-15}$ cm^2 increase with the complexity of the molecule and are in general within 40% higher than those for the corresponding atomic cases. So that the numerical cross sections be available for current laser-modeling and other programs, they are presented in Tables 6-8, together with the ionization potentials used in the calculations. The results for ionization of Ne_2^* and Ar_2^* have been recently published.[11]

Table 1

Electronic Orbital for the valence electron in metastable $He_2^*(^{1,3}\Sigma_u)$

i	j	K_i	α_{ji}	β_{ji}	C_i $^3\Sigma_u^+$	$^1\Sigma_u^+$
1	1	1	3293.6940	0.0001302	0.11165738	0.06073677
	2		488.8941	0.0010407		
	3		108.7720	0.0055930		
	4		30.1799	0.0241518		
	5		9.7891	0.0843609		
	6		3.5223	0.2600227		
	7		1.3524	0.4254755		
	8		0.5526	0.2512518		
	9		0.2409	0.1013753		
2	1	1	0.1079	1.0000000	0.16829577	0.20719604
3	1	1	0.0484	1.0000000	-0.19033779	-0.16317527
4	1	1	0.0217	1.0000000	-0.36421326	-0.41626502
5	1	2	1.5535	0.0205437	0.11802755	0.10639929
	2		0.3689	0.1656448		
	3		0.1192	0.8737556		
6	1	2	0.0449	1.0000000	-0.05478556	-0.05786859
7	1	2	0.0181	1.0000000	0.01833678	0.03859296
8	1	2	0.0073	1.0000000	0.00225434	-0.01405507
9	1	3	0.1800	1.0000000	-0.01068116	-0.01246813
10	1	4	0.1800	1.0000000	-0.07168301	-0.06675153

Table 2

Electronic Orbital for the valence electron in metastable $Ne_2^*(^{1,3}\Sigma_u)$.

i	j	K_i	α_{ji}	β_{ji}	C_i $^3\Sigma_u^+$	$^1\Sigma_u^+$
1	1	1	12100.0000	0.00120062	-0.0084119	-0.0056962
	2		1821.0000	0.00909401		
	3		432.8000	0.0413149		
	4		132.5000	0.137896		
	5		43.7700	0.362521		
	6		14.9100	0.472652		
	7		5.1270	0.130104		
	8		1.4910	-0.00225459		
2	1	1	12100.0000	-0.000280643	-0.1399576	-0.1188644
	2		1821.0000	-0.000216535		
	3		432.8000	-0.00977813		
	4		132.5000	-0.0353536		
	5		43.7700	-0.101423		
	6		14.9100	-0.207498		
	7		5.1270	-0.198026		
	8		1.4910	0.616139		
3	1	1	0.4468	1.0000000	-0.1300185	-0.1264780
4	1	1	0.0300	1.0000000	0.5788887	0.5964727
5	1	2	56.4500	0.0163096	0.0109995	-0.0033568
	2		12.9200	0.101669		
	3		3.8650	0.309059		
	4		1.2030	0.486447		
6	1	2	0.3444	1.0000000	0.0172090	0.0139787
7	1	2	0.0300	1.0000000	-0.0286067	-0.0229103
8	1	3	1.0000	1.0000000	-0.0040991	-0.0014983
9	1	1	0.2000	1.0000000	-0.0401757	-0.0383726
10	1	1	0.1000	1.0000000	-0.0270155	-0.0537932
11	1	2	0.1500	1.0000000	-0.0195532	-0.0171475

Table 3

Electronic Orbital for the valence electron in metastable $Ar_2^*(^{1,3}\Sigma_u)$.

i	j	K_i	α_{ji}	β_{ji}	C_i $^3\Sigma_u^+$	$^1\Sigma_u^+$
1	1	1	45654.0780	0.0010040	0.0005458	0.0001792
	2		6913.2678	0.0076021		
	3		1594.6573	0.0377288		
	4		457.3085	0.1372590		
	5		151.2192	0.3398540		
	6		55.9809	0.4355440		
	7		22.6253	0.1829890		
	8		7.1177	0.0105959		
	9		2.8287	-0.0011900		
	10		0.6334	0.0002980		
2	1	1	45654.0780	-0.0002843	0.0077017	-0.0034920
	2		6913.2678	-0.0021806		
	3		1594.6573	-0.0108579		
	4		457.3085	-0.0423726		
	5		151.2192	-0.1171760		
	6		55.9809	-0.2232860		
	7		22.6253	-0.0881448		
	8		7.1177	0.5595790		
	9		2.8287	0.5596220		
	10		0.6334	0.0360076		
3	1	1	45654.0780	0.0000890	0.1602136	-0.1401930
	2		6913.2678	0.0006786		
	3		1594.6573	0.0034139		
	4		457.3085	0.0132248		
	5		151.2192	0.0377956		
	6		55.9809	0.0721420		
	7		22.6253	0.0354576		
	8		7.1177	-0.2632880		
	9		2.8287	-0.3892130		
	10		0.6334	0.6784510		
4	1	1	0.2252	1.0000000	0.2700172	-0.2700771
5	1	1	0.0300	1.0000000	-1.0228201	1.0689500
6	1	2	268.7843	0.0135690	0.0005141	-0.0009674
	2		63.2144	0.0921681		
	3		19.9486	0.3068230		
	4		7.1087	0.4943400		
	5		2.7159	0.2804000		
	6		0.7635	0.0187786		
7	1	2	268.7843	-0.0037565	-0.0107419	-0.0080215
	2		63.2144	-0.0270096		
	3		19.9486	-0.0890523		
	4		7.1087	-0.1702800		
	5		2.7159	-0.0098684		
	6		0.7635	0.5631230		
8	1	2	0.2199	1.0000000	-0.0314933	0.0217787
9	1	2	0.0300	1.0000000	0.0352061	-0.0323465
10	1	3	1.0000	1.0000000	0.0096517	-0.0022985
11	1	1	0.1100	1.0000000	-0.2862100	0.3114807
12	1	1	0.0600	1.0000000	0.7114175	-0.7893349
13	1	2	0.1200	1.0000000	0.0199821	-0.0162383

Table 4

Electronic Orbital for the valence electron in metastable $Kr_2^*(^{1,3}\Sigma_u)$.

i	j	K_i	α_{ji}	β_{ji}	C_i $^3\Sigma_u^+$	$^1\Sigma_u^+$
1	1	1	35.1068	0.0047955	0.1165028	0.10253346
	2		2.7118	-0.4116402		
	3		0.4445	1.1811298		
2	1	1	0.1688	1.0000000	0.23331595	0.21164104
3	1	1	0.0550	1.0000000	0.11694121	0.16783456
4	1	1	0.0210	1.0000000	-0.66783485	-0.70048389
5	1	2	5.0493	-0.0832837	0.01753630	-0.0019190236
	2		0.5916	1.0213091		
6	1	2	0.1789	1.0000000	0.03061054	0.018123645
7	1	2	0.0360	1.0000000	-0.04031849	-0.045317967
8	1	2	0.0130	1.0000000	-0.00506482	0.00073613396
9	1	4	0.2200	1.0000000	-0.03280175	-0.028788417
10	1	3	0.2200	1.0000000	-0.01311801	-0.0026323942

Table 5

Electronic Orbital for the valence electron in metastable $Xe_2^*(^{1,3}\Sigma_u)$.

i	j	K_i	α_{ji}	β_{ji}	C_i $^3\Sigma_u^+$	$^1\Sigma_u^+$
1	1	1	28.7387	-0.015324	-0.16647072	-0.14387856
	2		1.9610	-0.192789		
	3		3.1852	1.099335		
2	1	1	0.1233	1.000000	-0.31590548	-0.26703023
3	1	1	0.0550	1.000000	-0.056094811	-0.15197290
4	1	1	0.0210	1.000000	0.66977637	0.72422827
5	1	2	2.8215	0.084105	-0.021755781	0.0023202384
	2		0.4358	0.0964806		
6	1	2	0.1372	1.000000	-0.035230628	-0.027882492
7	1	2	0.0360	1.000000	0.044257355	0.045215175
8	1	2	0.0130	1.000000	0.0019109689	0.0011055573
9	1	3	0.2200	1.000000	0.026441233	0.015451513
10	1	4	0.2200	1.000000	0.056381921	0.048010370

Table 6

Cross sections ($\mathring{A}^2$) for collisional ionization of metastable $He_2^*(2^{1,3}\Sigma_u^+)$ by electrons of energy E(eV). Ionization energy is I. E. (eV).

E(eV)	$^3\Sigma_u^+$	$^1\Sigma_u^+$
5	2.79	4.00
6	5.40	6.62
7	6.79	7.93
8	7.46	8.52
9	7.76	8.75
10	7.86	8.79
12	7.77	8.60
14	7.53	8.28
16	7.23	7.92
18	6.92	7.56
20	6.62	7.22
25	5.92	6.43
30	5.32	5.76
35	4.81	5.20
40	4.38	4.73
45	4.01	4.32
50	3.69	3.98
I.E.(eV)	4.108	3.901

Table 7

Cross sections ($\mathring{A}^2$) for collisional ionization of metastable $Ne_2^*(^{1,3}\Sigma_u^+)$ and $Ar_2^*(^{1,3}\Sigma_u^+)$ by electrons of energy E(eV). Ionization energy is I. E. (eV).

	Ne_2^*		Ar_2^*	
E(eV)	$^3\Sigma_u^+$	$^1\Sigma_u^+$	$^3\Sigma_u^+$	$^1\Sigma_u^+$
5	4.47	4.97	9.89	10.76
6	7.23	7.72	12.04	12.85
7	8.58	9.04	13.02	13.79
8	9.18	9.60	13.47	14.20
9	9.40	9.80	13.62	14.31
10	9.44	9.81	13.58	14.24
12	9.24	9.58	13.16	13.75
14	8.89	9.19	12.51	13.04
16	8.49	8.76	11.81	12.30
18	8.07	8.33	11.13	11.57
20	7.67	7.91	10.49	10.90
25	6.78	6.98	9.11	9.45
30	6.04	6.21	8.00	8.29
35	5.43	5.58	7.11	7.36
40	4.93	5.06	6.37	6.59
45	4.50	4.62	5.76	5.96
50	4.14	4.25	5.25	5.43
I.E.(eV)	3.85	3.78	3.23	3.15

Table 8

Cross sections ($\mathring{A}^2$) for collisional ionization of metastable $Kr_2^*(^{1,3}\Sigma_u^+)$ and $Xe_2^*(^{1,3}\Sigma_u^+)$ by electrons of energy E(eV). Ionization energy is I. E. (eV).

	$Q(\mathring{A}^2)$			
	Kr_2^*		Xe_2^*	
E(eV)	$^3\Sigma_u^+$	$^1\Sigma_u^+$	$^3\Sigma_u^+$	$^1\Sigma_u^+$
5	11.21	12.48	12.87	14.58
6	13.05	14.25	14.54	16.12
7	13.94	15.09	15.18	16.65
8	14.37	15.46	15.35	16.73
9	14.51	15.55	15.26	16.56
10	14.48	15.47	15.03	16.25
12	14.10	15.00	14.35	15.45
14	13.52	14.35	13.59	14.58
16	12.89	13.65	12.83	13.74
18	12.24	12.95	12.11	12.95
20	11.61	12.27	11.45	12.23
25	10.19	10.74	10.06	10.72
30	8.98	9.46	8.96	9.54
35	7.98	8.39	8.09	8.61
40	7.15	7.51	7.37	7.84
45	6.46	6.79	6.78	7.21
50	5.88	6.18	6.28	6.68
I.E.(eV)	3.04	2.94	2.96	2.84

SECTION IV

THEORETICAL CROSS SECTIONS FOR IONIZATION IN ELECTRON-METASTABLE Hg^* COLLISIONS

The binary encounter treatment outlined in the previous section is now applied to examination of the ionization process

$$\vec{e} + Hg(6s\ [^2S]\ 6p\ [^3P]) \rightarrow \begin{cases} \vec{e} + Hg^+(^2S) + e \\ \vec{e} + Hg^+(5d^{10}6p) + e \end{cases} \qquad (1)$$

as a function of electron-impact energy E. The orbital electrons are described by the modification to the Hartree-Fock-Slater approximation described in Section 5.2 of our previous report AFAPL-TR-78-58. At this time it appears that the use of a non-relativistic description of the orbital wavefunction is justified for the outermost electrons under study.

The velocity distributions of the 6p and 6s electrons are displayed in Figures 1 and 2 of this section. In Figure 3 are presented the cross sections as a function of electron-impact energy E for ionization of the 6p electron and of both the 6s and the 6p electrons.

These individual and combined cross sections are tabulated in Table 1 of this section. There are no experimental data for comparison.

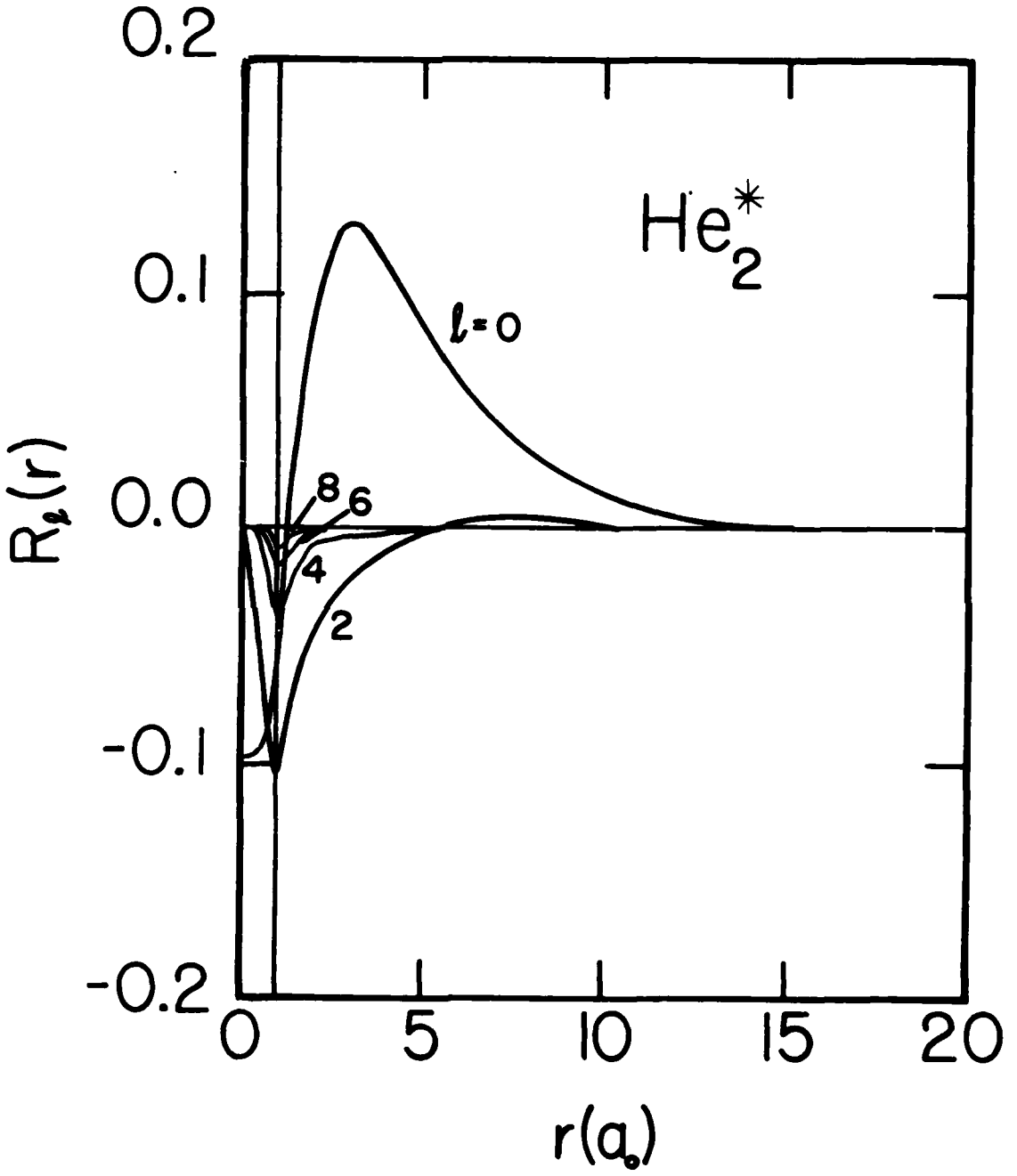

Figure 1. Radial Functions $R_\ell(r)$ in the single-center ℓ-expansion of the molecular orbital in He_2^*. The distance from the center-of-mass of the nuclei is r and the vertical line denotes position of nucleus from this center.

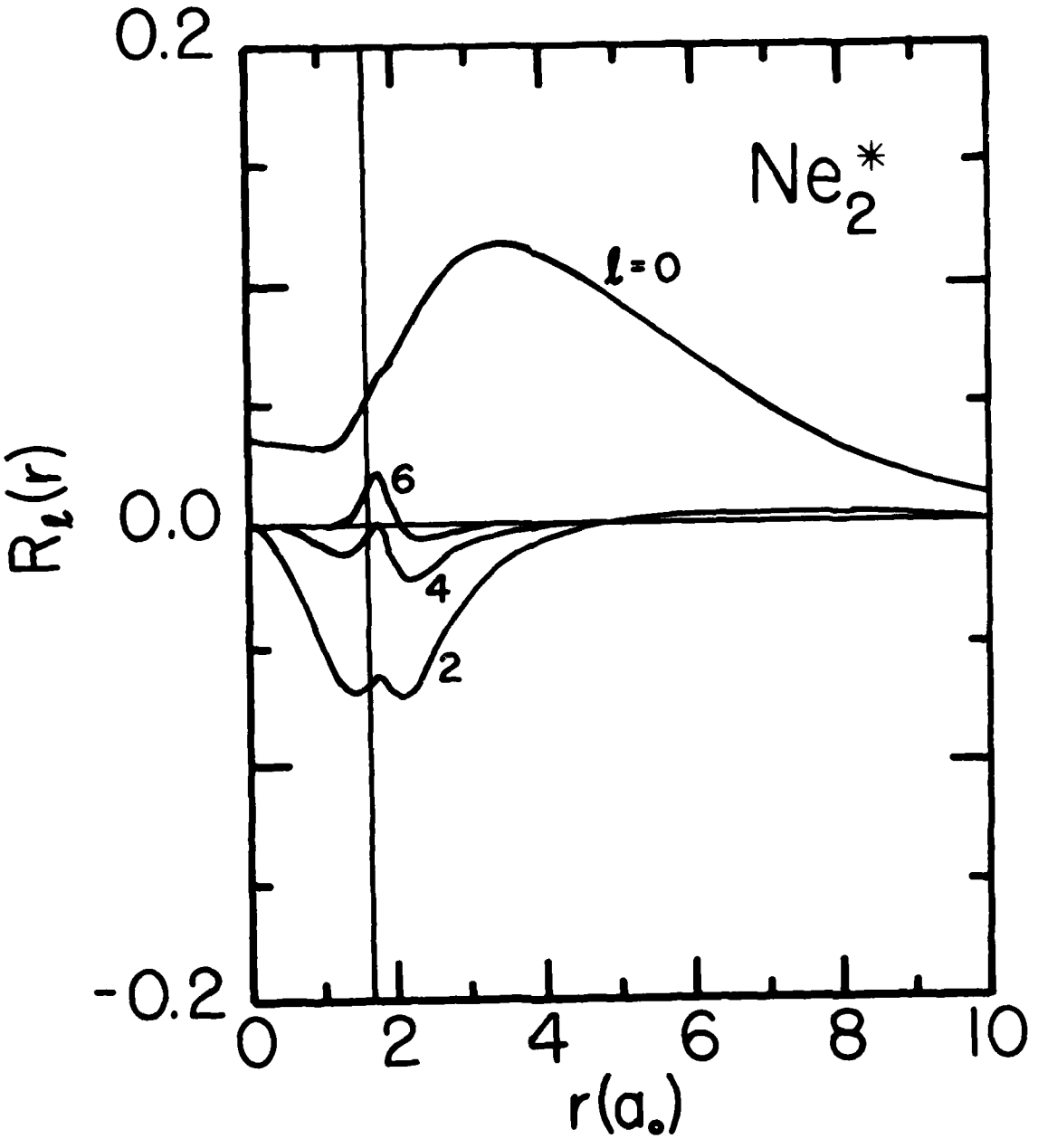

Figure 2. Radial Functions $R_\ell(r)$ in the single-center ℓ-expansion of the molecular orbital in Ne_2^*. The distance from the center-of-mass of the nuclei is r and the vertical line denotes position of nucleus from this center.

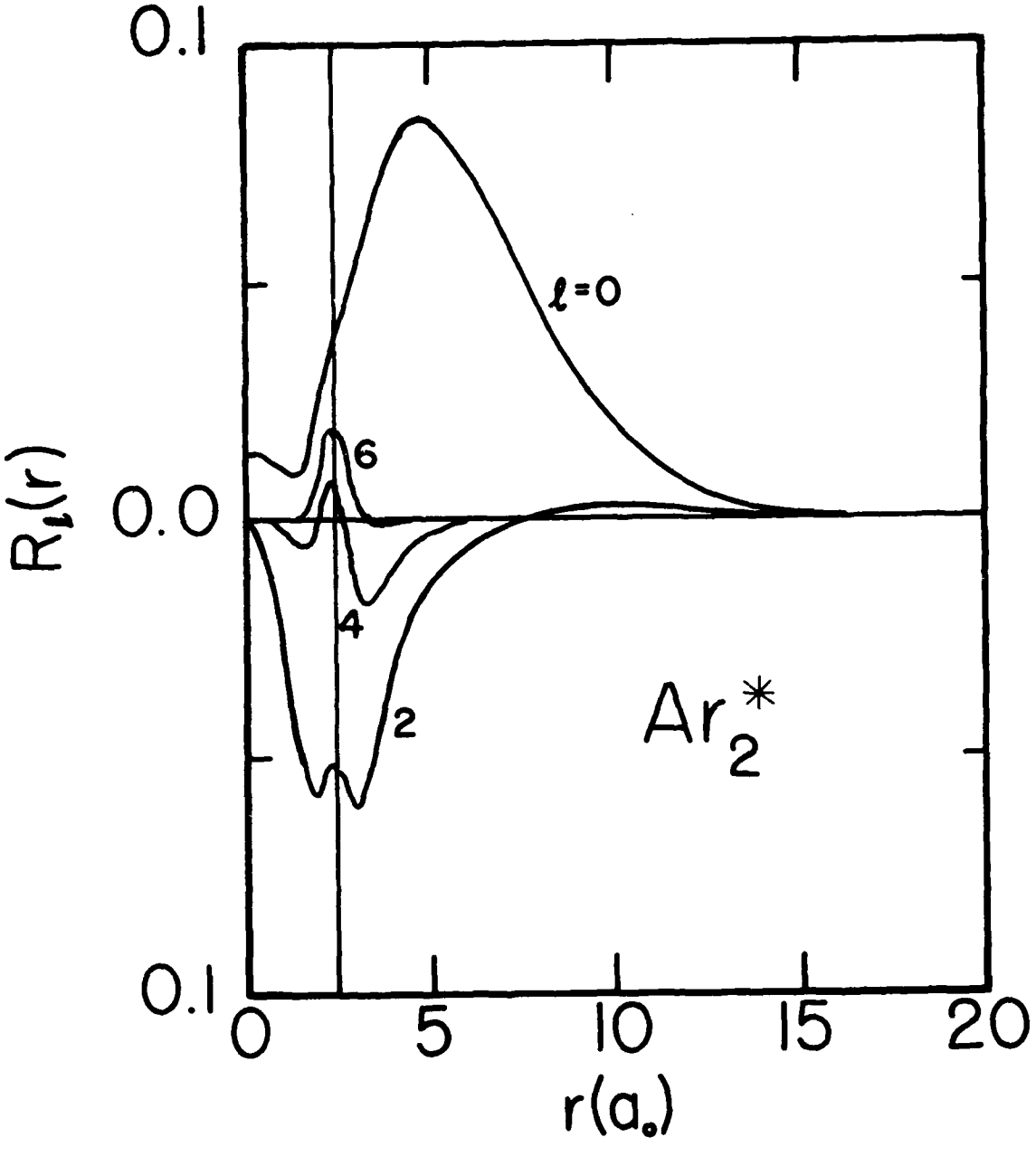

Figure 3. Radial Functions $R_\ell(r)$ in the single-center ℓ-expansion of the molecular orbital in Ar_2^*. The distance from the center-of-mass of the nuclei is r and the vertical line denotes position of nucleus from this center.

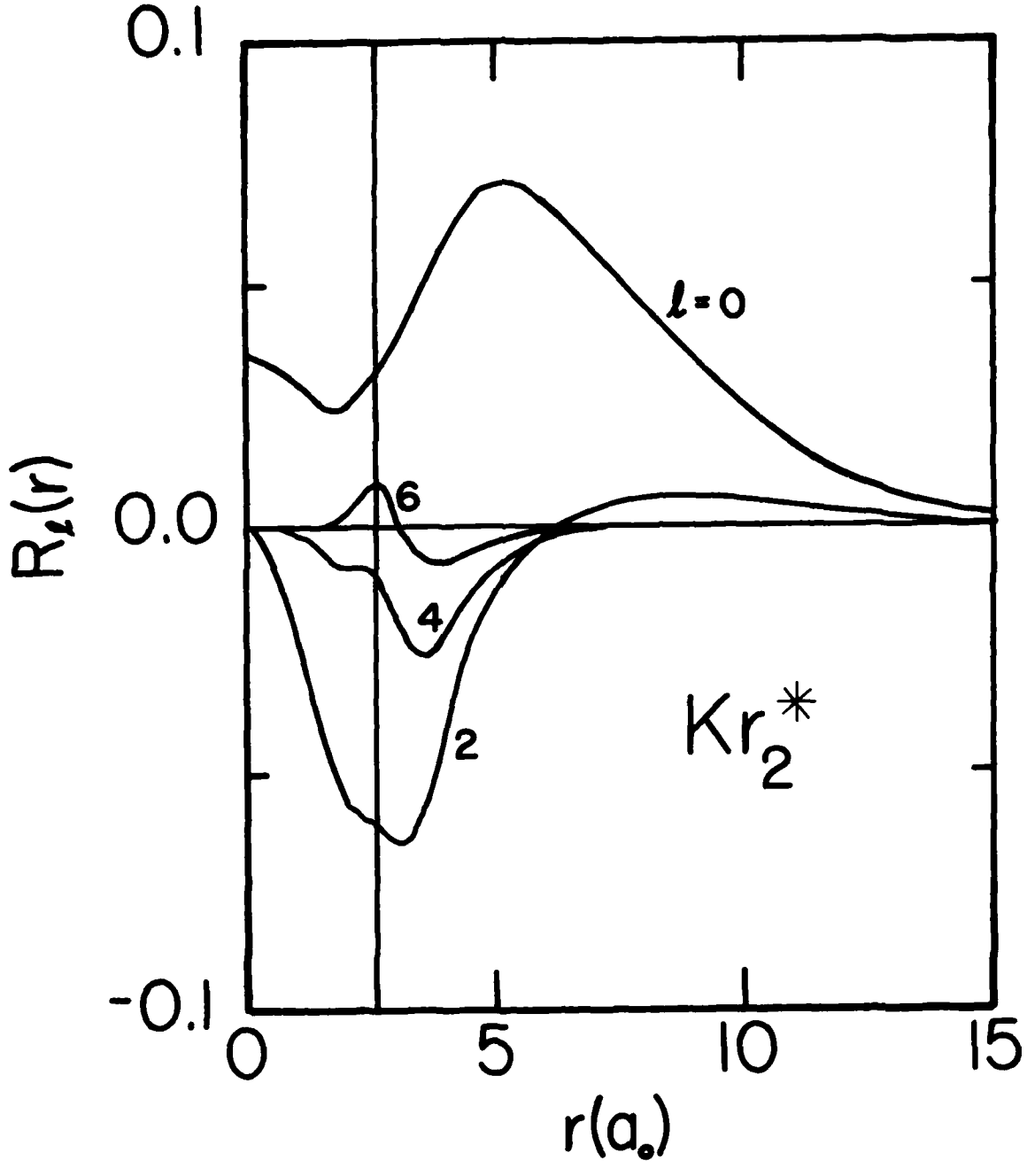

Figure 4. Radial Functions $R_\ell(r)$ in the single-center ℓ-expansion of the molecular orbital in Kr_2^*. The distance from the center-of-mass of the nuclei is r and the vertical line denotes position of nucleus from the center.

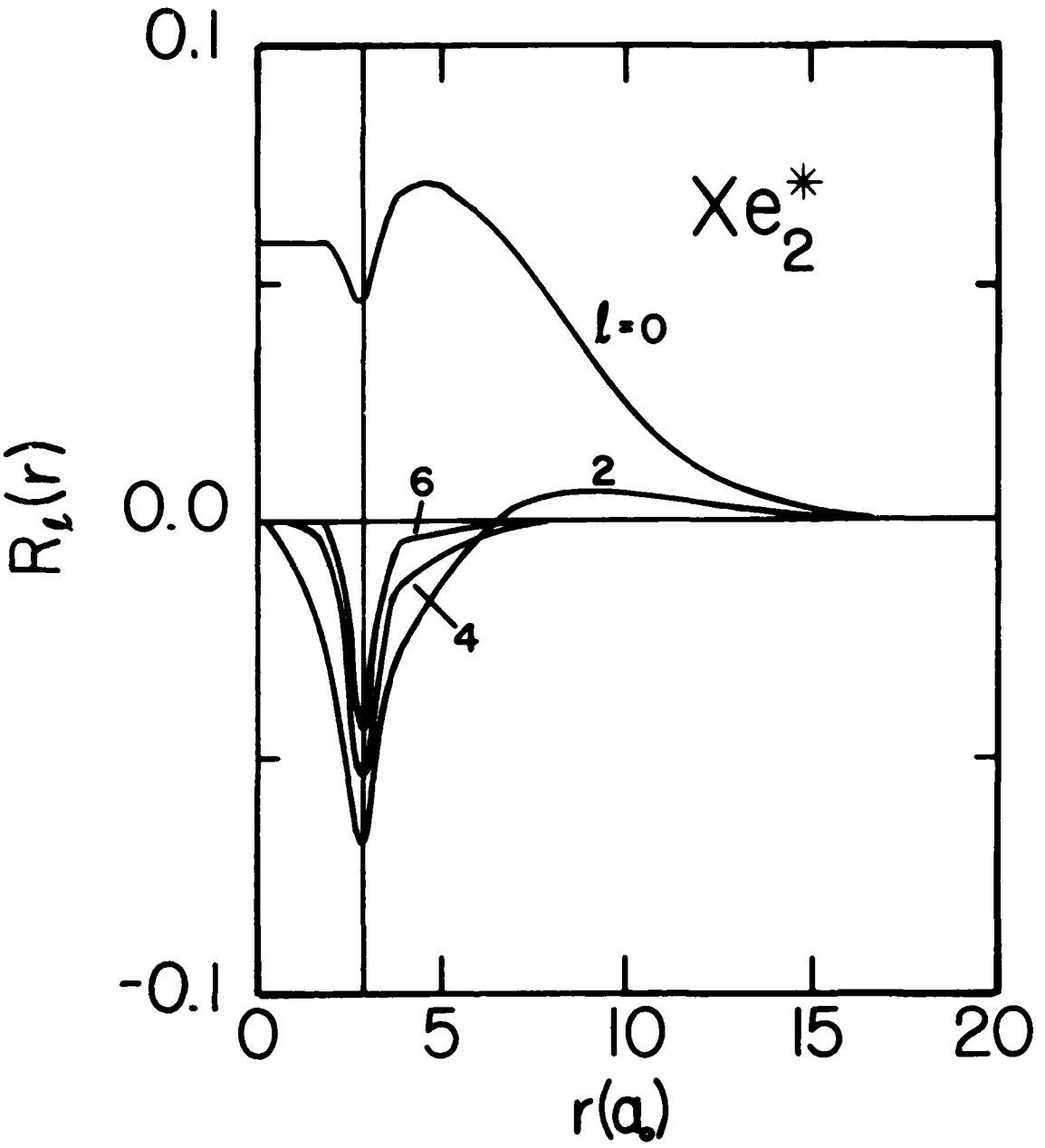

Figure 5. Radial Functions $R_\ell(r)$ in the single-center ℓ-expansion of the molecular orbital in Xe_2^*. The distance from the center-of-mass of the nuclei is r and the vertical line denotes position of nucleus from this center.

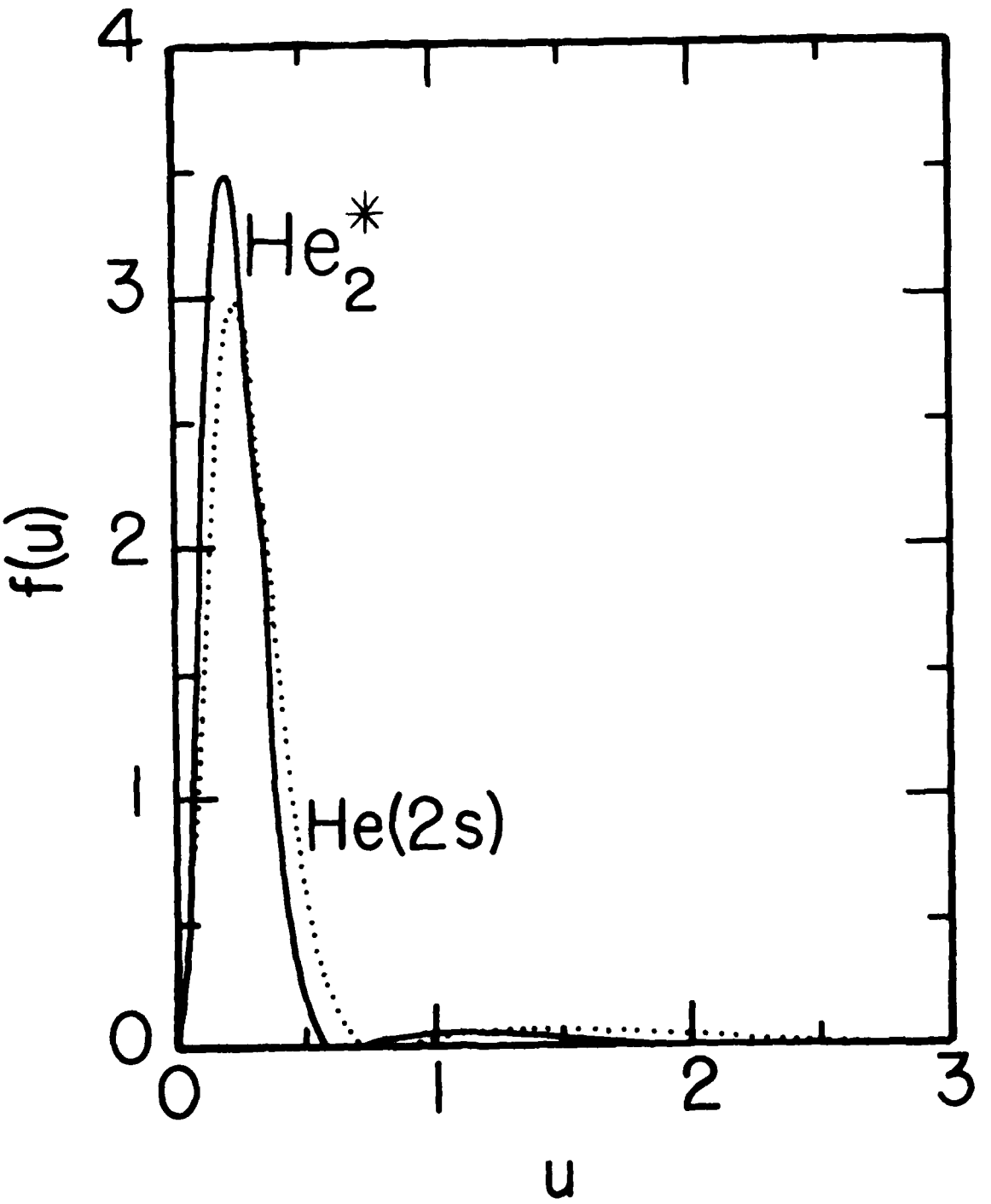

Figure 6. Normalized Distribution in speed of the orbital electron for metastable He_2^*. The corresponding distribution for the 2s electron of metastable He_2^* is shown for comparison.

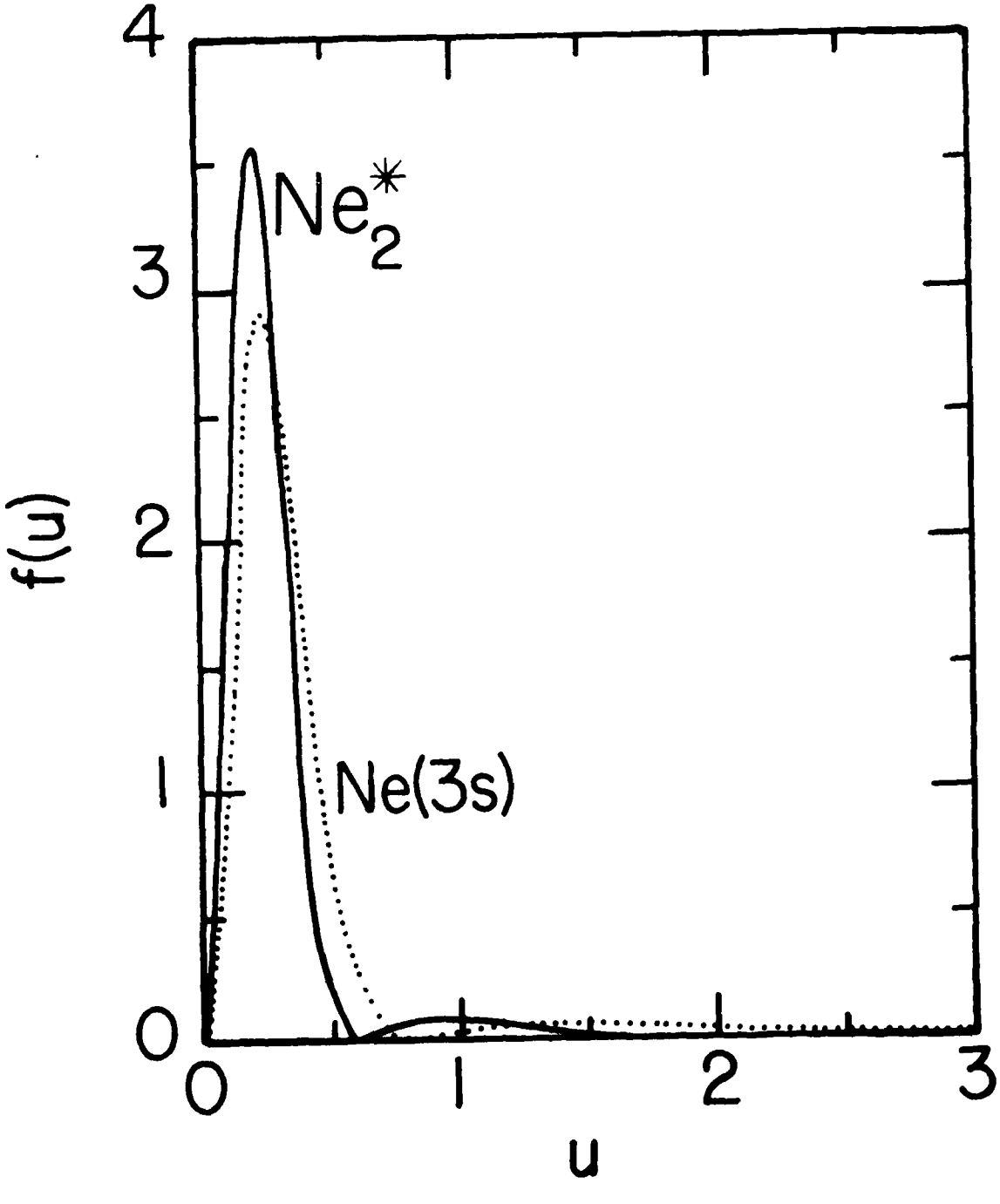

Figure 7. Normalized Distribution in speed of the orbital electron for metastable Ne_2^*. The corresponding distribution for the 3s electron of metastable Ne_2^* is shown for comparison.

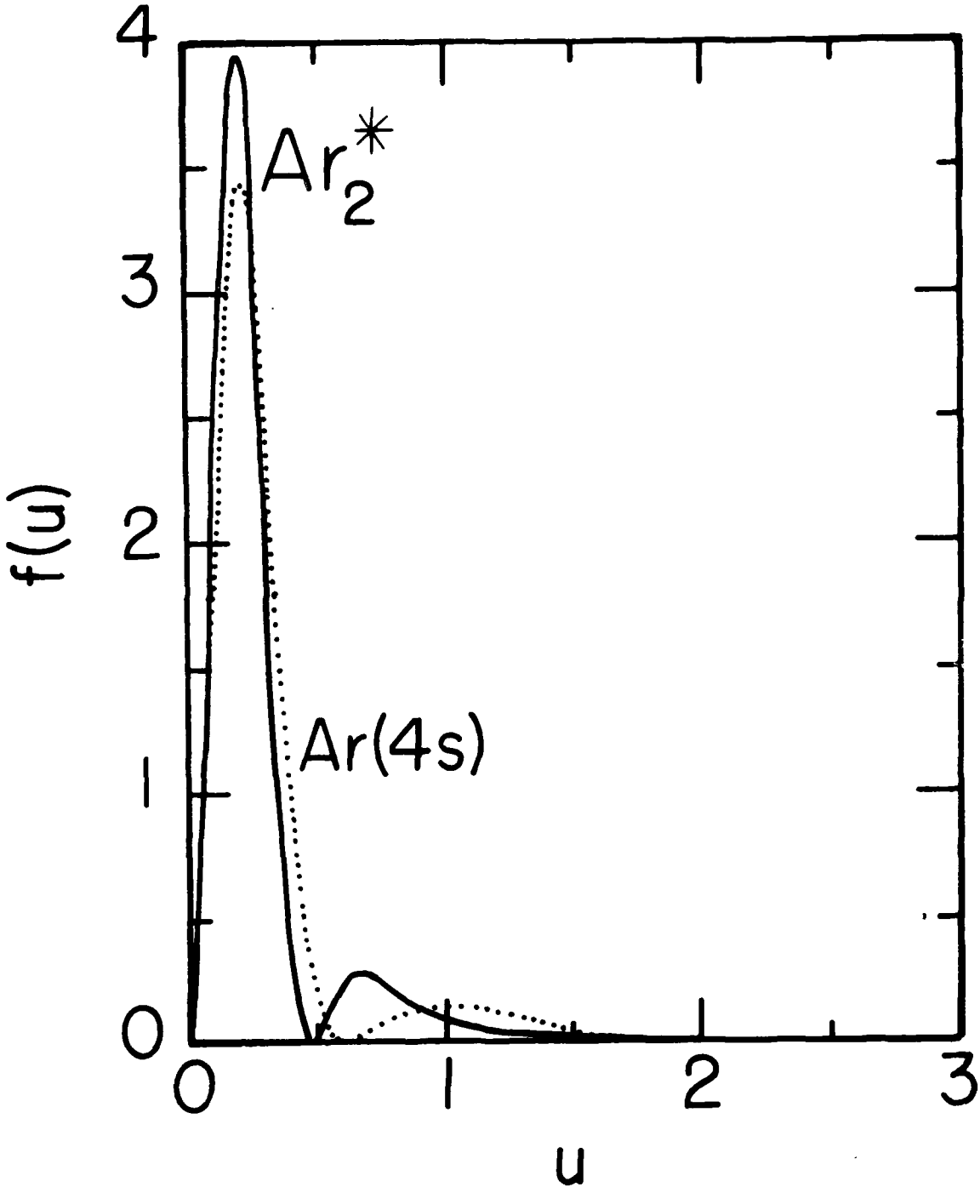

Figure 8. Normalized Distribution in speed of the orbital electron for metastable Ar_2^*. The corresponding distribution for the 4s electron of metastable Ar_2^* is shown for comparison.

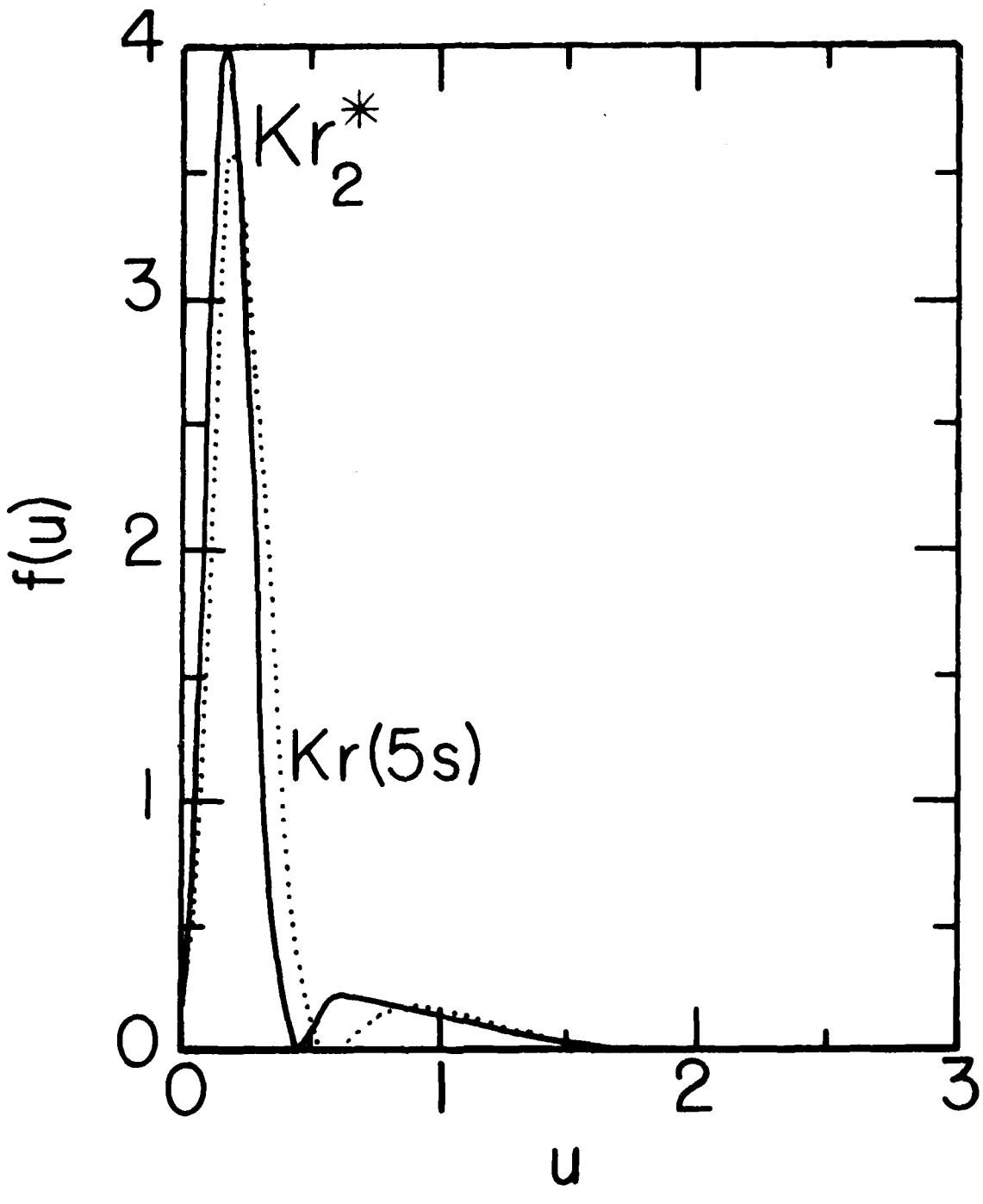

Figure 9. Normalized Distribution in speed of the orbital electron for metastable Kr_2^*. The corresponding distribution for the 5s electron of metastable Kr_2^* is shown for comparison.

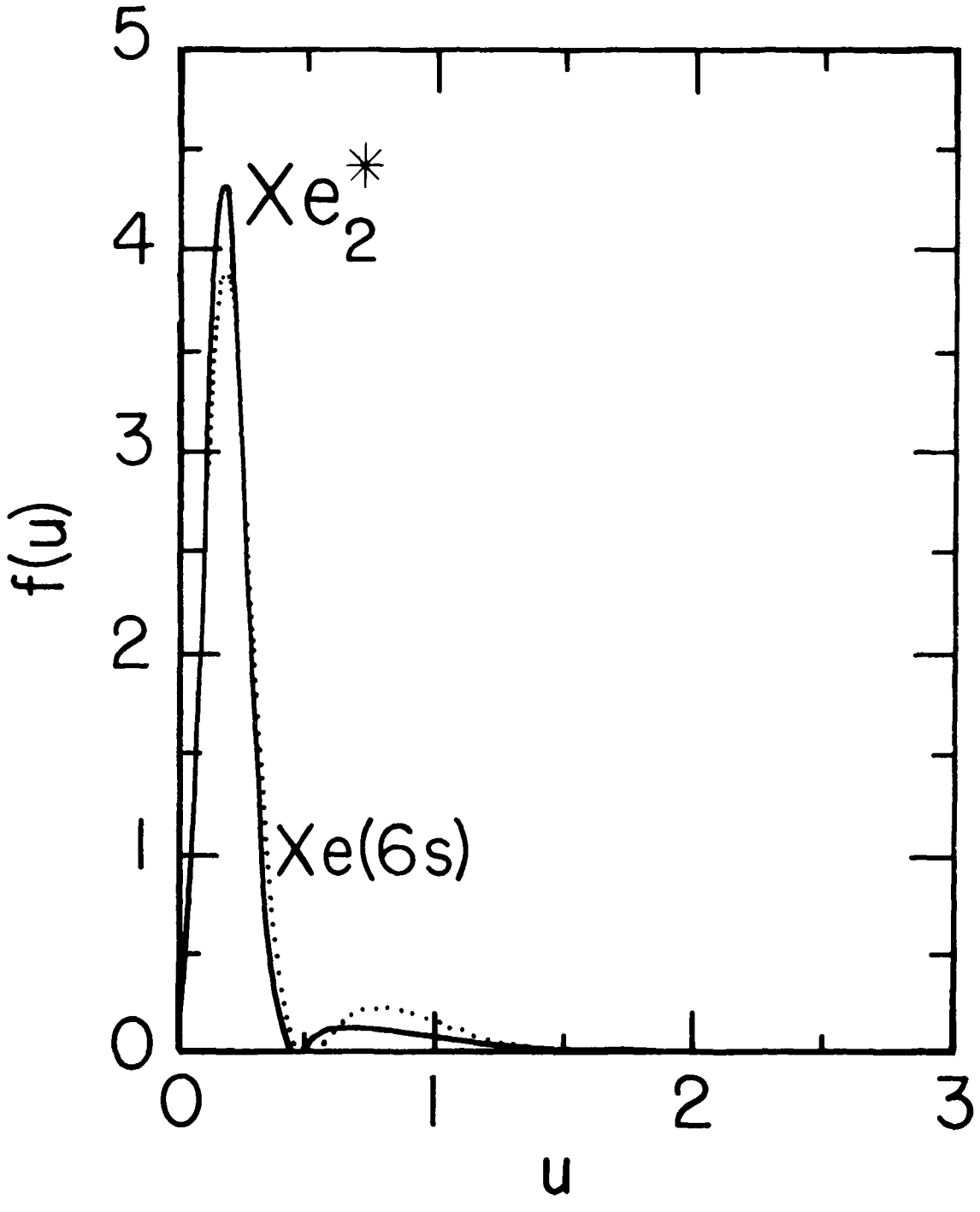

Figure 10. Normalized Distribution in speed of the orbital electron for metastable Xe_2^*. The corresponding distribution for the 6s electron of metastable Xe_2^* is shown for comparison.

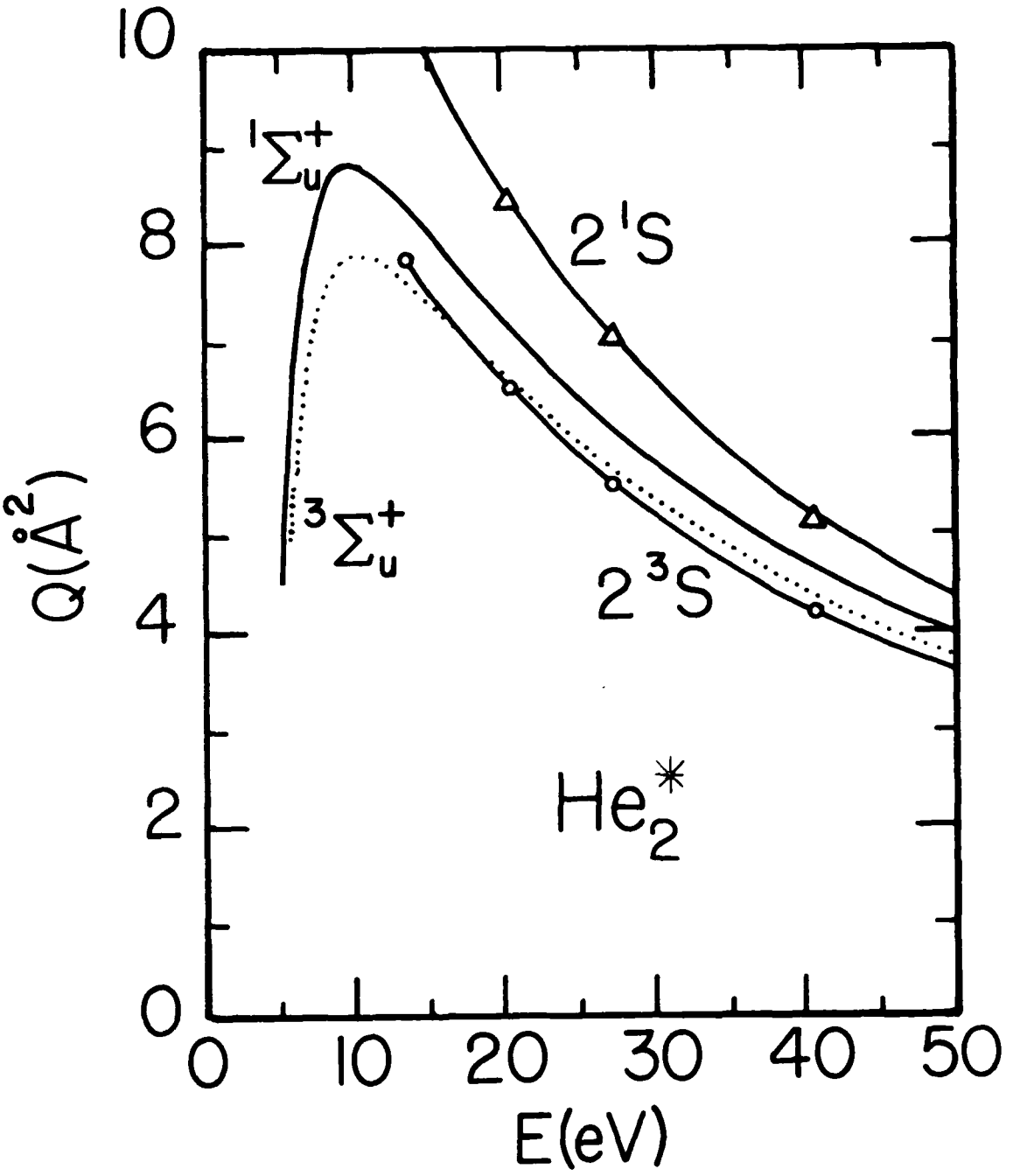

Figure 11. Cross sections ($Å^2$) for electron impact ionization of metastable ($^{1,3}\Sigma_u^+$) excimer states of He_2^* and of the atomic metastable levels ($2^{1,3}S$) of He^*.

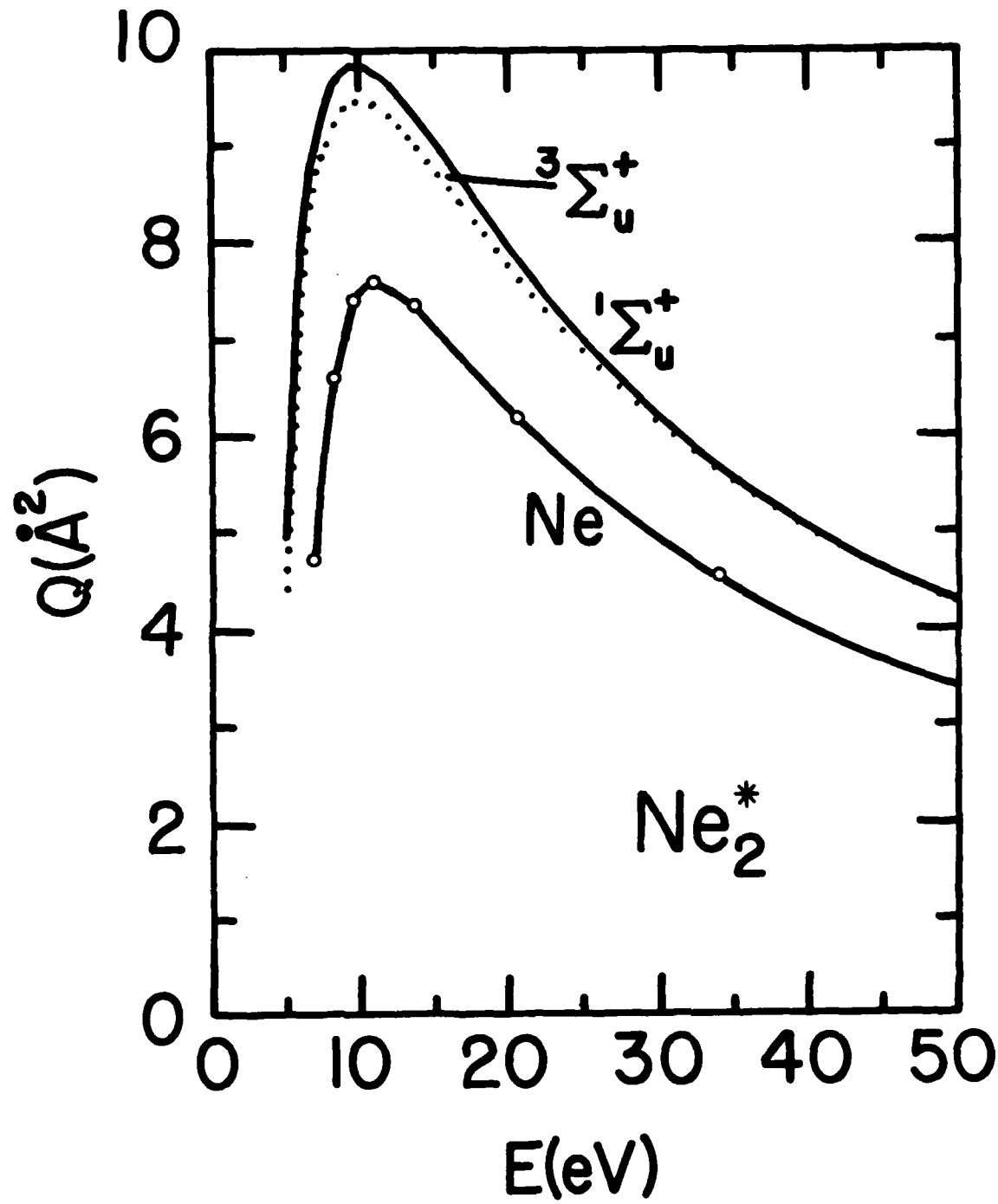

Figure 12. Cross sections ($Å^2$) for electron impact ionization of metastable ($^{1,3}\Sigma_u^+$) excimer states of Ne_2^* and of the atomic metastable levels ($2^{1,3}S$) of Ne^*.

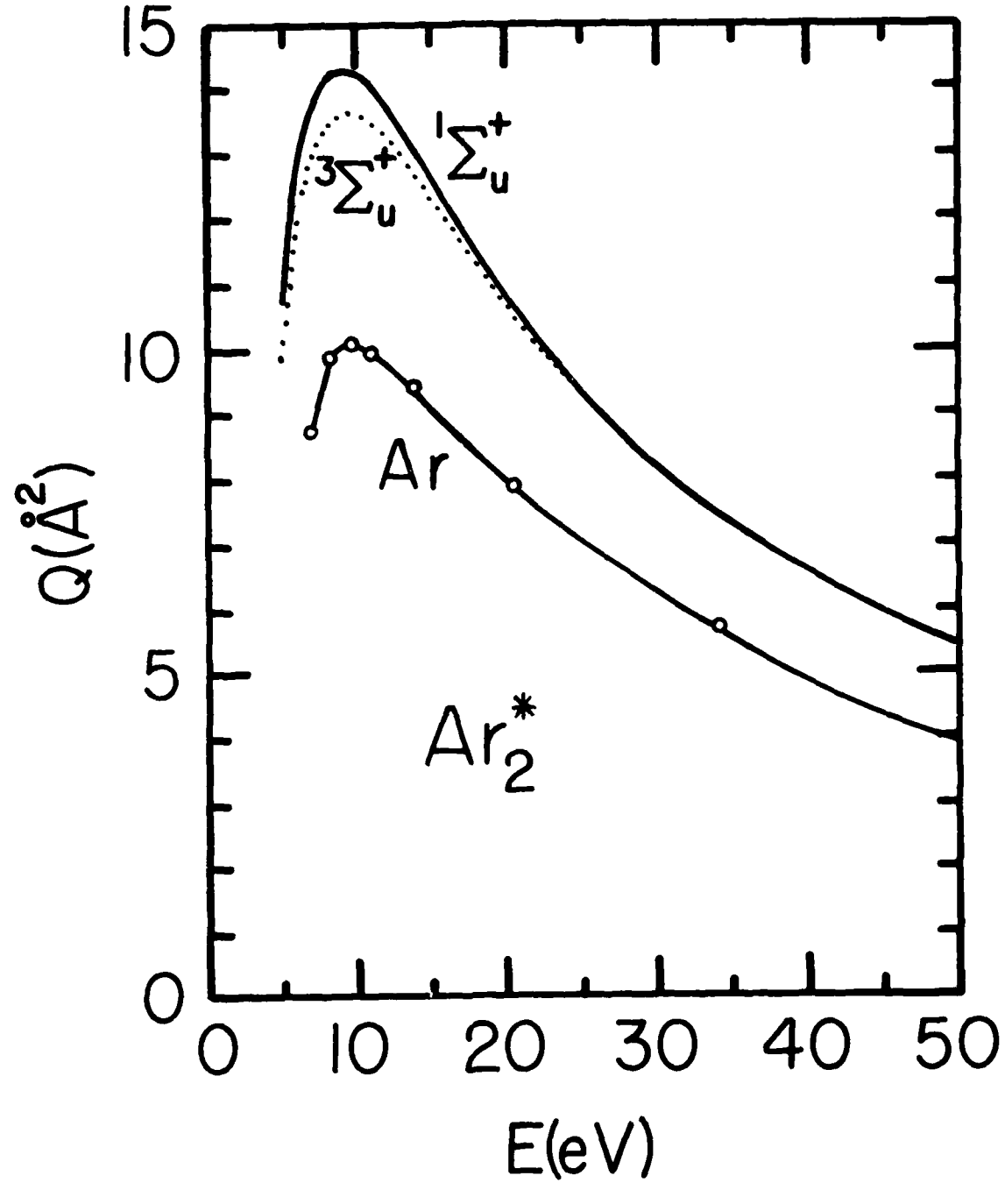

Figure 13. Cross sections ($Å^2$) for electron impact ionization of metastable ($^{1,3}\Sigma_u^+$) excimer states of Ar_2^* and of the atomic metastable levels ($2^{1,3}S$) of Ar^*.

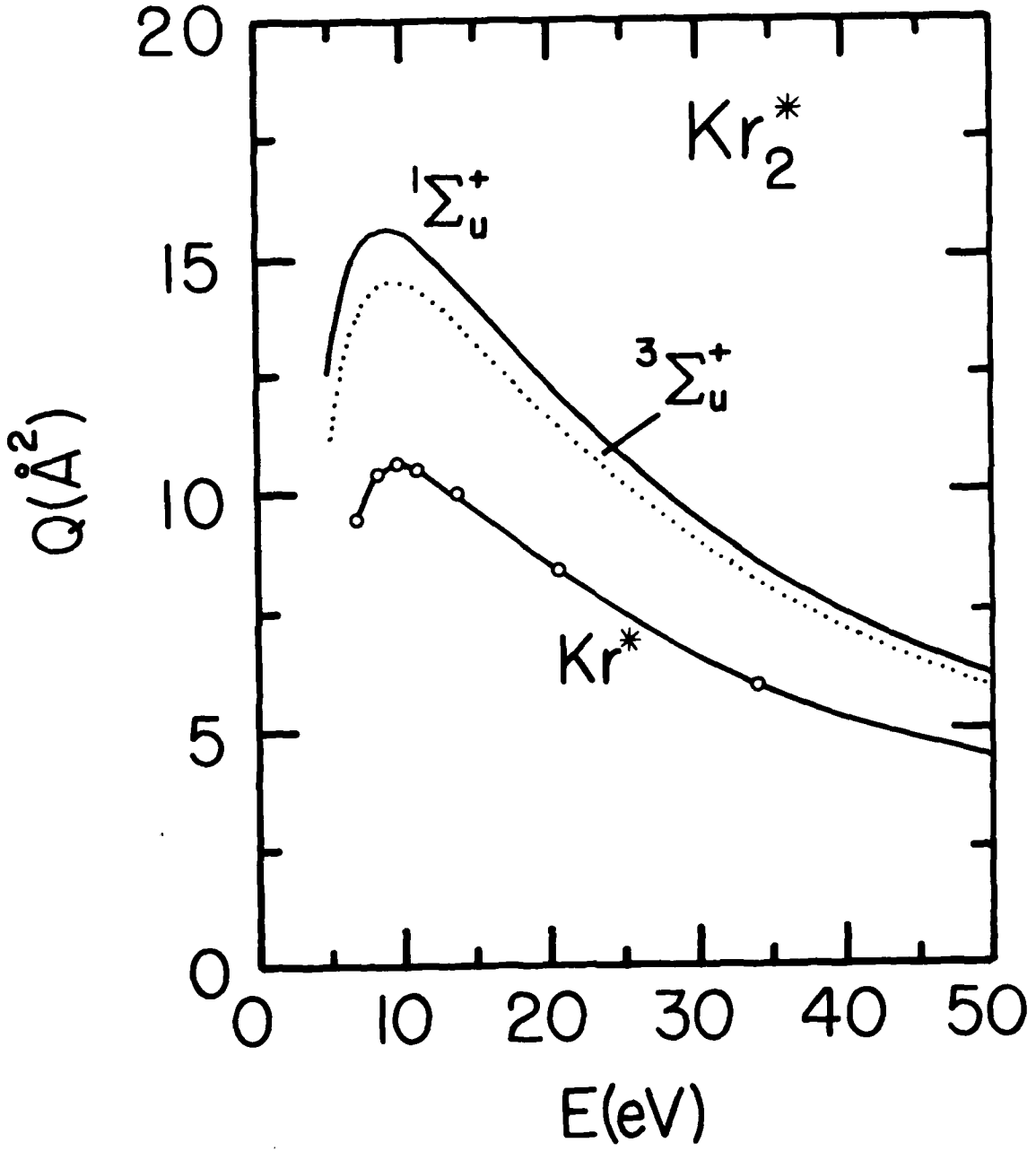

Figure 14. Cross sections ($\mathring{A}^2$) for electron impact ionization of metastable ($^{1,3}\Sigma_u^+$) excimer states of Kr_2^* and of the atomic metastable levels ($2^{1,3}S$) of Kr^*.

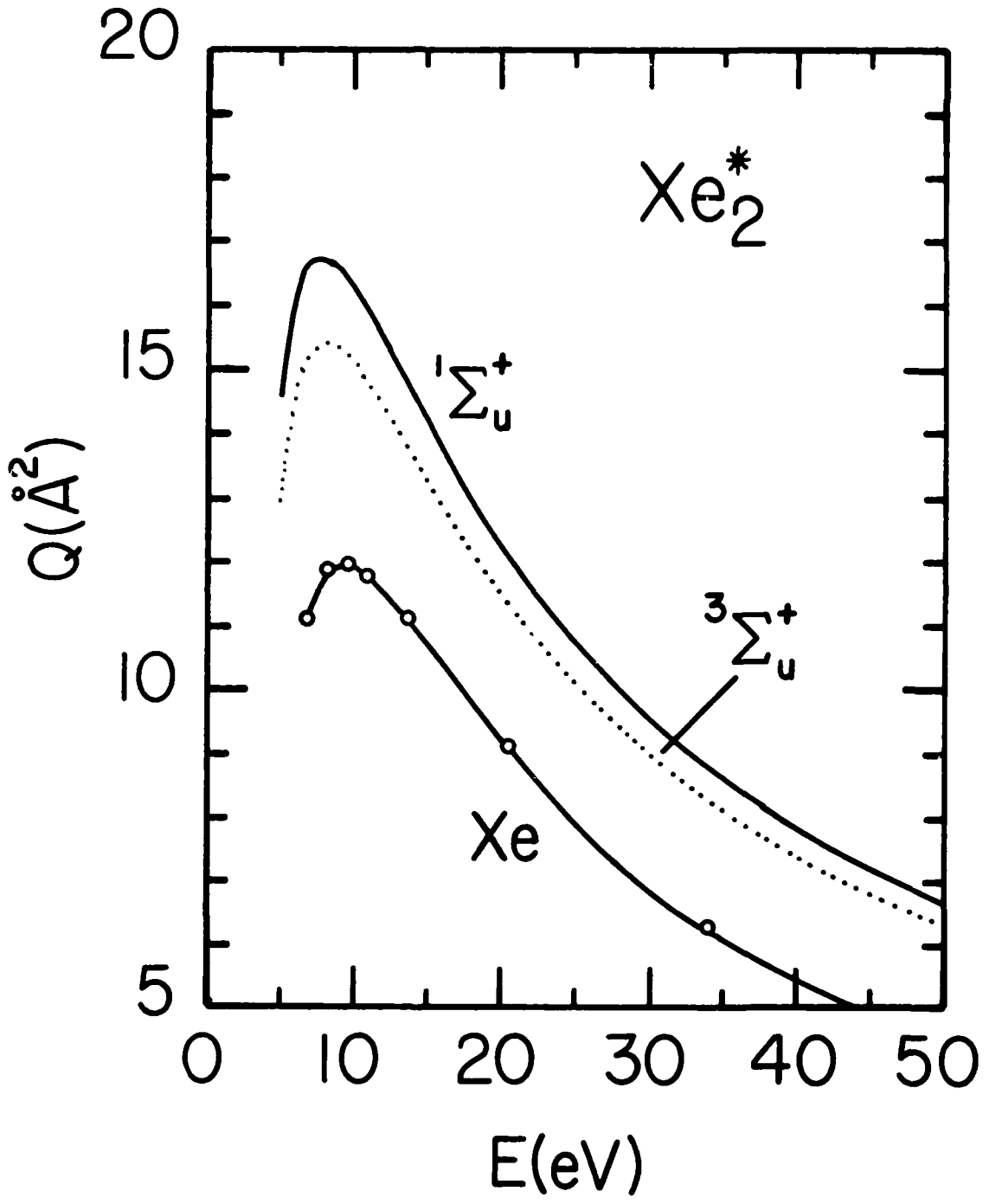

Figure 15. Cross sections ($Å^2$) for electron impact ionization of metastable ($^{1,3}\Sigma_u^+$) excimer states of Xe_2^* and of the atomic metastable levels ($2^{1,3}S$) of Xe^*.

Table 9

Cross Sections for the Electron Impact Ionization of Excited States of Mercury.

$$e + Hg(6s[^2S]\ 6p\ [^3P]) \rightarrow 2e + Hg^+(^2S)$$

$$e + Hg(6s[^2S]\ 6p\ [^3P]) \rightarrow 2e + Hg^+(5d^{10}6p)$$

	$Q(\mathring{A}^2)$		
E(eV)	6p	6s	6p + 6s
6	0.455	--	0.455
7	2.07	--	2.07
8	3.62	--	3.62
10	5.69	--	5.69
12	6.63	--	6.63
14	6.91	0.220	7.13
16	6.86	0.551	7.41
18	6.65	0.788	7.44
20	6.37	0.941	7.31
30	4.99	1.14	6.13
40	4.05	1.11	5.16
50	3.44	1.04	4.48
60	3.01	0.975	3.99
70	2.69	0.905	3.60
80	2.43	0.838	3.27
90	2.22	0.776	3.00
100	2.06	0.720	2.78
125	1.72	0.608	2.33
150	1.46	0.526	1.99
175	1.27	0.467	1.74
200	1.13	0.421	1.55
300	0.777	0.311	1.09
400	0.602	0.246	0.848
500	0.493	0.201	0.694

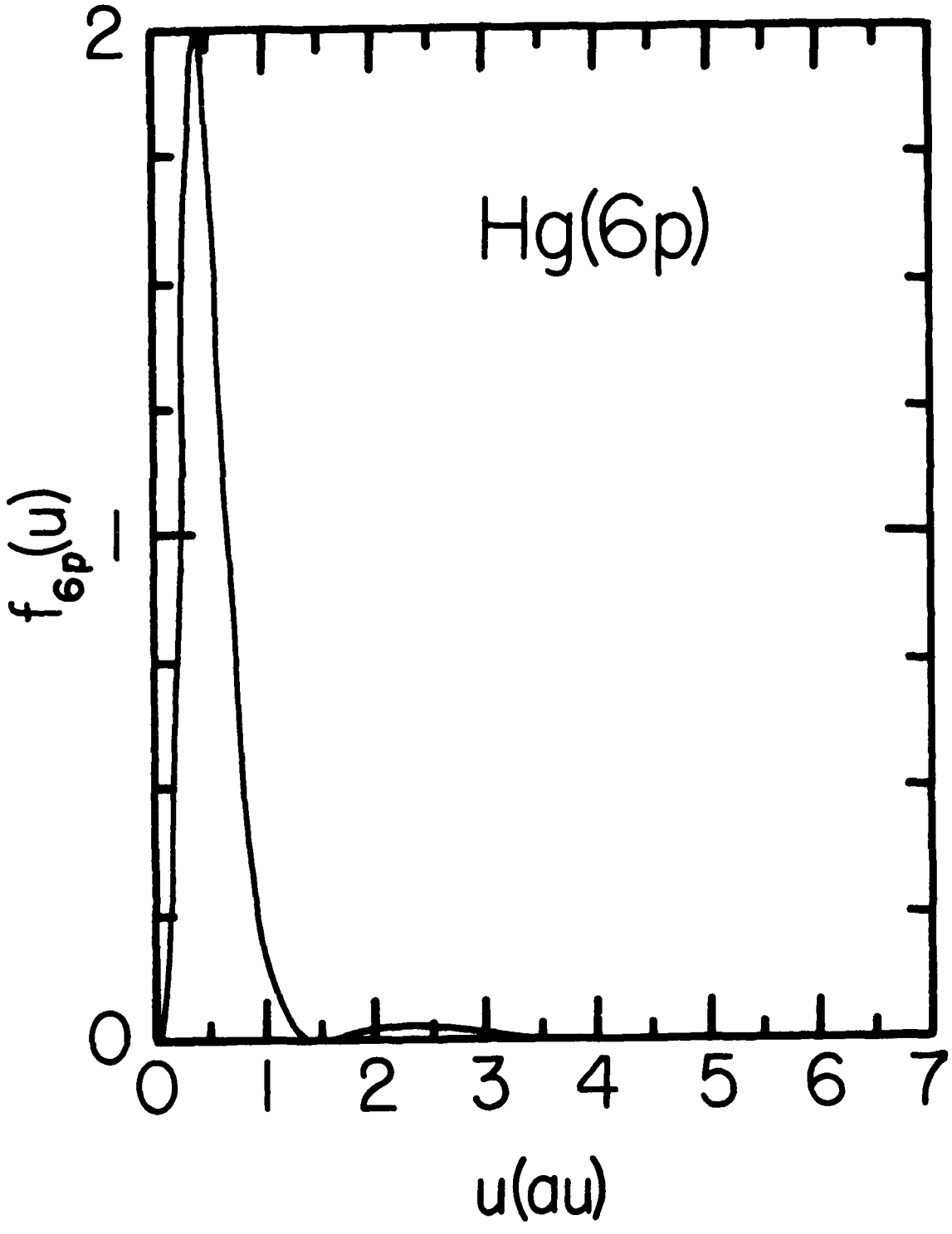

Figure 16. Normalized Distribution in speed of the 6p electron of metastable mercury Hg*.

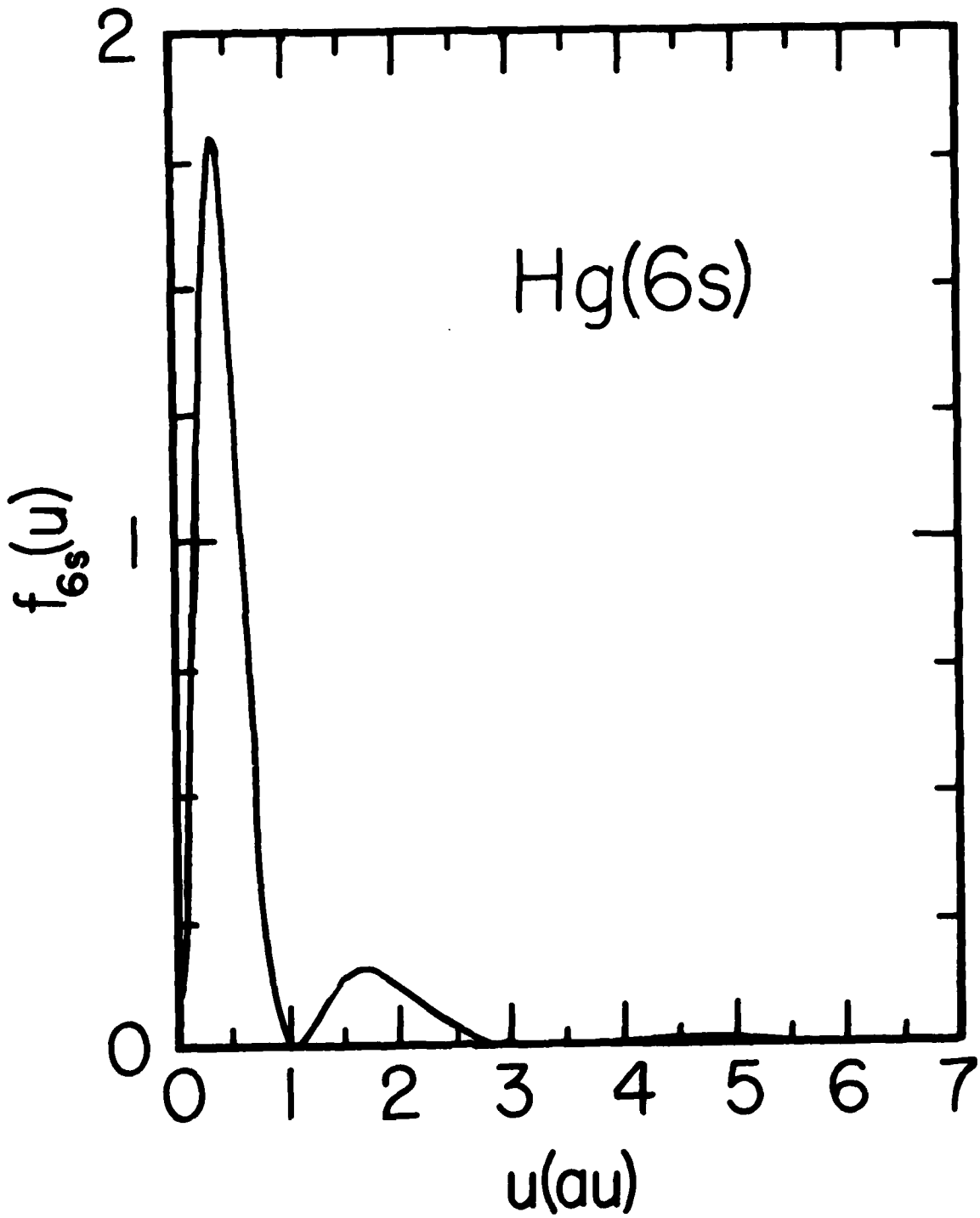

Figure 17. Normalized Distribution in speed of the 6s electron of metastable mercury Hg^*.

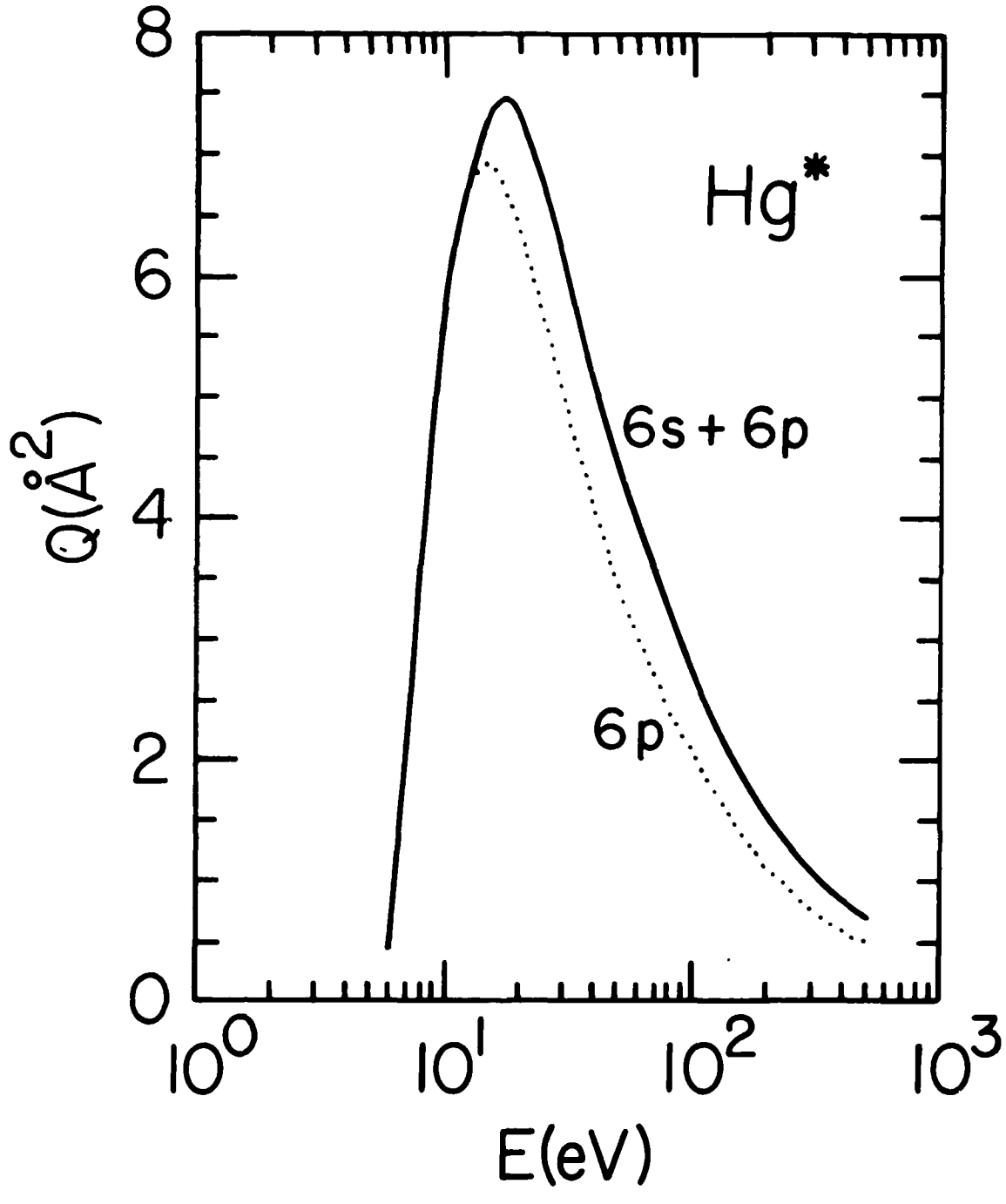

Figure 18. Cross sections ($Å^2$) for ejection of the 6p, and the combined (6s + 6p) electrons from metastable mercury Hg^*.

SECTION V

TRENDS IN INELASTIC FORM FACTORS AND BORN CROSS SECTIONS FOR $n\ell \rightarrow (n+1)\ell'$ COLLISIONAL TRANSITIONS.

The following research represents further development in the theoretical prediction of various systematic trends noted for collisions involving atoms initially in excited states. In a previous report AFAPL-TR-78-58 we discussed such patterns in $n\ell \rightarrow n'\ell'$ collisional transitions for instances in which $n' >> n$ e.g. $n = 10 \leftrightarrow n' = 20$ or else when the energy of transition was relatively large e.g. $n = 2, 3, 4 \rightarrow n' = n + 1$. In the following, we shall examine $n\ell \rightarrow (n+1)\ell'$ collisional transitions for n fairly large.

5.1 INTRODUCTION

Previous studies (Flannery et al.[19], Flannery and McCann[17], Ton-That and Flannery,[22] Ton-That et al.,[23]) have suggested, and a more recent investigation[16] (Flannery and McCann, 1979) has revealed interesting systematic trends in collisional transitions between excited atomic states induced by electron and by heavy-particle impact. These trends would assume significance in many astrophysical situations (see, for example, Dupree and Goldberg,[1]

Flannery and McCann[18] have shown that both the inelastic form factor and associated cross sections for $n\ell \to n'\ell'$ transitions, with $n'>>n>>1$ oscillate on an increasing background as ℓ' is increased until a unique value ℓ'_{max} is attained, after which they exhibit a rapid decrease. The value ℓ'_{max} is strongly dependent on the initial value of the principal quantum number n, is relatively insensitive to changes in the initial angular-momentum quantum number ℓ and is given by

$$\ell'_{max} = \min \left\{ (n'-1) \, , \sim \left(n \left[\frac{2(n+3)}{(n+1)} \right]^{\frac{1}{2}} - \frac{1}{2} \right) \right\} \quad . \qquad (1)$$

The chief contribution to the population of the final level n' in e-atom and atom-atom collisions arise from the $n[\ell=0,1,\ldots,(n-1)] \to n'\ell'_{max}$ array of transitions. This array may include some with dipole character i.e. $\ell=\ell'_{max} \pm 1$ and these dipole transitions tend to be somewhat more probable. However, the important feature is that ℓ'_{max} is primarily n-dependent and, as such, may have a value inaccessible to dipole transitions. For example, the strongest collisional transitions in the $10\ell \to 20\ell'$ array (with variation of ℓ and ℓ') are the set $10\ell \to 20(\ell'_{max} \sim 15)$, none of which possesses dipole character. Since $n'>>n>>1$, the magnitude and range of the initial and final orbitals are quite different (because of the relatively large energy-separation between the levels) and the expression (1) for ℓ'_{max} is determined from a consideration of the overlap

of the initial radial orbital with the first lobe of the final orbital, the region yielding any significant overlap.

The situation with $n\ell \rightarrow (n+1)\ell'$ collisional transitions for large n is not as clear, the energy separation between the neighboring levels becoming very small. In this paper we consider these transitions between adjacent highly-excited levels in an effort to determine any associated systematic trends in the inelastic form factors and corresponding collisional cross sections. We note that (1) would predict that $\ell'_{max} \approx (n'-1)$ in this limit. As a result of our study we present new features associated with $n \rightarrow (n+1)$ collisional transitions. In doing so, we also express a note of caution in arbitarily following the assumption in $n\ell \rightarrow n'\ell'$ collisional excitation that the associated $\ell \rightarrow \ell \pm 1$ dipole transitions are strongest at all impact-energies and are the only ones that need calculation for various problems of astrophysical interest, as, for example, in theoretical interpretation of radio recombination spectra of HI and HII regions of hot stars (cf Dupree and Goldberg[12]).

5.2 THEORY

The inelastic form factor,

$$F_{fi}(\underset{\sim}{K}) = \langle \psi_f(\underset{\sim}{r}) \mid \exp(i\underset{\sim}{K}\cdot\underset{\sim}{r}) \mid \psi_i(\underset{\sim}{r}) \rangle \qquad (2)$$

for i→f transitions in atomic hydrogen with wavefunctions $\psi_n(\underset{\sim}{r})$, as a function of momentum-change $\underset{\sim}{K}$, is, from Born's approximation to more elaborate close-coupling treatments, a key quantity implicit in most theoretical descriptions of a collision. Any systematic trends in (2) exhibited via variation of the quantum numbers (n ℓ m) of initial and final states are, in general (Flannery and McCann[18]), reflected in the corresponding collision cross sections. The role of the form factor in a collision at relative energy E is made apparent by

writing the Born cross section as, (cf Flannery and McCann, 1978),

$$Q_{n\ell m,n\ell'm'}(E) = \frac{1}{8\pi}\left(\frac{2M}{\hbar^2 k_f^2}\right)\int_{(k_i-k_f)}^{(k_i+k_f)} |F_{n'\ell'm',n\ell m}(\underset{\sim}{K})|^2 |T^B_{e\ell}(K)|^2 K\, dK \qquad (3)$$

where the initial and final wavenumbers of relative motion of the collision partners with reduced mass M are k_i and k_f respectively. For electron-atom collisions, the Born transition-matrix element for (e-e) potential scattering in (3) is $T^B_{e\ell} = 4\pi e^2/K^2$ which exerts a dramatic influence on F_{fi} in (2) only in the "optical" limit of vanishing momentum-change when it effectively amplifies any dipole term in F_{fi}. This dipole then dominates the remaining multipoles at high impact energies, with the result that the cross section for $n \to n'$ transitions reduces to the Bethe asymptotic-limit with its characteristic $E^{-1}\ell n\, E$ dependence. With increasing n and n', however, the onset of this limit is pushed further into regions of higher impact energy E such that for a wide range of energies, E, (up to 1000 eV for e-He(2^3S) collisions (Flannery and McCann[17]), the $\ell \to \ell \pm 1$ dipole transitions are no longer dominant.

For H(1s)-projectiles remaining in the ground state,

$$T^B_{e\ell}(K) = \frac{4\pi e^2}{K^2}\left[1 - F^2_{1s,1s}(K)\right] = \frac{4\pi e^2}{K^2}\,\frac{K^2(8+K^2)}{(4+K^2)^2} \qquad (4)$$

which is non-singular as $K \to 0$ such that the cross section $Q_{n\ell,n'\ell'}$ for $n\ell \to n'\ell'$ transitions will correlate more closely, than for e-atom collisions, with the behavior of the inelastic form factor F_{fi}. Moreover, improvement to Born's approximation can be obtained (Flannery[13,15,16]), as in the impulse approximation, by replacing $T^B_{e\ell}$ of (3) by a more accurate (exact) T-matrix $T_{e\ell}$ for potential scattering of the "frozen" electrons of the target by the projectile. In the limit of slow collisions, $T_{e\ell}$ is isotropic such that details of the collisional transition are then governed entirely by F_{fi}.

5.3 RESULTS AND DISCUSSION

For $n\ell \rightarrow n'\ell'$ collisional transitions in $H(n\ell)$, or in any highly-excited Rydberg atom, various theoretical predictions for the population distribution over final states with angular momentum ℓ' can be given following detailed consideration of (2) and (3). In general, the cross section as a function of impact-energy E has a maximum value Q_{max} which originates from K-integration over the largest peak F_{max} in the inelastic form factor F_{fi} as a function of momentum-change K.

In an effort to isolate the key features we consider, via a computer analysis, the variation of the maximum values, F_{max} and Q_{max}, with respect to the various quantum numbers of the levels involved. Rather than presenting here all the many tables of cross-section data (which did involve lengthy computing time particularly for transitions between high-n states, due to the large number of angular momentum states, and which may be obtained, if required, from the authors) we have attempted to isolate the key features by presenting here only the maximum values of $Q_{n\ell,n'\ell'}$ with respect to impact-energy E and of the averaged value

$$Q_{n,n'\ell'} = \frac{1}{n} \sum_{\ell=0}^{(n-1)} Q_{n\ell,n'\ell'} = \frac{1}{n} \sum_{\ell=0}^{(n-1)} \frac{1}{(2\ell+1)} \sum_{m,m'} Q_{n\ell m,n'\ell'm'} \quad . \quad (5)$$

(a) $n\ell \rightarrow n'\ell'$ Transitions ($n'>>n$). In order to later illustrate the differences between the cases, $n'>>n$ and $n' = n+1$, and to remind us of the systematic trends obtained previously by Flannery and McCann[18]. Fig. 1 shows that this maximum F_{max} in general oscillates on a background which rises as ℓ' is increased until it attains a pronounced peak at a unique value ℓ'_{max} which is strongly dependent only on the initial principal quantum number n and which is fairly insensitive to the remaining quantum numbers ℓ and n'. For $\ell'>\ell'_{max}$, F_{max} exhibits a final

dramatic fall. This sharp drop however will not be observed unless the final n' is sufficiently large so as to accomodate that unique value ℓ'_{max}. This final decline with ℓ' therefore becomes more marked by making n' large as for the ($n\ell \rightarrow 20\ell'$) transition-array in Fig. 1.

By averaging over ℓ before varying K and ℓ', the oscillations can be suppressed and the key issues - the rise, peak and rapid decline - becomes more apparent, as in Fig. 1 for $n = 10 \rightarrow 20\ell'$ transitions. The value of ℓ'_{max} in Fig. 1 is in agreement with that predicted by Eq. (1).

These trends are preserved in the cross sections for the corresponding electron-atom and atom-atom inelastic collisions (Flannery and McCann[18]). Since many final-angular momenta ℓ' contribute to the cross section $Q_{n\ell,n'}$ for $n\ell \rightarrow n'$ transitions (rather than predominant dipole $\ell \rightarrow \ell \pm 1$ transitions), the collision is well suited to quasi-classical concepts.

The Born cross section $n'^{-2} \sum_{\ell'=o}^{(n'-1)} Q_{n,n'\ell'}(E)$ summed over all final angular momentum states ℓ' is displayed in Fig. 2 as a function of impact-energy E for $10 \rightarrow 20$ transitions together with the cross section

$$Q_{n,n'}(E) = \frac{2\pi a_o^2}{3E} \int_{\frac{1}{2}(\varepsilon_{n'}+\varepsilon_{n'-1})}^{\frac{1}{2}(\varepsilon_{n'}+\varepsilon_{n'+1})\infty} d(\varepsilon-\varepsilon_n) \int_o^{\infty} \left[n^{-2} \sum_{\ell=o}^{n-1} (2\ell+1)\, F_{n\ell}(u) \right] \left[\frac{1}{P_-^3} - \frac{1}{P_+^3} \right] \frac{du}{u} \qquad (6)$$

derived, with all quantities in atomic units, from the classical binary encounter approximation (cf Vriens[4], Flannery[14]). Here it is assumed that ε the energy-change $\varepsilon_n - \varepsilon_{n'}$ between the two states of internal energy ε_n and $\varepsilon_{n'}$ respectively is achieved via a binary encounter between the incident electron of speed v and the valence electron attached with speed u to its parent nucleus. The nucleus is ignored except insofar as it generates a velocity distribution $F_{n\ell}(u)$, normalized to unity, of the orbital electron appropriate to the initial $n\ell$-state. The limits to the momentum change P (in atomic units) in the e-e

collision are

$$\left.\begin{aligned} P_- &= \max\left[\,|u'-u| \;,\; |v'-v|\,\right],\; u' = (u^2+2\epsilon)^{\frac{1}{2}} \\ \text{and} \qquad & \\ P_+ &= \min\left[\,(u'+u) \;,\; (v'+v)\,\right],\; v' = (v^2-2\epsilon)^{\frac{1}{2}} \end{aligned}\right\} \qquad (7)$$

where u' and v' are the post binary-collision speeds of the target and projectile following transfer of energy ϵ. The binary-encounter approximation is apparently good for cases involving large energy-change ϵ, and is more suitable for ionization rather than for discrete excitation. However, the close agreement displayed in Fig. 6 between the Born and binary encounter approximations possibly results from the fact that many final angular momentum states ℓ' contribute to $Q_{n,n'}$, an instance well suited to quasi-classical descriptions. Moreover, application of (6) required much less computer time than that involved in the Born approximation, partly because individual angular momentum states ℓ and ℓ' need not be considered as required in Born's approximation.

(b) <u>$n \to n+1$ Transitions for large n</u>: The situation, however for $n \to n+1$ collisional transitions which involve relatively small energy-changes for large n is not quite as clear as above. As Fig. 3 indicates, two distinct sets of peaks emerge in both the form factors and electron-atom cross sections. One set occurs for $\Delta\ell = \ell' - \ell \approx 0$ while the other set is evident around $\ell' \to 6 - 8$. As ℓ increases, the two sets merge and yield relatively larger form factors and cross sections. This is further reflected in Fig. 4 which gives the $(10 - 11\ell')$ ℓ-averaged cross section (4) as a function of ℓ'.

The origin of this behavior can be explained. For large $n \approx n'$, the radial orbitals are almost similar in both magnitude and range (in contrast to that for the cases $n' >> n >> 1$). Maximum overlap is obtained when <u>all</u> the <u>innermost</u> lobes are in phase and almost coincide, as happens when $\ell \approx \ell'$ as in Fig. 5.

As ℓ' increases, the lobes of the final orbital move inwards with increasing phase difference between the orbitals. Maximum overlap is again attained when the outermost oscillations of both the initial and final orbitals are almost out of phase by π, or in phase as for the (11,6) and (11,7) final orbitals $(n'\ell')$ respectively in Fig. 6. With further increase of ℓ', the number of oscillations in the final orbitals (11,8) - (11,10) becomes reduced and cancellation occurs thereby yielding small overlap with the 10s state. The overlap in (1) is further modulated by $\exp(i\underset{\sim}{K}\cdot\underset{\sim}{r})$ which can be expanded in terms of spherical Bessel functions $j_{\ell''}(kr)$ which, for a typical value of the momentum change K, supresses any of the small overlap contribution which arises from the inner lobes of 10s and (11,6) orbitals, as in Fig. 6.

(c) H(1s) - H(nℓ) Collisions: Because of the absence of a singularity in the integrand of (2) as $K \to 0$, the behavior of single transitions in atom-atom collisions is expected to correlate more closely (than e-atom collisions) with the variation displayed in Fig. 1 for the inelastic form factor characterizing the single transition. This expectation is confirmed (Flannery and McCann[18]), when the range of momentum-change K important to the collisional transition is relatively large, as in $4 \to 5$ and $10 \to 20$ transitions. However, for $n \to n + 1$ transitions with n large, the relevant K are much smaller such that $K\,|T^{B}_{e\ell}(K)|^2$ in (2) controls events. This factor (cf Eq. (3)) increases initially as K thereby amplifying the overall rise of the inelastic form factors in Fig. 3. The increase may also be sufficiently strong so as to offset the fall-off in the form factors of Fig. 3. The associated cross sections should therefore, in this instance, display an overall increase with ℓ' rather than a peak at some value of ℓ' as appears in the inelastic form factor. Fig. 7 supports this contention and also shows that the magnitudes are fairly insensitive to the value ℓ of the initial angular momentum. The cross sections when averaged over the n values of

ℓ increase with ℓ', as illustrated by Fig. 7.

5.4 CONCLUSIONS

For $n \rightarrow (n+1)$ collisional transitions with large n, the initial and final orbitals have similar magnitude and range, and two distinct peaks in the inelastic form factor are noted. These are attributed to instances when significant overlap occurs for the following two cases: (a) when $\ell' \gtrsim \ell$ is such that the innermost lobes yield the significant contribution, and (b) when ℓ' is such that the outermost oscillations of the initial and final orbitals are either out of phase by π or almost in phase, both of which generally occur within a change of unity in ℓ'. This second peak may not occur due to limited ℓ', in which instance an overall rise is noted until $\ell' = (n'-1)$. Further increase of ℓ', if available, beyond the second peak of case (b), involves continuous reduction in overlap and the inelastic form factor falls off quite sharply.

This behavior is further reflected in the excitation cross sections for e-atom collisions. For single transitions in atom-atom collisions, however, the elastic form factor describing the incident atom whose state is left unchanged is such that it offsets any decrease with ℓ' of the inelastic form factor describing the target. The cross sections then exhibit an overall increase as ℓ' is increased from 0 to $(n'-1)$.

Apart from providing some insight into various systematic properties of $n\ell \rightarrow n'\ell'$ collisional transitions, a related purpose of this paper and the previous paper is therefore to express a cautionary note in arbitrarily following the tacit assumption (valid only in the limit of high impact speeds) that only those transitions with dipole character i.e., $\ell' = \ell \pm 1$ are the strongest at all energies and are the only ones that require calculation.

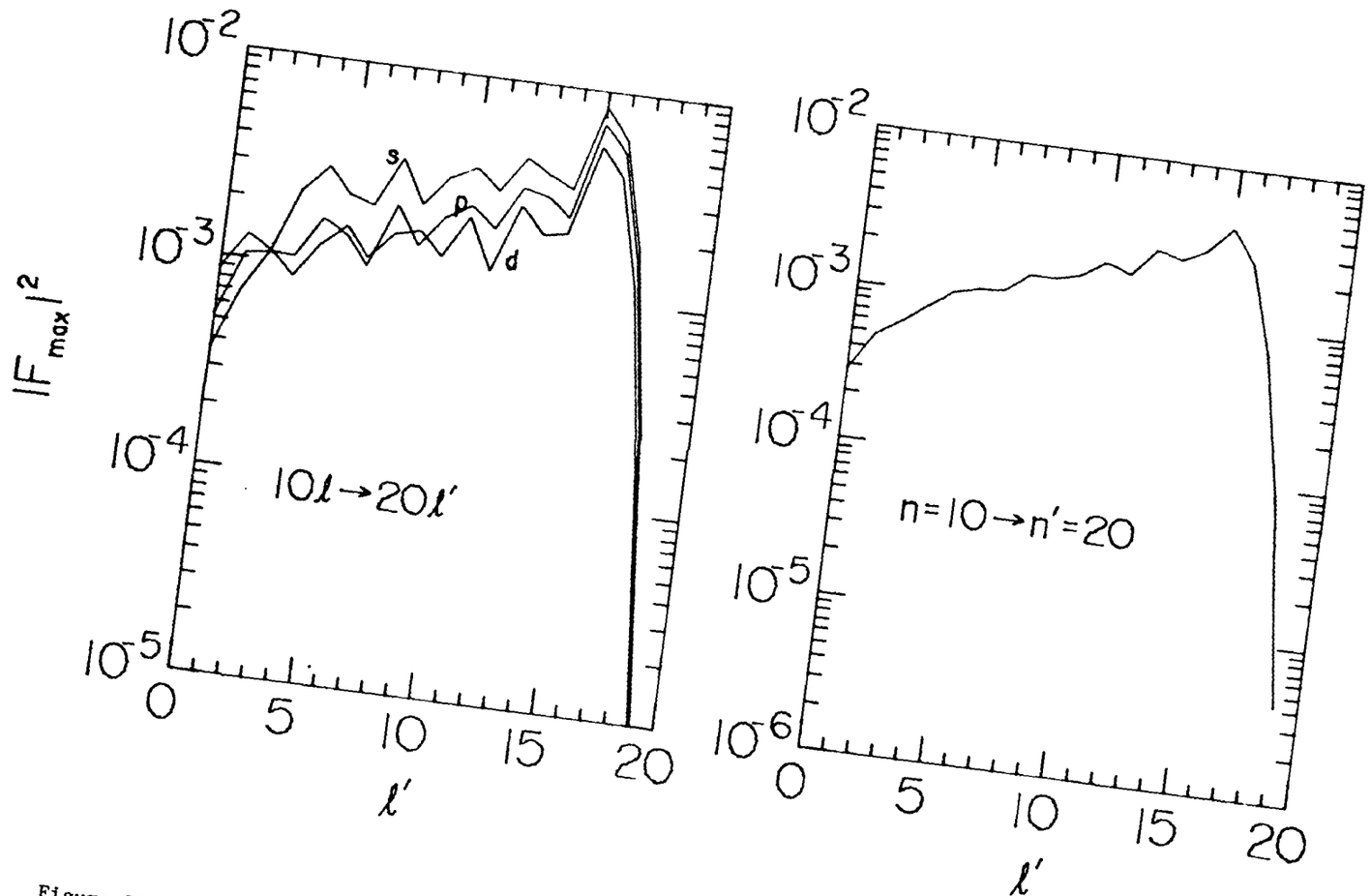

Figure 19. Variation with final angular momentum ℓ' of the peak of the inelastic form factor unaveraged and averaged over ℓ for $10\ell \rightarrow 20\ell'$ transitions.

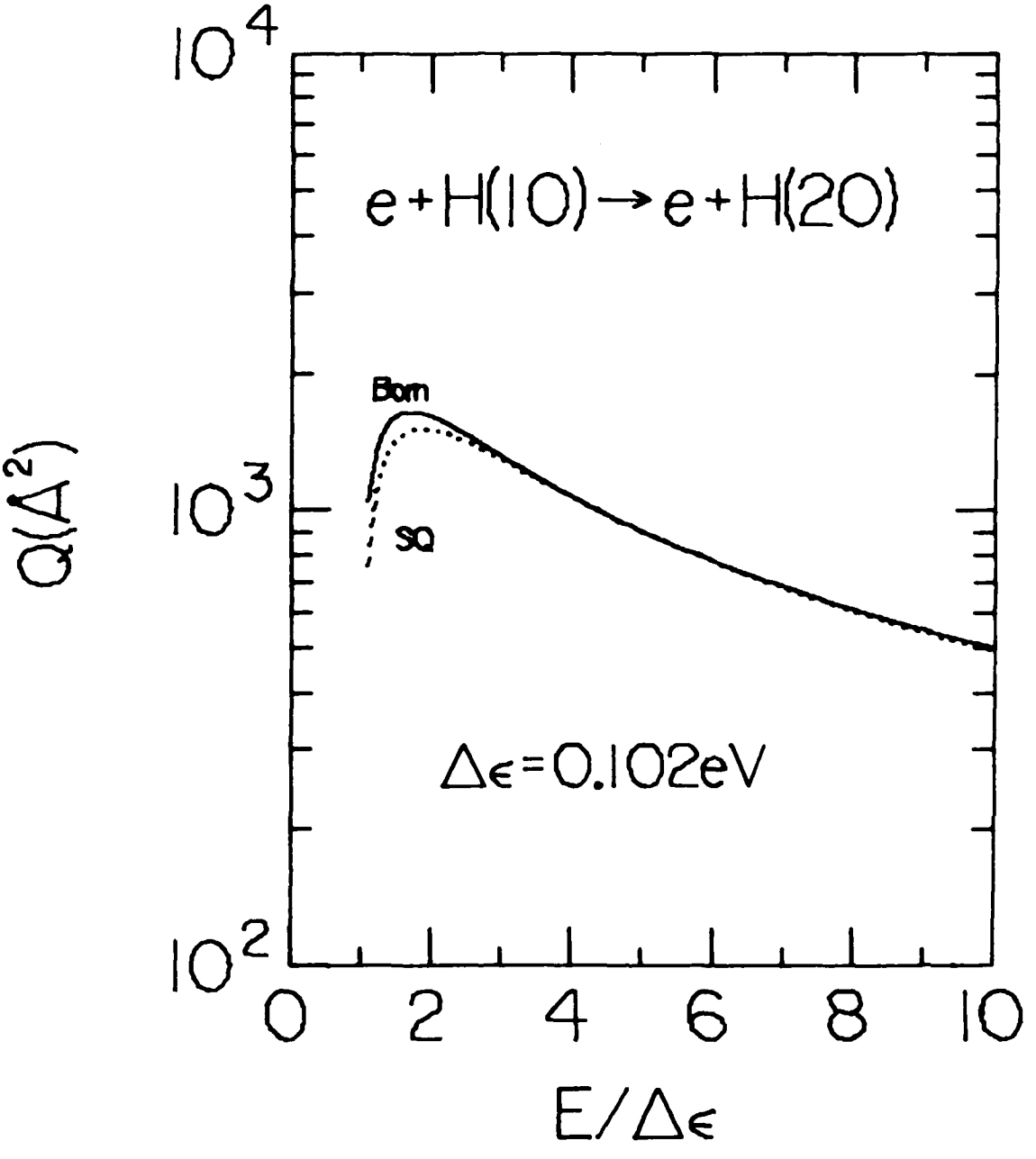

Figure 20. Cross section (A^2) for 10 → 20 transitions as a function of electron-impact energy E in units of the energy Δε of transition. ____ Born approximation. --- Binary encounter approximation SQ.

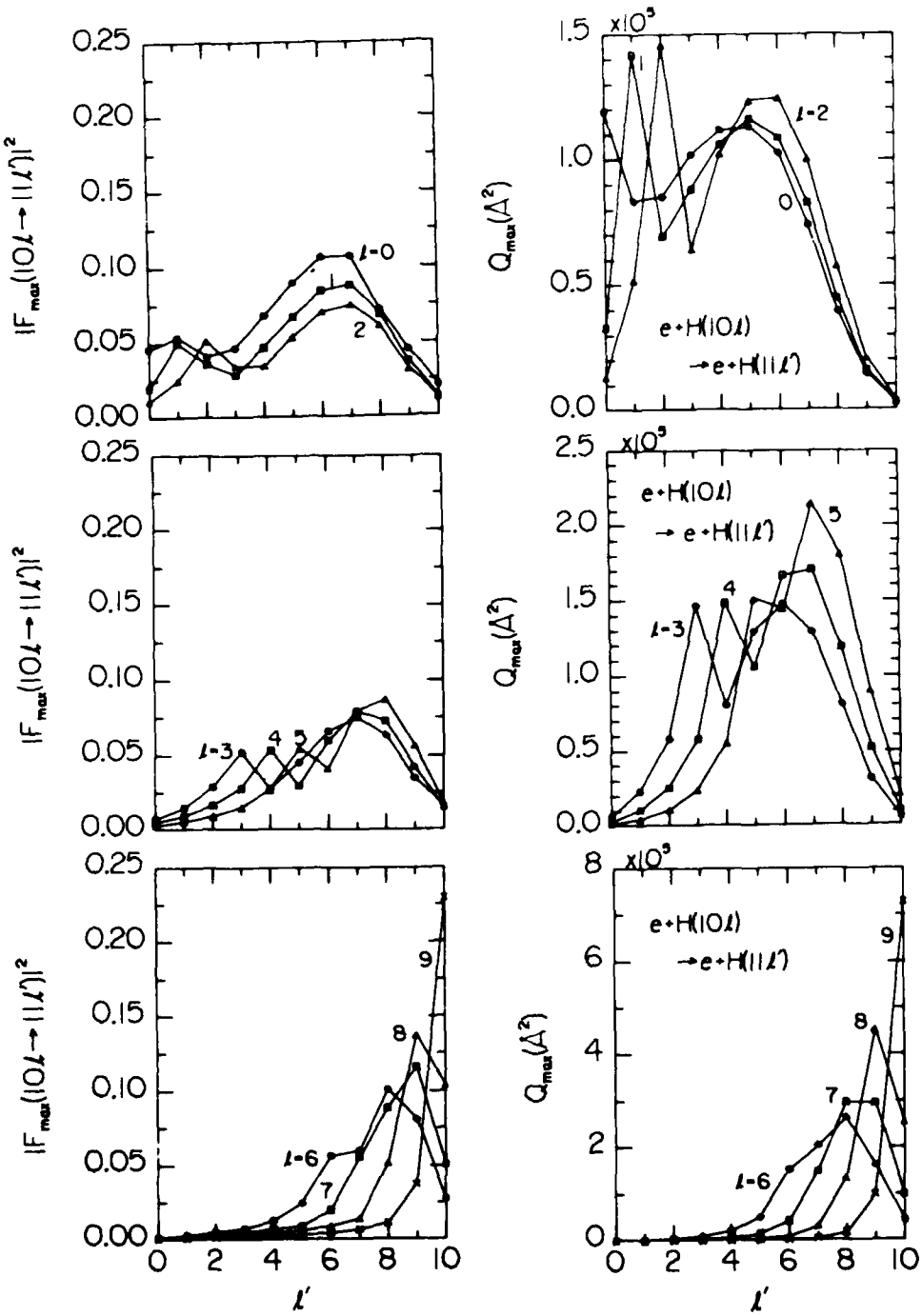

Figure 21. **Maximum form factors and maximum electron-impact cross sections for $10\ell \rightarrow 11\ell'$ transitions.**

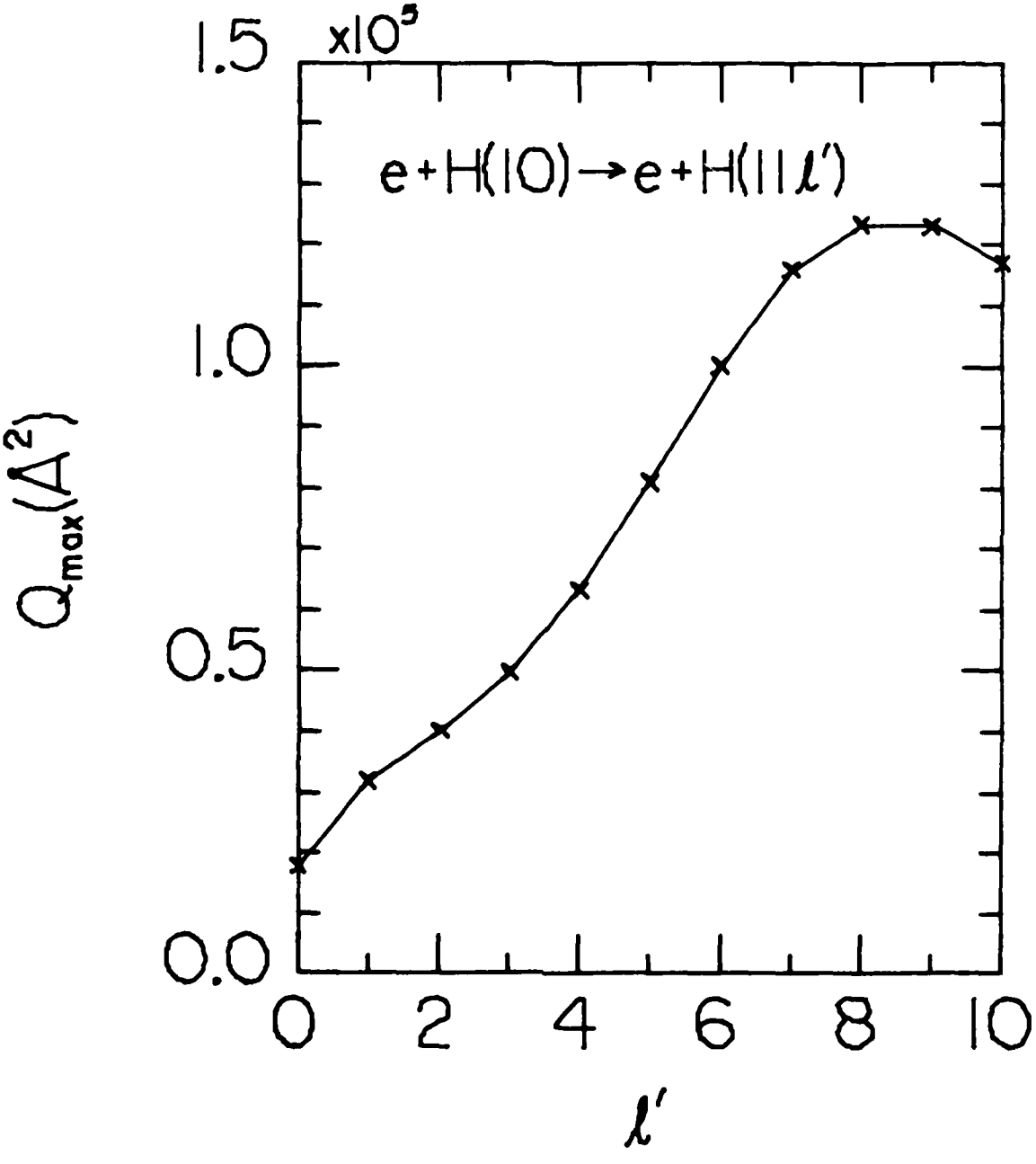

Figure 22. Maximum electron-impact cross section (averaged over initial ℓ-values for 10 → 11ℓ' transitions as a function of ℓ'.

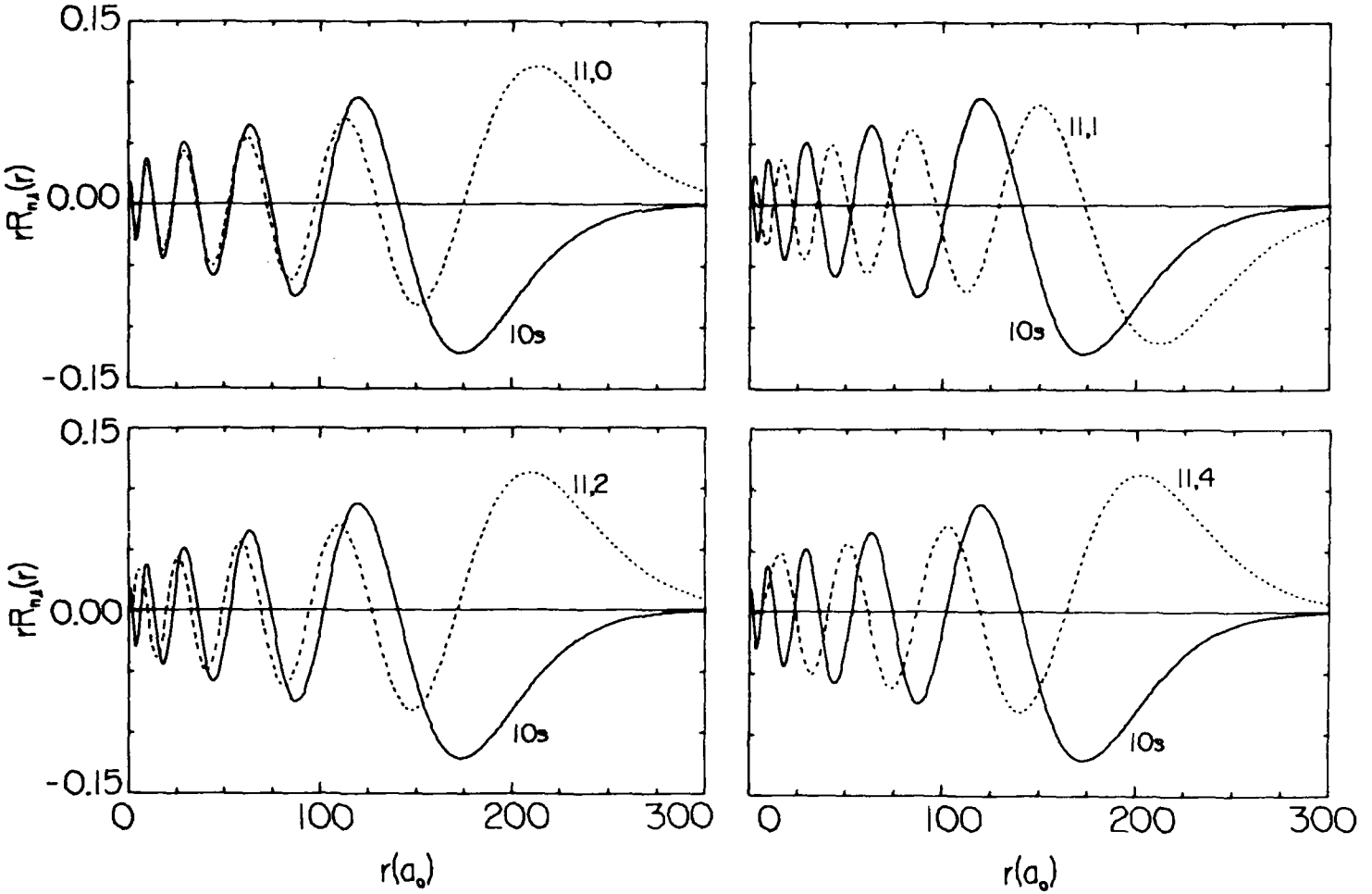

Figure 23. The 10s and 11ℓ' hydrogen radial orbitals $R_{n\ell}(r)$ times r in configuration space. Note inward shift of the 11ℓ' orbital as ℓ' is increased. Large overlap is attained between 10s and 11s orbitals.

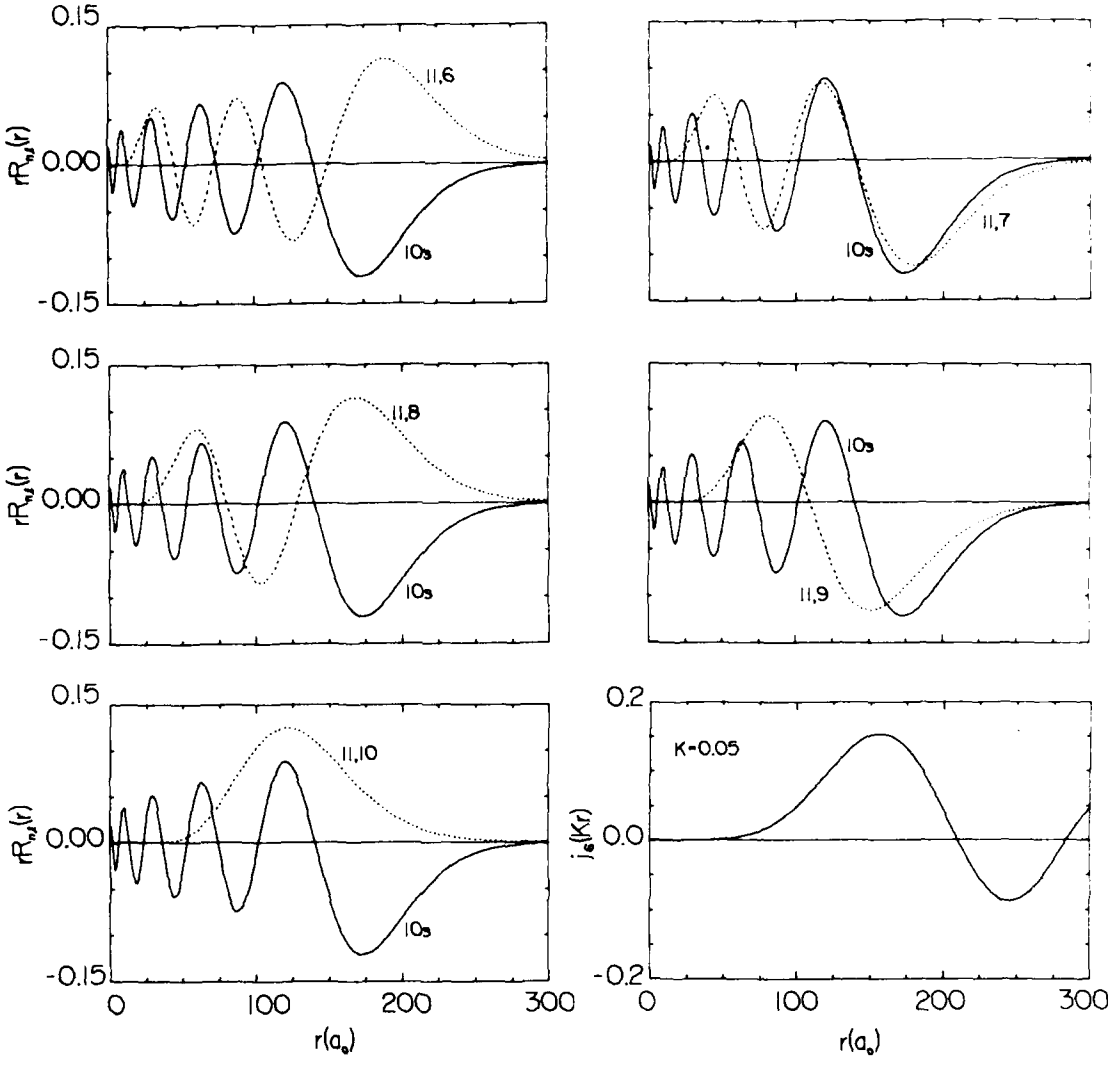

Figure 24. **As in Figure 5. Maximum overlap is attained between 10s and 11(ℓ' = 6 and 7) orbitals. Variation of the spherical Bessel function $j_6(Kr)$ which modulates the 10s - 11(ℓ' = 6) overlap is also illustrated.**

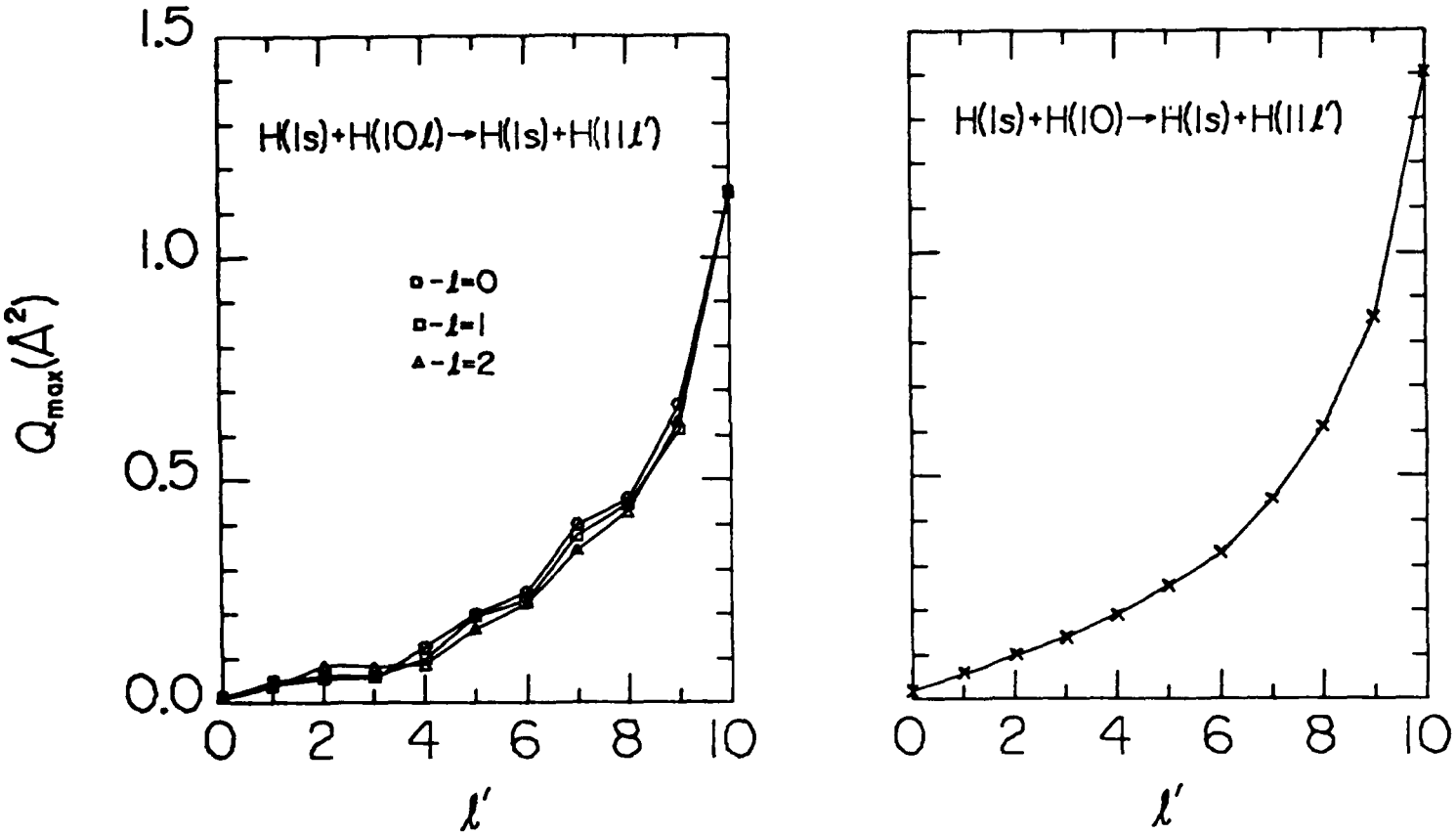

Figure 25. Maximum cross sections (unaveraged and averaged over ℓ) for 10ℓ → 11ℓ' transitions in H(1s) - H(10ℓ) collisions.

SECTION VI

ATOMIC AND MOLECULAR COLLISION PROCESSES IN RARE GAS-HALIDE LASERS AND RARE-GAS EXCIMER LASERS.

In this section, the key cycles of atomic and molecular collision processes contributing to the formation and quenching of the excited molecular states in exciplex (such as KrF^*) and excimer (such as Xe_2^*) laser systems are delineated and discussed in detail.

6.1 Excimers and Exciplexes: Background

During the past few years there has been remarkable progress[24-26] achieved in the development of a new class of gas lasers which, by electronic transitions, operate at ultraviolet to visible wavelengths and which are the first type outside the infrared lasers to demonstrate efficient scaling to high single pulse energy and high average power. This class of high efficiency lasers is based on an interesting class of molecules generally known as excimers, such as Xe_2^* or KrF^* which are molecular complexes bound in an excited electronic state but unstable in the ground electronic state. Heteronuclear excimer species as KrF^* are more accurately classified as "exciplexes" while "excimer", derived from excited dimer (formed from two identical species), is reserved for homonuclear constituents as Xe_2^*. The lasing transitions originate on the excited bound molecular states and terminate on dissociative (or weakly bound) ground states.

Recognition that the excited states of rare gas excimers or of rare gas-halide exciplexes not only have high electronic energies but also can be efficiently populated, and the advantage of the repulsive ground state for extraction of laser energy provide key ingredients for laser action. Typical times for dissociation of the lower repulsive ground level are $\sim 10^{-12}$s, extremely brief relative to radiative lifetimes 10^{-9}-10^{-6}s of the upper excited states so that automatic population inversion can be created and maintained without the limitation of bottlenecking.

Figs. 1 and 2 illustrate general characteristics of a rare-gas excimer (Xe_2^*) and a rare gas-halide ($RgH\ell^*$) exciplex respectively. The common feature is the existence of bound excited molecular states and repulsive (or only weakly attractive) ground states. While the lowest excited states of Xe_2^* are strongly covalent over all internuclear distances R, the lowest excited states of the

rare gas-halides $RgH\ell^*$ are predominantly ionic ($Rg^+ - H\ell^-$) in character over an extensive range of R. This general distinction is reflected in different channels (ion or neutral) for population of the excited states.

At low densities ($\sim$ several Torr) of the rare gas, the laser (bound-free) emission forms a rather broad undulating continuum while sharper and narrower emissions are produced at much higher pressures ($\sim$ 1 atm). The higher vibrational levels which are populated and decay radiatively at low pressures are rapidly quenched to low vibrational levels (0-2) by three-body collisions at higher pressures. Energy pathways for a given system are dependent not only on gas pressure and temperature but also on the method used to pump the laser. Since the emissions in both the excimer and rare gas-halide systems are broad, $\sim$ 200 Å and 100 Å respectively, the cross sections for stimulated emission are low $\sim 10^{-17}$-10^{-18} cm^2 (relative to 10^{-15}-10^{-12} cm^2 for bound-bound atomic or molecular transitions with comparable linestrengths). Vigorous pumping is therefore required to ensure excited state densities sufficient for laser action, and this is achieved in general by three methods.

(A) In gas-discharge lasers, low-energy electrons mainly suffer elastic collisions with the rare gas and lose little energy. By drifting along an applied electric field they gain energy sufficient for direct excitation of the excited states of the rare-gas atoms. Various atomic and molecular processes mainly involving ground and excited-state neutrals are then responsible for the production and destruction of the excited excimers. Discharge (self-extinguishing) instability which results from arbitrary increase in the electric field can be eliminated by introduction of an electron-beam so as to restore the balance between the discharge ionization rate and the electron-loss rate due to dissociative recombination and attachment. High pumping efficiency and high average power is obtained by this electron-beam sustained discharge.

(B) In electron-beam pumped lasers, a high-intensity keV or relativistic electron-beam deposits a large fraction of its energy in ionization of the rare gas. The excited molecular states are then populated by collision processes in general different from these in (A) and scaling to high pulse-energy and average-power require detailed optimization of many factors; some are atomic and molecular and some are technical ($\vec{e}$-beam technology, optics and materials). Increase of the intensity of the $\vec{e}$-beam is accompanied by a more complex sequence of atomic and molecular processes.

(C) In nuclear-pumped lasers a pulsed nuclear reactor generates a high intensity pulse of neutrons which interact with the nuclear species in the laser gas to produce high-energy charged projectiles, which in turn ionize and excite the laser gas in a manner similar to that in (B).

The above types of lasers provide rich sources of extremely interesting atomic and molecular collision processes involving excited electronic and vibrational states, a research subject about which relatively little is known. The delineation of these processes, to be discussed below, is pivotal towards development of a realistic kinetic model which will eventually fully characterize the detailed response of these "laser" systems to action of the energy-pump under certain conditions.

6.2 Rare Gas-Halide Lasers

Fig. 2 illustrates the relevant potential-energy curves for various combinations of rare gases Rg and halides Hℓ. The ground electronic Σ and Π states, in general repulsive, dissociate into covalent products while the B, C and D excited states have strong ionic character with dissociation energy $\sim$ (5-6) eV. The unique feature here is the relatively close balance between the ionization potentials $I^* \sim$ (4-5) eV of Rg^* in its metastable level and the electron-affinity EA $\sim$ (3-3.5) eV of the halides Hℓ (F, Cℓ, B, I) such that the (Rg^* - Hℓ) covalent asymptotic energy level (I^* - EA) lies $\sim$ 1 eV below the ionic (Rg^+ - $H\ell^-$) asymptote. The crossing point determined by equating the R^{-1}-Coulombic attraction with (I^* - EA) in eV, is

$$R_x\ (\mathring{A}) = \frac{14.35}{(I^* - EA)} \qquad (1)$$

which is therefore large $\sim$ (20-60) $\mathring{A}$. Curve crossings are therefore highly improbable and the dissociation products of the B, C and D states are mainly (Rg^+ - $H\ell^-$) ion pairs (as for NaCℓ in its ground state). Typical values of R_x are given in Table 1 for various (Rg^+-$H\ell^-$) combinations.

The first excited level of the halides $H\ell^*$ is also relatively high for special cases. The asymptotic level for (Rg - $H\ell^*$) is well above the (Rg^+ - $H\ell^-$) level for ArF^*, KrF^* and XeF^* (efficient laser-systems) and is just below for $XeC\ell^*$ and $XeBr^*$. The levels for Ne -($C\ell^*$, Br^*, I^*) and for Ar -(Br^*, I^*) all lie in the vicinity of the potential minimum of the B state, thereby allowing rapid predissociation into rare gas-excited halide products without any excimer laser action. This predissociation is however, an efficient source of production of I^* used in other lasers.

The rare gas-halide systems at high pressure that have already produced laser

action and oscillation are ArF^* (193 nm), KrF^* (248 nm), $KrCl^*$ (222 nm), XeF^* (352 nm), $XeCl^*$ (308 nm) and $XeBr^*$ (282 nm), while fluorescence has been observed for $ArCl^*$ (170 nm), $KrBr^*$(206 nm) and XeI^*(252 nm); in accord with the above considerations. While a two component Ar (1-4 atm)/F_2(<1%) mixture is used for ArF^* lasers, the remaining cases associated with heavier rare gases generally involve an additional lighter rare gas as a buffer, normally Ne or Ar, because of the reduced three-body quenching by the lighter gas. For the longer wavelength $XeHl^*$ cases, Ne is chosen because of the reduced absorption by Ne_2^+ versus Ar_2^+ , subsequently formed, while Ar is used for KrF^* and $KrCl^*$. It is also worth noting from Fig. (2) that NeF^* has sufficient internal energy to ionize Xe by a Penning ionization-type process.

In the following discussion on the relevant atomic and molecular processes, we adopt for illustrative purposes available rates and cross sections from previous compilation,[24-26] bearing in mind that while much useful information has recently become available for the structural properties of homonuclear and heteronuclear rare gas molecules, comparatively little is known about the collisions involving excited electronic and vibrational states in general, and that some guesses to the rates have been deduced.

6.3 Formation, Quenching and Absorption Processes for Rare Gas-Halides

6.3.1 $\vec{e}$-beam Pumped Lasers: ArF^*

When high-energy electron beams excite (Ar/F_2) mixture at high pressure, a few ion-channels are selectively favored over the many neutral-neutral channels normally associated with rare gas excimers. Lasing transitions originate on the first excited molecular states of ArF^*, ($B\ ^2\Sigma^+_{1/2}$, $C\ ^2\Pi_{1/2}$ and $D\ ^2\Pi_{3/2}$ without spin-orbit coupling as in Hund's case (a), or III 1/2, II 1/2 and IV 1/2 including spin-orbit coupling as in Hund's case (c)), formed from $Ar^+\ (^2P_{1/2,3/2}) + F^-\ (^1S_o)$ and they terminate on the purely dissociative $X\ ^2\Sigma^+$ and $A\ ^2\Pi$ ($\equiv$ X 1/2 and I 3/2, II 1/2) states with covalent products $Ar(^1S_o) + F(^2P_{1/2,3/2})$. The UV-transitions in order of decreasing strengths are B → X, the strong laser-emission with bandwidth ∿ 100 Å, D → X and C → A which is very weak. These upper levels are populated directly by the ion-ion recombination process,[28-32]

$$Ar^+ + F^- + Ar \rightarrow ArF^*\ (B,C,D) + Ar; \quad \alpha \simeq 3\ 10^{-6}\ cm^3\ S^{-1} \text{ at 1 atm.} \qquad (2)$$

with a rate ($\alpha\ N^+N^-$) $cm^{-3}\ S^{-1}$ where N^+ and N^- are number densities of positive ions Ar^+ produced by electron-impact ionization,

$$\vec{e} + Ar^{(*)} \rightarrow \vec{e} + Ar^+ + e_s \qquad (3)$$

of Ar in the ground and metastable levels, and negative ions F^- formed at a rate k_{DA} by (endothermic) dissociative attachment,

$$e_s\ (\sim 1\ eV) + F_2 \rightarrow F + F^-\ ;\ k_{DA} \sim 2\ 10^{-9}\ cm^3\ S^{-1} \qquad (4)$$

of the slow ejected e_s in (3) with F_2. The recombination rate α increases with gas density N, reaches a maximum $3\ 10^{-6}\ cm^3\ S^{-1}$ at ∿1 atm and then decreases.[28-32]

At gas pressures beyond 2 atm, Ar^+ are rapidly converted to Ar_2^+ by ion-atom association

$$Ar^+ + Ar + Ar \rightarrow Ar_2^+ + Ar \; ; \; k_{IA} \sim 2\ 10^{-31}\ cm^6\ S^{-1} \tag{5}$$

at a rate $(k_{IA}\ N^+N^2)\ cm^{-3}\ S^{-1}$. The upper excited states are therefore populated at an effective two-body rate $\alpha\ cm^3S^{-1}$ by ion-ion recombination,

$$Ar_2^+ + F^- + Ar \rightarrow (Ar_2^+\ F^-)^* + Ar \begin{cases} \rightarrow ArF^* + 2Ar & (6a) \\ \rightarrow Ar_2F^* + Ar & (6b) \end{cases} ; \; \alpha = 3\ 10^{-6}\ cm^3\ S^{-1}$$

in which dissociative electron-transfer

$$[Ar_2^+ - F^-]^* \rightarrow ArF^* + Ar \tag{7a}$$

in the quasi-bound triatomic system stabilizes (6a). According to measurements of Rockni et al.,[33] the channel (6a) is much more probable than (6b). The stable configuration for Ar_2F^* is triangular so that formation of Ar_2F^* requires confinement of the trajectory of F^- in (6b) to the plane normal to the symmetry axis. Process (7a) can occur in isolation for free ion-pairs slowed by the gas, at rates considerably enhanced $\sim 10^{-6}\ cm^3\ S^{-1}$ over those ($\sim 10^{-7}\ cm^3\ S^{-1}$) in the absence of gas.

For typical concentrations $N^{\pm} \sim 10^{15}\ cm^{-3}$ of positive and negative ions, recombination proceeds in a time scale of 1 ns , to be compared with the radiative lifetime of $\sim$ 4 ns for the $B\ ^2\Sigma - X\ ^2\Sigma^+$ transition. At higher gas densities N, the speed of ion-ion approach becomes limited by random diffusion and mobility in the gas such that α decreases with N. Moreover for $N \geq 6\ 10^{19}\ cm^{-3} \equiv 2$ atm, the time scale for conversion of atomic to molecular ions is $T \sim (k_{IA}\ N^2)^{-1} \geq 1$ ns which with increasing N becomes much shorter than the time for $(Ar^+ - F^-)$ recombination (2). Also the rate of

$$Ar_2^+ + F^- \rightarrow ArF^* + Ar \qquad (7b)$$

for free ion-pairs will become quite competitive with (6a) which decreases with N. Although (7b) is a "two-body" process, its rate will increase with N since the gas will effectively reduce the speed of approach of the ions so as to promote more efficient curve crossing. This enhanced efficiency will however be eventually offset by the reduced approach speed.

For typical F_2- concentrations $N(F_2) \sim 10^{-2}\ N \simeq 3\ 10^{17}\ cm^{-3}$, attachment (4) occurs in a timescale of 2 ns. Slow electrons are also lost with a rate $k_{DR}\ cm^{-3}\ S^{-1}$ by <u>dissociative recombination</u>,

$$e_s + Ar_2^+ \rightarrow Ar^* + Ar\ ;\ k_{DR} \sim 8.5\ 10^{-7}\ cm^2\ S^{-1} \qquad (8)$$

with Ar_2^+ formed at high pressures by (5). The excited atomic states A^* so produced rapidly relax to the metastable and ground levels for possible recycling in (3) or else form excimers Ar_2^*.

So that attachment (4) of electrons with number density n_e proceeds faster than dissociative recombination

$$n_e\ N(F_2)\ k_{DA} >> n_e\ [N_2^+]\ k_{DR} \simeq n_e^2\ N^2\ k_{DR}\ k_{IA}\ T \qquad (9)$$

where the concentration $[N_2^+]$ of diatomic ions are formed from $N^+ \simeq n_e$ atomic ions by (5) in time T. The effective rates of dissociative attachment and dissociative recombination vary therefore as n_e and n_e^2 respectively. With $n_e \sim 3\ 10^{15}\ cm^{-3}$ associated with an ionization pumping rate 10^{24} ions $cm^{-3}\ S^{-1}$ in (2) and with T ~ 1-10 ns, (9) is easily satisfied. If this pumping rate and/or (1-4) atm. neutral pressure are exceeded, then dissociative recombination becomes important and new pathways resulting from formation of rare gas excimers Ar_2^* and from "harpoon" reactions assume increasing significance.

Excited atomic states Ar^* originate from electron-impact excitation

$$\vec{e} + Ar \rightarrow \vec{e} + Ar^* \tag{10a}$$

by the $\vec{e}$-beam, from dissociative recombination (8) (when important) and from mutual-neutralization (cf Fig. 2)

$$Ar^+ + F^- \rightarrow Ar^* + F \tag{10b}$$

the rate for which can be considerably enhanced to $\sim 10^{-6}$ cm^3 S^{-1} by the presence of third bodies (see § 4). At high N, the excimer Ar_2^* is produced at a rate k_3 cm^6 S^{-1} by the three-body atom-atom recombination process,

$$Ar^* + Ar + Ar \rightarrow Ar_2^* \ (^{1,3}\Sigma) + Ar; \ k_3 \simeq 10^{-32} \ cm^6 \ S^{-1} \ . \tag{11}$$

New channels for formation of ArF^* are now entered via the "harpoon" reactions,[11]

$$Ar^* + F_2 \rightarrow (Ar + F_2^-)^* \rightarrow ArF^* + F \ , \ k_H \sim 7.5 \ 10^{-10} \ cm^3 \ S^{-1} \tag{12}$$

which occurs with a large cross section ~ 150 $\mathring{A}^2$ (see § 4) and

$$Ar_2^* + F_2 \rightarrow (Ar_2^+F_2^-)^* \rightarrow ArF^* + Ar + F \ . \tag{13a}$$

$$\rightarrow Ar_2F^* + F \ . \tag{13b}$$

At sufficiently high gas densities N however, Ar_2^* excimer-formation occurs more readily than (12). When the Ar_2^* excimer channel is an important source of the ArF^* exciplex, then all the kinetic pathways for the formation and destruction of the pure rare-gas excimers must be considered e.g., loss of atomic and molecular metastables by electron-impact ionization,

$$e + \begin{cases} Ar^* \\ Ar_2^* \end{cases} \rightarrow 2e + \begin{cases} Ar^+ \\ Ar_2^+ \end{cases} \ , \tag{14}$$

by associative ionization,

$$Ar + Ar^* \rightarrow Ar_2^+ + e \tag{15}$$

by Penning ionization

$$Ar^* + Ar^* \rightarrow Ar^+ + A + e \quad , \tag{16a}$$

$$Ar_2^* + Ar_2^* \rightarrow Ar_2^+ + 2A + e \tag{16b}$$

and by photoabsorption. This chain of events is separately discussed in § 6.5 on pure excimer lasers. The rare gas ions produced by (14) - (16) undergo ion-ion recombination (2) and (6) with formation of ArF^*. At high N, the 193 m laser radiation is absorbed by photodissociation of Ar_2^+, and of Ar_3^+ produced by

$$Ar_2^+ + 2\ Ar \rightarrow Ar_3^+ + Ar \tag{17}$$

Fig. 3 summarizes the main energy pathways for ArF^* exciplex formation via three-body recombination and harpoon reactions. It also illustrates the important quenching and photoabsorption processes. In addition to spontaneous radiative decay,

$$ArF^* \rightarrow Ar + F + h\nu \quad (\sim 193\ nm) \tag{18}$$

in 4 ns, the excited states of ArF^* are quenched by two-body collisions,

$$ArF^* + F_2 \rightarrow Ar + 3F, \quad k_{2Q}^{(1)} \sim 1.9\times10^{-9}\ cm^3\ s^{-1} \tag{19}$$

which, even for $N(F_2) \lesssim 10^{-2}\ N(Ar)$ remains faster than

$$ArF^* + Ar \rightarrow 2\ Ar + F, \quad k_{2Q}^{(2)} \sim 9\times10^{-12}\ cm^3\ s^{-1} \tag{20}$$

but becomes slower than the three-body process,

$$ArF^* + 2Ar \rightarrow Ar_2F^* + Ar, \quad k_{3Q} \sim 5\times10^{-31}\ cm^6\ s^{-1} \tag{21}$$

which is the dominant quenching mechanism for gas pressures $\gtrsim$ 1.5 atm.

Absorption of 193 nm-radiation with cross section σ_ν arises mainly from photodetachment

$$h\nu + F^- \rightarrow F + e \ , \quad \sigma_\nu^{(1)} \sim 9.3\times10^{-18} \text{ cm}^2 \tag{22}$$

from photodissociation,

$$h\nu + Ar_2^+ \rightarrow Ar + Ar^+ \quad \sigma_\nu^{(2)} \sim 5\times10^{-17} \text{ cm}^2 \tag{23}$$

and in situations when the excimer Ar_2^* chain is entered, from photoionization:

$$h\nu + Ar_2^* \rightarrow Ar_2^+ + e \quad \sigma_\nu^{(3)} \sim 4\times10^{-18} \text{ cm}^2 \tag{24}$$

and possibly from

$$h\nu + Ar^* \rightarrow Ar^+ + e \ , \sigma_\nu^{(4)} \sim 10^{-20} \text{ cm}^2 \tag{25}$$

involving mainly metastable Ar^* since the higher excited electronic states have relaxed by emission and collision. Cross sections for the above four photoabsorption processes[35-39] are displayed as a function of wavelength in Figs. 4-7. Note that, in contrast to the cross sections for photoionization of the molecular metastables, those for photoionization of atomic metastables are much smaller and display transmission windows at wavelengths associated with the rare gas-halide laser emissions.

6.3.2 $\vec{e}$-beam Pumped Heavier Rare Gas Lasers: KrF^*, XeB^*, $XeC\ell^*$, XeF^*

As noted above, laser efficiency of the heavier rare gas-halide systems is enhanced by using a lighter buffer gas as Ne or Ar so that three-body quenching process as (21) is considerably reduced e.g., the three-body quenching of KrF^* is ten times less with Ar than with Kr. As indicated by Fig. 5, the absorption by Ar_2^+ of 248 nm radiation from KrF^* is much less than by Ne_2^+, such that Ar is preferred as a buffer. With Xe-halides, a Ne-buffer is indicated. With these systems the energy pathways are somewhat similar, and KrF^* can be considered as a model. However, Xe-halide lasers are inherently less efficient since the ground state is bound (fairly weakly by 225 cm^{-1} for $XeC\ell$ and relatively strongly by 1100 cm^{-1} for XeF) originating from increased configuration interaction between the pure ionic excited and ground covalent states. The bound state in XeF can accomodate vibrational levels resulting therefore in less efficient laser energy extraction. Moreover, in contrast to ArF^* and KrF^*, the C-level in XeF^* is much lower than the B-level, the origin of the laser $B \rightarrow X$ transition. Also, as illustrated in Fig. 2, NeF^* has sufficient internal energy to ionize Xe, thereby providing an additional quenching mechanism.

In the mixture (Ar > 90%/Kr < 10%/ < 1% F_2) at high pressures (1-4 atm.), production channels for ArF^* and KrF^* can be considered as proceeding quite independently of one-another via ion-ion recombination, harpoon reactions and (depending on the current density of the $\vec{e}$-beam) via entry into the excimer cycle. Fig. 8 illustrates the two distinct sequences (similar to ArF^* formation in isolation) and the coupling between sources of ArF^* and KrF^*. Coupling between the two cycles is achieved (1) by the displacement reaction

$$ArF^* + Kr \rightarrow KrF^* + Ar \ , \qquad (26)$$

which is endothermic and which produces KrF^* directly, (2) by charge-transfer,

$$Ar_2^+ + Kr \rightarrow Kr^+ + 2A \ , \tag{27}$$

which in turn produces KrF^* via $(Kr^+ - F^-)$ recombination, and (3) by energy-transfer

$$Ar_2^* + Kr \rightarrow Kr^* + 2Ar \ , \tag{28}$$

which yields KrF^* following harpoon reactions with F_2.

The vibrational distribution of KrF^* is determined by a sequence of events illustrated in Fig. 9. Recombination in general produces initially ion-pairs in highly excited vibrational levels v, which subsequently become vibrationally relaxed by collisions

$$ArF^* (v) + Ar \rightarrow ArF^* (v_i) + Ar \tag{29}$$

to levels v_i. These levels, characterized by long radiative lifetimes can further relax or else undergo displacement reactions

$$ArF^* (v_i) + Kr \rightarrow KrF^* (v_f) + Ar \tag{30}$$

populating in general higher excited vibrational levels v_f which in turn are relaxed by

$$KrF^* (v_f) + Ar \rightarrow KrF^* (v) + Ar \tag{31}$$

to levels $v \sim 0\text{-}2$ which radiate to the ground electronic state. A critical step for laser efficiency is to ensure that the lower vibrational levels of KrF^* are populated by vibrational relaxation at a rate faster than the rate of extraction of laser energy.

Ion-ion recombination, displacement and harpoon reactions produce KrF^* in the B, C and D electronic states which are mixed by collision with electrons, Ar and Kr. Details of this mixing are at present not fully understood.

The utility of (27) and (28) requires the entry of the excimer channel,

implying therefore sufficient high-density of Ar and current density of the electron-beam. These efficient coupling mechanisms are illustrated in Fig. 8 together with an interesting sequence,

$$Kr^+ + 2Ar \rightarrow ArKr^+ + Ar \qquad (32)$$

and

$$ArKr^+ + F^- + (Ar) \rightarrow KrF^* + Ar + Ar \qquad (33)$$

The chief mechanisms for quenching KrF^* and absorbers of 248 nm radiation are summarized in Fig. 10. As before, the three-body collisions,

$$KrF^* + Kr + Ar \rightarrow Kr_2F^* + Ar \qquad (34)$$

and

$$KrF^* + Ar + Ar \rightarrow ArKrF^* + Ar \qquad (35)$$

eventually quench KrF^* more rapidly at high pressures $\gtrsim$ 1.5 atm. than the process

$$KrF^* + F_2 \rightarrow Kr + 3F \qquad (36)$$

which is important at low and intermediate pressures and which is much more efficient than direct dissociative de-excitation of KrF^* by Ar and by electrons.

The main absorbers are F^-, Ar_2^+, Kr_2^+, Ar_2^*, Kr_2F^* produced by (31) and Ar_2F^* produced by

$$ArKrF^* + Ar \rightarrow Ar_2F^* + Kr \qquad (37)$$

and by the harpoon-reaction

$$Ar_2^* + F_2 \rightarrow Ar_2F^* + F \quad . \qquad (38)$$

6.3.3 Gas-Discharge Rare Gas-Halide Lasers

Here the emphasis is on low-energy electrons which gain sufficient energy from an applied electric field so as to excite the high pressure mixture rare gas atoms Rg^* ($\equiv Ar^*, Kr^*$) by electron-impact,

$$e + Rg \rightarrow e + Rg^* \tag{39}$$

The metastables so produced undergo harpoon reactions,

$$Rg^* + F_2 \rightarrow RgF^* + F \tag{40}$$

with the formation of KrF^* and ArF^* which in turn is linked to KrF^* by a displacement reaction, as before. The high density of atomic metastables required for exciplex formation imply a rapid rate for the ionization process,

$$e + Rg^* \rightarrow Rg^+ + 2e \tag{41}$$

thereby resulting in electron-avalanche causing (self-extinguishing) discharge instability. Cross sections obtained for (41) by Ton-That and Flannery[41] are large ($\sim 10^{-15}$ cm^2). With sufficient F_2-density, this electron production is partially offset by dissociative attachment (via a resonance)

$$e + F_2\ (v=0) \rightarrow (F_2^-)^* \rightarrow F + F^- \tag{42}$$

so that the ion-ion ($Rg^+ - F^-$) channel can now be entered for the production of RgF^*.

In descending order of importance, the main mechanisms for electron cooling are excitation (Rg^* production) (39), electron-impact dissociation

$$e + F_2 \rightarrow (F_2^-)^* \rightarrow e + F + F \tag{43}$$

which also tends to offset the loss via (42) of higher-energy electrons, elastic

electron-neutral collisions,

$$e + Rg^{(*)} \rightarrow e + Rg^{(*)} \tag{44}$$

and ionization of Rg^* in (41).

Electron-electron collisions will also influence the electron-energy distribution once the fractional ionization exceeds a certain limit ($\sim 10^{-6}$) thereby approaching a weakly-ionized plasma. Although cross sections for vibrational excitation

$$e + F_2\ (v=0) \rightarrow e + F_2\ (v) \tag{46}$$

are relatively large ($\sim 10^{-17}$ cm^2), the energy loss per collision is relatively small ($\sim$ 0.1 eV). The main advantage of (46) is however, the production of vibrationally excited $F_2(v)$ permitting dissociative attachment

$$e + F_2\ (v) \rightarrow F + F^- \tag{47}$$

at a rate more rapid than (42). Thus (46) and (47) together enhance considerably the electron loss. Nighan[42] has recently performed detailed studies of discharge instability.

When electron-beams are used to sustain the discharge, atomic ions Rg^+, are formed directly and, at high pressures, are converted into molecular ions Rg_2^+ which in turn dissociatively recombine with the low-energy electrons producing Rg^*. The excimer Rg_2^* and F_2-harpoon channels could then be entered as before in Figs. 3 and 8 with the formation of RgF^*.

In summary, therefore, the primary source of RgF^* in fast pulse or $\vec{e}$-beam controlled discharge are reactions between Rg^* and F_2, in contrast to pure $\vec{e}$-beam excitation when the ion-ion channels is the main source of production. However, depending on circumstances, ion-ion recombination can provide comparative contributions in the former case, while dissociative recombination and

entry into the pure excimer channel can become important in the latter case.

4.4 Three-Body Ion-Ion Recombination, Mutual Neutralization and Harpooning

Ion-ion recombination is therefore of central significance to rare gas-halide lasers pumped by $\vec{e}$-beams and of some importance to discharge lasers under certain circumstances. At low gas densities the basic mechanism can be explained with the aid of Fig. 11. The positive and negative ions, Ar^+ and F^- for example, accelerate towards one another from infinite separation under the action of their mutual Coulombic attraction. In the absence of gas atoms (third bodies) the ions simply follow their Coulomb trajectory until sufficiently close separation for the crossing of the Coulomb potential with the covalent potential describing the direct interaction of Ar^* and F. Electron-transfer (or mutual neutralization)

$$Ar^+ + F^- \rightarrow Ar^* + F \ , \quad k_M(N=0) \simeq 2\ 10^{-7}\ cm^3\ S^{-1} \tag{48}$$

can therefore occur with a certain probability mainly arising at the crossing point $\simeq 20\ \overset{o}{A}$; otherwise the ions simply continue to their distance of closest approach, then separate to distances where (48) has another chance and on to infinity. Note the above rate k_M is given for zero concentration N of gas atoms.

Introduction of third bodies however allows the possibility of collisions between third bodies and ion-pairs with relatively large separations R. Due to the strength and long-range of the ion-ion Coulombic interaction, the relative kinetic energy of the ion-pair has doubled when the ions approach each other to within

$$R_T = \frac{2}{3}\ \frac{e^2}{kT} \simeq 370\ \overset{o}{A}\ \text{(at room temperature)} \tag{49}$$

By collision with thermal gas atoms, the energy of superthermal ion-pairs will be reduced on average and bound ion-pairs in excited vibrational and

rotational levels are formed. Electrons in the laser plasma quench the rotational excitation very efficiently, particularly in the presence of strong dipoles (as ArF^*). Further collisions cause tighter binding (vibrational relaxation), weaker binding (vibrational excitation) and even dissociation which has important consequences for eventual mutual neutralization (48). The ion-pairs in general proceed up and down the vibrational-energy ladder (discrete and continuous), and, in the absence of any sinks a Saha-Boltzmann equilibrium would be attained between the free and bound ion-pairs, the number of free-bound transitions balancing the number of bound-free dissociations between given energies. Ion-pairs $ArF^*(v)$, particularly those in very low vibrational levels v are lost by spontaneous radiative decay (18) to the repulsive ground electronic state and by three-body collisional quenching (21), both of which are very rapid, assumed here for simplicity of discussion to be instantaneous. Radiative decay of the highly excited vibrational levels is negligible in comparison to the more rapid vibrational relaxation with gas atoms. The presence of the sink at low v, inhibits the full development of Saha-Boltzmann equilibrium such that there is a net flow of ion-pairs down the energy ladder until sufficient binding is obtained so as to insure rapid electron-transfer in bound ion-pairs in low levels v. The range of these low v becomes manifest by the transition from hydrogenic vibrational levels $\sim 1/v^2$ to levels normally associated with a harmonic (or anharmonic) oscillator $\sim (v + \frac{1}{2})$ with nearly constant separation between neighboring levels. Radiative decay of these lower vibrational levels and further vibrational relaxation occur much faster than any permissible vibrational excitation or dissociation. The radiative sinks (via stimulated or spontaneous laser extraction) and quenching sinks are irreversible and the ion-pairs are irretreviably lost to the recombination process. With rare gas mixtures, displacement reactions occur and sinks are illustrated in Fig. 7.

Not only does the above sequence of events provide some insight into the

mechanism by formation of ArF^* but it has extremely important consequences for the loss of free ion-pairs via mutual neutralization.

Degradation of the internal speed u of a free ion-pair via direct free→free and indirect free→bound (high v) →free transitions implies that a free ion-pair has substantially increased the probability P for mutual neutralization (48) which ≈ exp(-A/u) [1 - exp(-A/u)] (cf Flannery[8]) by curve crossing over that met in the absence of third bodies. With this increased probability the effective rate for (48) will therefore increase with N from its value $\sim 10^{-7}$ cm^3 S^{-1} at zero gas density. By means of a computer experiment, Bates and Mendas[43] have demonstrated that values as high as (1-2) 10^{-6} cm^3 S^{-1} can be attained for mutual neutralization in the pressure range ($\frac{1}{10}$ - 1) atm, depending on the initial value at N=0 and, as a result, were the first to recognize the importance of this possibility. The increase in the rate of mutual neutralization with N is eventually subdued by the overall decrease in Pu. The excited states Ar^* so produced however undergo harpoon reactions (12) with F_2 such that ArF^* is formed, the mutual neutralization process being an intermediate step between the ion-ion channel and the eventual production of ArF^*.

With increasing gas density N, the third body effectively utilizes the many ion-ion superthermal encounters that occur at large separations ≤ 370 Å as collisions which eventually contribute to mutual neutralization (in marked contrast to the much smaller separations (10-20 Å) associated with mutual neutralization in the absence of a third body). This statement is also true for ion-ion recombination and essentially is the basis for large rates $\sim$ (1-5) 10^{-6} cm^3 S^{-1} for both these processes at pressures ∼ 1 atm.

In general, the rates for population and destruction of highly vibrational levels v (which are closely packed and can be therefore regarded as forming a continuum) are very rapid in comparison with the slow rate at which the net number density of level v is changing. The cluster of highly excited levels therefore act as a conduit through which the majority of ion-pairs from the continuum (and which eventually terminate in recombination) must flow. The loss-rate of

free ion-ion pairs is therefore equal to the rate of production of the lowest levels which in turn are rapidly depopulated by radiative decay (18) to the repulsive ground electronic state and by further three-body collisions (21) with the formation of Ar_2F^*.

Let

$$K_{if}\, dE_f \equiv K(E_i, E_f)dE_f \tag{49}$$

be the microscopic rate that a collision between an ion-pair and a third body changes the internal energy of an ion-pair from E_i to between E_f and $E_f + dE_f$ i.e., for the process,

$$(Ar^+ - F^-)_{E_i} + M \rightarrow (Ar^+ - F^-)_{E_j} + M,\ E_{i,f} \lesssim 0 \tag{50}$$

which therefore proceeds at an overall rate $(n_i dE_i)\ N\ (K_{if}\, dE_f)\ cm^{-3}\ s^{-1}$ where $n_i\, dE_i$ is the number density of ion-pairs within the energy interval dE_i about E_i and N is the concentration of third bodies M.

The recombination rate is the net flow of ion-pairs past some arbitrary negative energy level E_A and is, with the aid of Fig. 11 , given by

$$-\frac{dN^{\pm}}{dt} = \alpha\, N^+N^- = N\left[\int_{E_A}^{\infty} n_i\, dE_i \int_{E_D}^{E_A} K_{if}\, dE_f - \int_{E_A}^{\infty} dE_i \int_{E_S}^{E_A} n_f\, K_{fi}\, dE_f\right] , \tag{51}$$

the net balance of the downward R↓ and upward R↑ flows (in energy) respectively. The dissociation energy of the lowest level is $(-E_D)$ and E_S is the negative energy of the level at which the recombination is stabilized at the lower v by electron-transfer. The probability of upward flow past this level is assumed negligible compared with the rapid irreversible depletion of the lower levels by (B → X) radiative decay and by three-body collisional quenching, both of which are here assumed to occur instantaneously relative to the time scale for recombination. A more elaborate collisional-radiative model can however be developed (following the lines of Bates, Kingston and McWhirter[44] ,) so as to

remove this assumption.

The rate of growth with time t of ion-pairs in level i significant to the recombination process is given by

$$\frac{\partial n_i(E_i,t)}{\partial t} = N \left[\int_{E_S}^{\infty} n_f K_{fi} \, dE_f - n_i \int_{E_D}^{\infty} K_{if} \, dE_f \right] \tag{52}$$

in which explicit account is taken both of the inability of those ion-pairs with energy $E < E_S$ to be excited to E_i and of the possibility that ion-pairs be degraded directly past E_S by collision. This (infinite) set of integro differential equations is solved subject to the boundary conditions that

$$n_i = \begin{cases} \tilde{n}_i \, , & E_i > 0 \\ < \tilde{n}_i \, , & E_S < E_i < 0 \\ 0 \, , & E_i < E_S \end{cases} \tag{53}$$

where $\tilde{n}_i$ is the number density of ion-pairs in Saha-Boltzmann equilibrium. A quasi-equilibrium treatment follows by setting $\frac{\partial n_i}{\partial t}$ in (52) zero since, for the high levels i, n_i remains effectively constant during the short time scale (1-10 ns) for recombination to proceed.

In the process,

$$Rg^+ + F^- + Rg \rightarrow RgF^* + Rg \; ; \; Rg \equiv He, Ne, Ar, Kr, Xe \tag{54}$$

(the range of the Coulombic interaction is much longer than the ion-neutral interaction), and so the three-body collision can be separated into the individual binary-encounters

$$Rg^+(f) + Rg(s) \rightarrow Rg(f) + Rg^+(s) \tag{55}$$

in which symmetrical resonance charge transfer occurs between a fast positive ion and a thermal neutral, and

$$F^-(u_i) + Rg(u_o) \rightarrow F^-(u') + Rg(u_o') \qquad (56)$$

in which an elastic (and momentum-change) collision changes the speed of F^- from u_i to u_i' and Rg from u_o to u_o'. The charge-transfer process (55) is a very efficient mechanism for energy reduction since it essentially interchanges the velocity vectors of the positive ion and neutral atom i.e., it converts a superthermal ion into one essentially thermal.

By simple extension of previous work (Bates and Moffett[45], Bates and Flannery[46],) the rate coefficient K_{if} for (54) can be formulated as a four-dimensional integral. With this knowledge, Flannery and Yang[47] solved subject to (53), the integral equation (52) with LHS equal to zero for $n_i(E)$ which are then inserted in (51) to yield α, the recombination rate. Results at 300 K are given in Table 2 and are applicable only to the linear N low-density region.

In a rather elegant paper, Bates and Mendas[48] have provided further basic understanding of the extension to somewhat higher densities of this type of quasi-equilibrium treatment, nonlinearity with N being introduced by treating incoming ion-pairs separately from outgoing ones. The procedure however requires solution to two coupled integro-differential equations for the density n(E,R) variation with E and R, followed by a triple integration for α, provided the rates K_{if} are known (generally from a four-dimensional integral). Although prohibitive to direct application, this procedure represents a key pivotal development in studies of recombination in the intermediate density region. Bates and Mendas[20] have presented an interesting method based on a Monte-Carlo type computer experiment applicable to all densities N.

Reasonable estimates based on intuitive models, or else on models constructed so as to reproduce the end result of a rather complicated sequence of events, are also available.[29-32]

While emphasis has been placed on a series of weak collisions with third bodies effecting recombination, Thomson[13] assumed that one single strong collision alone was responsible. As the ions approach each other from infinity to within mutual separation R, their relative kinetic energy T, as depicted in Fig. 11, increases from a thermal value $\frac{3}{2}$ kT to

$$T_R = \frac{3}{2} kT + \frac{e^2}{R} \tag{57}$$

Thomson conjectured that, upon collision with a thermal neutral, this gain (e^2/R) was lost (a reasoning somewhat consistent with symmetrical resonance charge-transfer encounter with a thermal atom) such that the total energy of relative motion

$$E_{rel} = \frac{3}{2} kT - \frac{e^2}{R} \tag{60}$$

can become negative for separations,

$$R \leq R_T = \frac{2}{3} \frac{e^2}{kT} \simeq 370 \text{ Å (at room temperature)} \tag{61}$$

Eventual electron-transfer in these bound ion-pairs completes the recombination at a rate

$$\alpha = \pi R_T^2 \bar{v}_{rel} P(R_T,N) \tag{62}$$

where $\bar{v}_{rel}$ is an averaged thermal relative speed of the ions and $P(R_T,N)$ is the probability that an ion-pair with internal separation within R_T collides with an atom of the gas of density N. While assignment of P is subject to discussion, an important feature here is the recognition that ion-pairs with separations as large as R_T are potential candidates for three-body ion-ion recombination. However, a realistic assignment to R_T can only be effected after the detailed collisional history of the ion-pairs is first established as by a quasi-equilibrium

treatment such as described above and in more mathematical detail elsewhere.[2] Bates and Flannery[46] have shown for equal mass constituents (for which the Thomson treatment was designed) that the Thomson assignment at low gas densities is fairly realistic in that the one strong collision required for recombination is effectively equivalent to the net balance of the many weak collisions involving free bound, bound bound deexcitation and excitation, and dissociation (even temporarily).

As N is raised, the Thomson probability P for an (ion-pair)-neutral collision increases as N (predicted also by the low density quasi-equilibrium treatment), enters a nonlinear dependence with N and finally approaches an asymptotic value of unity, roughly at STP, such that the limit at high densities is

$$\alpha \to \pi R_T^2 \tilde{v}_{rel} \sim 2\ 10^{-6}\ cm^3\ S^{-1} \tag{63}$$

with a thermal speed $\tilde{v}_{rel} \sim 5\ 10^4$ cm S^{-1}. This rate, although yielding the correct order of magnitude at STP is nevertheless quite incorrect in its asymptotic independence with N.

The reason for this failure is that the recombination is governed by the rate of ion-ion approach which, as N is raised, becomes slow compared to the frequency of collision with third bodies. Langevin[50] had much earlier provided the high density limit (at hundreds of atmospheres) by reasoning that the ions approached one another through a viscous medium composed of third bodies under the influence of their mutual electric field (e/R^2) such that the radial drift speed of approach is given in the "mobility limit"

$$v_d(R) = (K^+ + K^-)\ \frac{e}{R^2} \tag{64}$$

where K^+ are the mobilities of the ions in the gas density N. Recombination was then assured upon radial passage through the surface of a sphere of arbitrary radius R_A such that

$$\alpha = 4\pi R_A^2 v_D(R_A) = 4\pi e(K^+ + K^-) . \tag{65}$$

which varies as N^{-1}. This expression apparently works at pressures (several atms) for which it was not intended (cf Bates[51], Flannery[28])

Natanson[52] has constructed a bridge between the microscopic low-density approach of Thomson and the macroscopic Langevin- limit for the special case of equal mass ions moving with identical mean free paths in a gas of atoms with mass equal to the mass of the individual ions. Flannery[29] has recently generalized (and corrected) this treatment for arbitrary masses and mean free paths, and results[29-32]

$$Ar^+ + H\ell^- + Ar \rightarrow ArH\ell^* + Ar \; ; \; H\ell \equiv F, C\ell, B, I \tag{66}$$

$$\left.\begin{aligned} Rg^+ + F^- + Rg &\rightarrow RgF^* + Rg \\ Rg_2^+ + F^- + Rg &\rightarrow [Rg_2F]^* + Rg \end{aligned}\right\} \tag{67}$$

and

$$\left.\begin{aligned} Kr^+ + F^- + Rg &\rightarrow KrF^* + Rg \\ Kr_2^+ + F^- + Rg &\rightarrow [Kr_2F]^* + Rg \end{aligned}\right\} \tag{68}$$

with Rg ≡ He, Ne, Ar, Kr and Xe are reproduced in Figs. 12-16. In general, the rates are large as expected and tabulations are available.[29-32]

The main mechanism for population of the exciplexes in gas-discharge lasers is the harpoon reaction

$$Kr^* + F_2 \rightarrow (Kr^+F_2^-)^* \rightarrow KrF^* + F \qquad (69)$$

Here Kr^* uses its valence electron as a harpoon to pull in F_2. An ion-pair $Kr^+F_2^-$ is then formed by Coulombic attraction, and ejection of F stabilizes the formation of KrF^*. The $(Kr^* - F_2)$ potential curve crosses the $(Kr^+ - F_2^-)$ Coulombic potential at (cf. Table 1)

$$R_x(\mathring{A}) = \frac{14.35}{I(Kr^*) - EA(F_2)} \simeq 14.35\ \mathring{A} \qquad (70)$$

implying a large cross section for production of KrF^*. The ionization potential I(eV) of Kr^* ($\sim$ 4 eV) exceeds the electron affinity EA(eV) of F_2, ($\sim$ 3 eV) so that at infinite separation R the charge transfer is endothermic (cf. Fig. 2). Formation of a quasi-bound ion-pair can occur however via the kinetic energy gained from the growing Coulomb attraction between the approaching reactants.

6.5 Rare Gas Excimer Lasers

Rare gas excimers are pumped by $\vec{e}$-beams although fluorescence in rare gas discharges has been observed. In contrast to the rare gas-halide systems, pure excimer lasers rely mainly on neutral-neutral rather than ion-ion channels for production of excited states. Fig. 17 illustrates the main sequence of collision processes.

The $\vec{e}$-beam excites and ionizes the gas (e.g. Ar) by

$$\vec{e} + Ar \rightarrow \vec{e} + Ar^+ + e_s \qquad (71)$$

$$\rightarrow \vec{e} + Ar^* \qquad (72)$$

The atomic ions are rapidly converted by ion-atom association into molecular ions

$$Ar^+ + 2Ar \rightarrow Ar_2^+ + Ar \; ; \quad k_{IA} \sim 2\ 10^{-31}\ cm^6\ s^{-1} \tag{73}$$

which then undergo dissociative recombination

$$e_s + Ar_2^+ \rightarrow Ar^{**} + Ar \; ; \; k_{DA} \sim 2\ 10^{-7}\ cm^3\ s^{-1} \tag{74}$$

with the secondary electrons of (71). Radiative decay of the excited states so formed to the ground state is inhibited because the atomic radiation is trapped at the high gas pressures, such that Ar^{**} relaxes by collision or radiation to the $^3P_{0,2}$ metastable levels or to the $^{1,3}P_1$ resonance levels, all denoted by Ar^*.

Excimers are then produced by the three-body (rate limiting) process

$$Ar^* + 2Ar \rightarrow Ar_2^* \; (^{1,3}\Sigma_u) + Ar \; ; \; k_3 \approx 10^{-32}\ cm^6\ s^{-1} \tag{75}$$

in either a $^1\Sigma$-state (or 0_u^+ in Fig. 1) of short radiative lifetime ($\sim$ 5 ns) or in a slightly lower lying $^3\Sigma$-state (or 0_u^-, 1_u) of somewhat longer radiative lifetime (from $\sim$ 100 ns for Xe_2^* to (1-3) μs for Ar_2^*). The lower $^3\Sigma_u$ state, which acts as a reservoir and absorber, can be mixed with the upper laser $^1\Sigma_u$ state mainly by collision with electrons

$$e + Ar_2^* \; (^3\Sigma_u) \rightleftarrows e + Ar_2^* \; (^1\Sigma_u) \tag{76}$$

and with heavy particles

$$Ar + Ar_2^* \; (^3\Sigma_u) \rightleftarrows e + Ar_2^* \; (^1\Sigma_u) \tag{77}$$

The excimer formation (75) is one of the rate limiting steps in the chain occuring in a time ($\sim$250 ns at 1 atm) which decreases as N^{-2}. The atomic and molecular metastables are collisionally quenched by direct ionization,

$$e + Ar^*_{(2)} \rightarrow Ar^+_{(2)} + 2e \ , \tag{78}$$

by <u>electron-impact dissociation</u>

$$e + Ar_2^* \rightarrow e + 2Ar \tag{79}$$

and possibly by <u>associative ionization</u>,

$$Ar^* + Ar \rightarrow Ar_2^+ + e \tag{80}$$

Provided the metastable densities are sufficiently large so that collisions can occur within a time short compared to the radiative lifetimes (particularly for the $^3\Sigma_u$ state), <u>Penning-type ionization processes</u>

$$Ar^* + Ar^* \rightarrow Ar + Ar^+ + e \tag{81}$$

and

$$Ar_2^* + Ar_2^* \rightarrow Ar_2 + Ar_2^+ + e \tag{82}$$

would be important quenching mechanisms.

In addition the rare gas excimers can be photoionized by absorption of their own radiation. While cross sections in Fig. 6 for photoionization of atomic metastables

$$h\nu + Ar^* \rightarrow Ar^+ + e \tag{83}$$

are not only comparatively small ($\lesssim 10^{-19}$ cm^2) but also exhibit a pronounced minimum in the neighborhood of excimer wavelengths, the cross sections for photoionization of the excimer as in Fig. 7 for

$$h\nu + Ar_2^* \ (^{1,3}\Sigma_u) \rightarrow Ar_2^+ + e \tag{84}$$

are in general an order of magnitude larger ($\sim 10^{-18}$ cm^2).

The energy distribution of the electrons ejected in the initial ionization process (71) is determined from (71), (78)-(82) and (84). The cross sections for ionization of the atomic and molecular metastables are displayed in Figs. 19-21.

In addition to affecting the rates for the above atomic and molecular processes, high gas temperature excites high vibrational levels of Ar_2^*, thereby widening the emission band with a consequent decrease in gain. Also under high temperatures, ground state atoms can approach each other along the repulsive potential curve to sufficiently close separations whereby they can absorb radiation. The energy pathways for mixtures of rare gases are quite similar to those illustrated in Fig. 17 for a pure rare gas.

6.6 Summary

In summary, we have delineated and discussed the various atomic and molecular collisions processes which play a central role in the kinetics of rare gas-halide exciplex and rare gas excimer laser systems. We have stressed the importance of processes involving excited atomic and molecular states. Although knowledge of these processes is growing, much remains to be done in the development of theoretical treatments of processes involving excited states.

Table 10: Distances (Å) where ion-ion Coulomb potential for $Rg^+ - (Hℓ^-, Hℓ_2^-)$ crosses covalent $Rg^* - (Hℓ, Hℓ_2)$ straight-line potential.

Rg \ Hℓ	F	C	Br	I	F_2	O_2	Br_2	I_2
He	11	12	10	9	9	6	6	7
Ne	9	11	9	8	8	6	6	6
Ar	18	24	17	13	13	8	8	9
Kr	21	30	20	14	14	8	9	10
Xe	32	63	30	18	19	10	11	11

AD-A086 698 GEORGIA INST OF TECH ATLANTA SCHOOL OF PHYSICS F/G 20/5
CROSS SECTIONS FOR IONIZATION OF RARE GAS EXCIMERS BY ELECTRON --ETC(U)
MAR 80 M R FLANNERY, K J MCCANN F33615-78-C-2028
UNCLASSIFIED AFWAL-TR-80-2015 NL

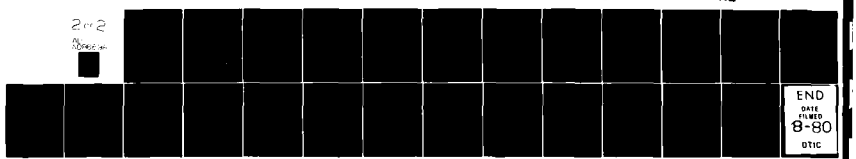

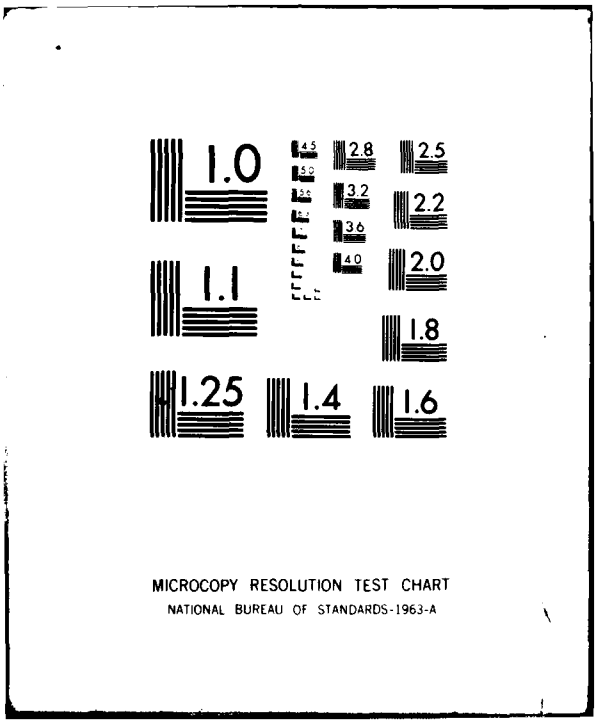
1.0
1.1
1.25
1.4
1.6
1.8
2.0
2.2
2.5
2.8
3.2
3.6
4.0
4.5
5.0
MICROCOPY RESOLUTION TEST CHART
NATIONAL BUREAU OF STANDARDS-1963-A

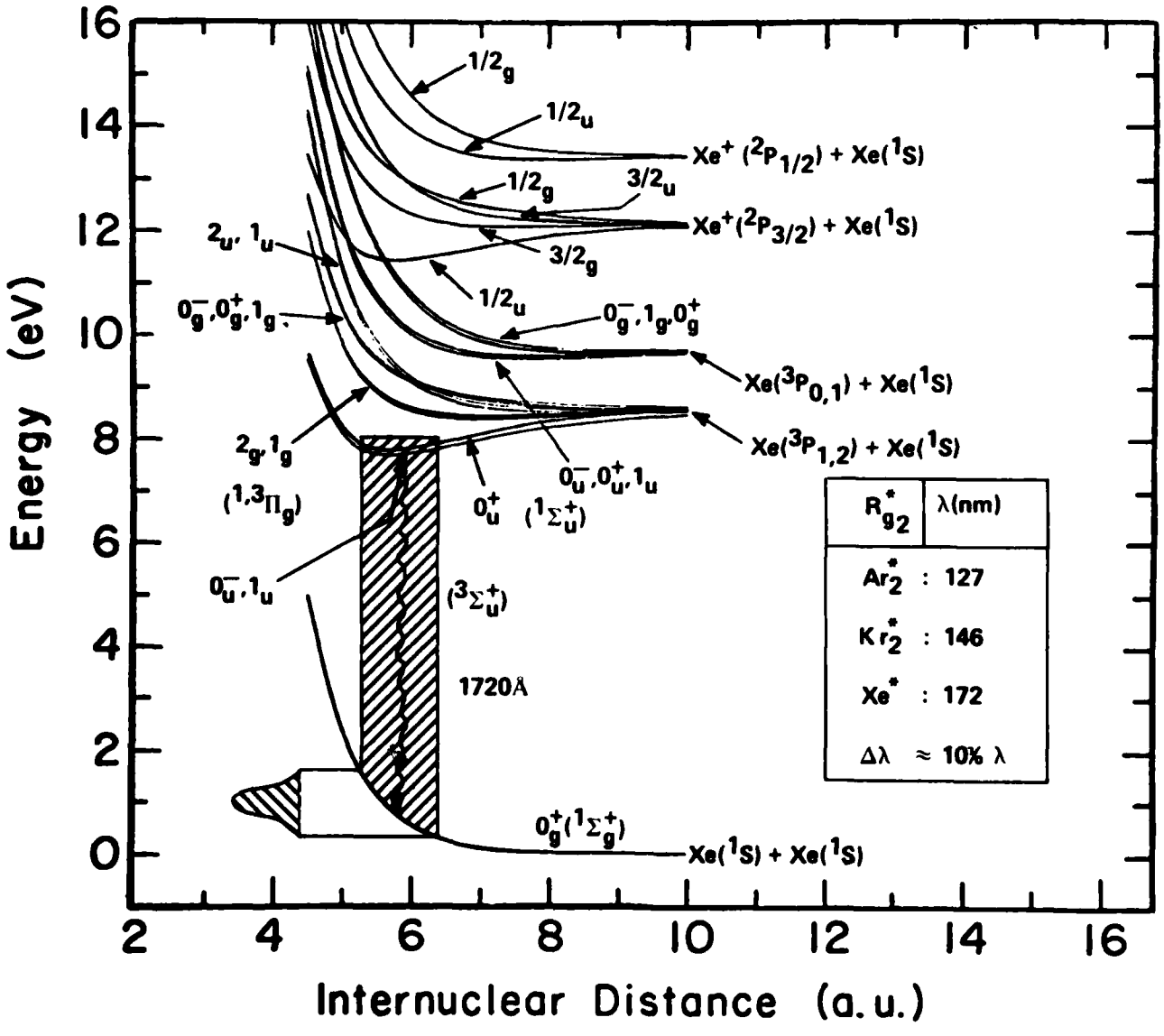

Figure 26. Potential energy curves relevant to the excimer Xe_2^* system (adapted from Ermler et al.[4]).

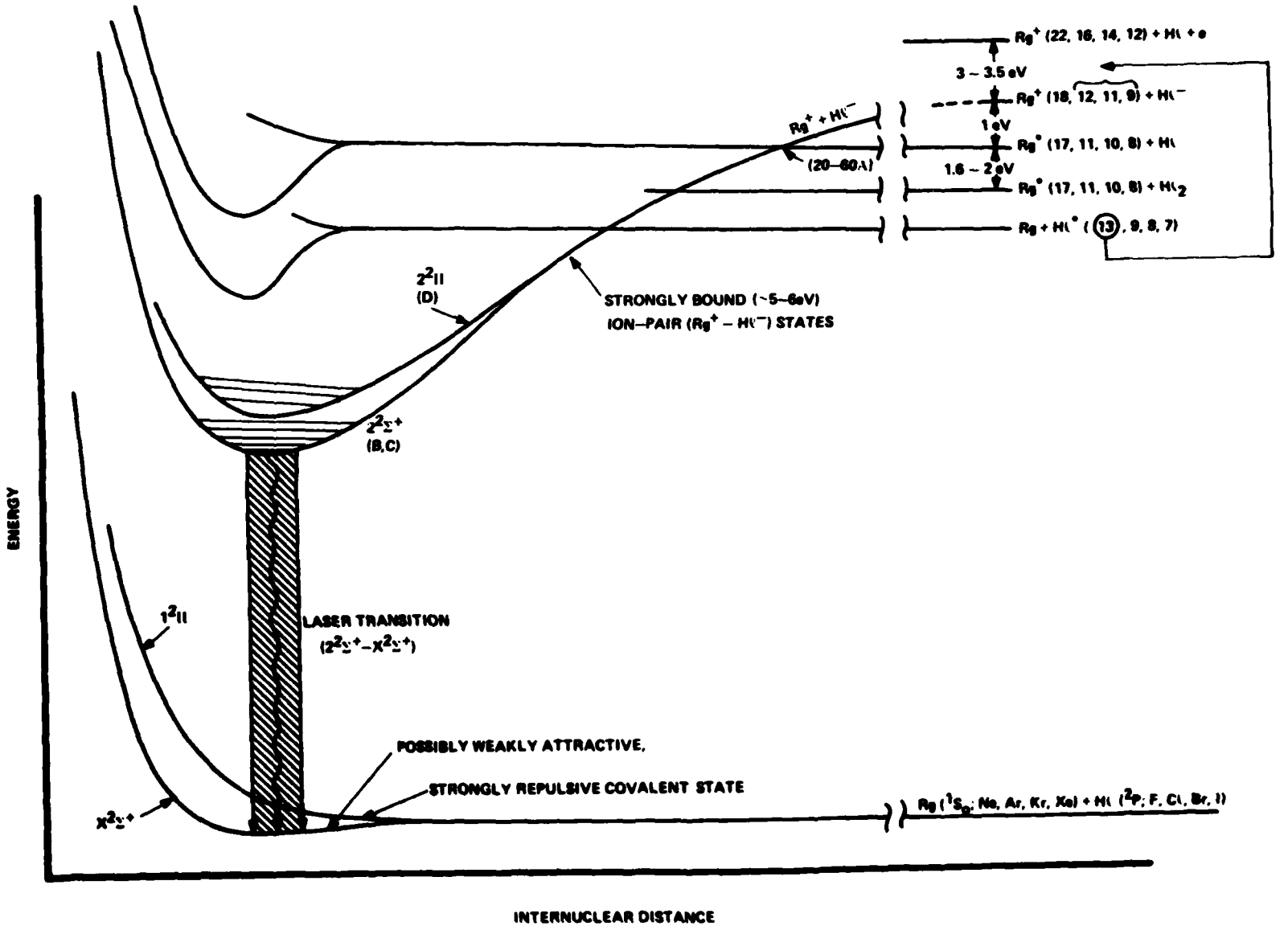

Figure 27. Schematic diagram of potential-energy curves relevant to the rare gas (Rg)-halide (Hℓ) systems.

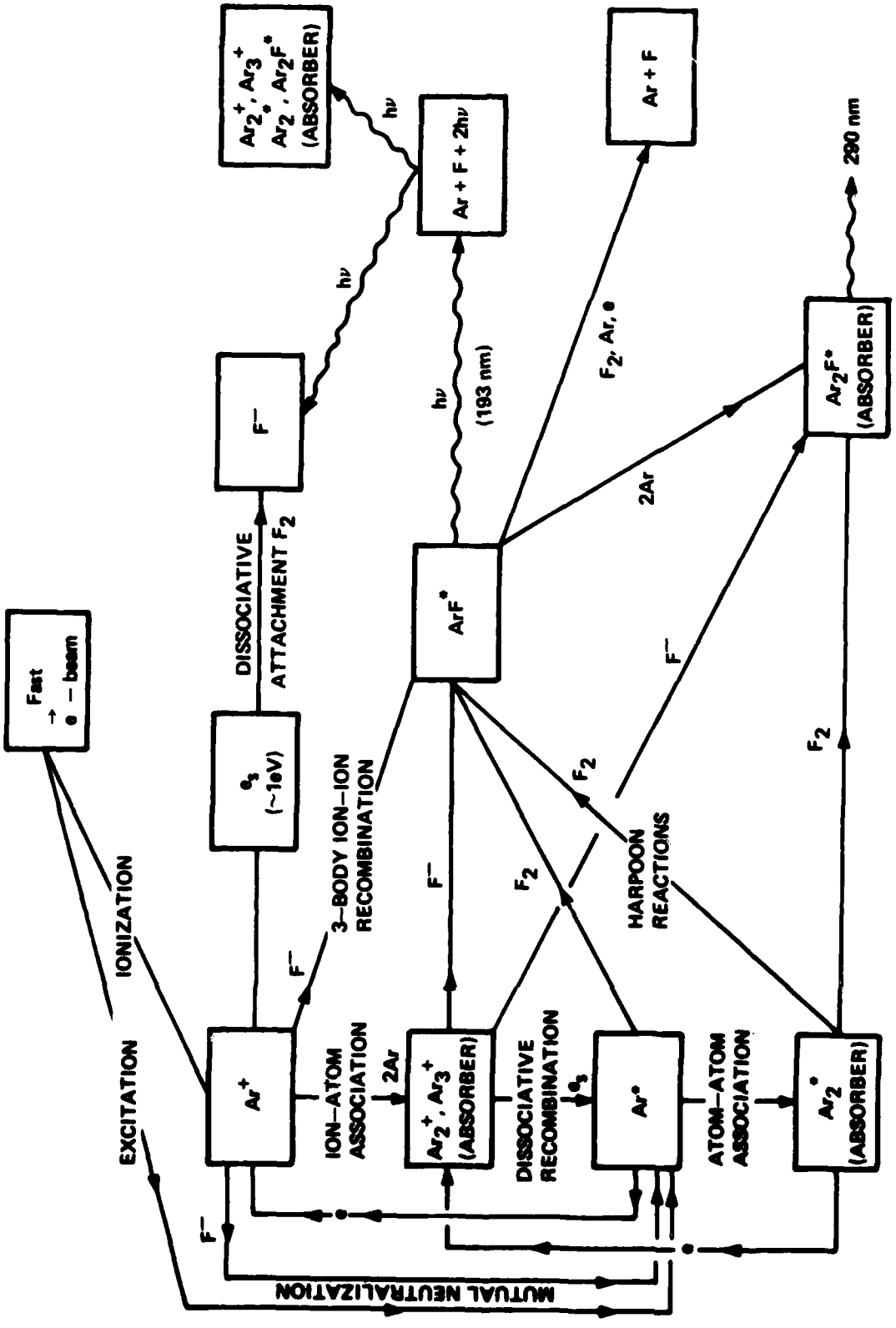

Figure 28. Dominant Mechanisms for production and quenching of ArF* in a typical e-beam excited two-component rare gas-halide system at pressures (1-4) atm.

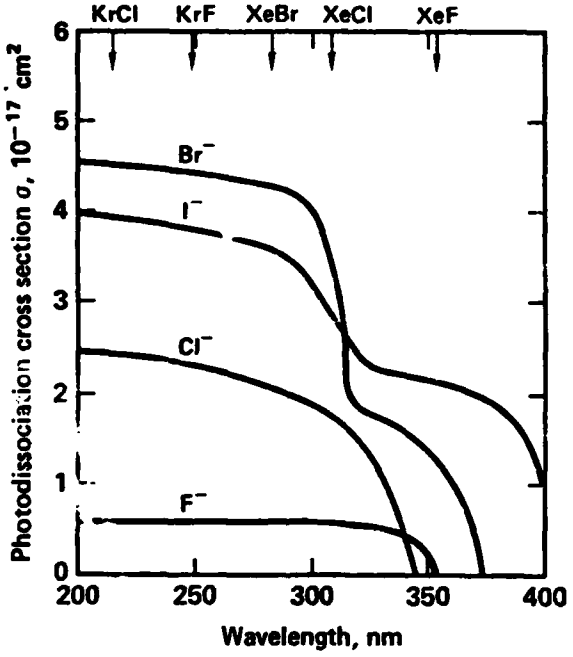

Figure 29. Cross sections for photodetachment of halide negative-ions (adapted by Ewing[1] from Mandl[12] and Roth[13]).

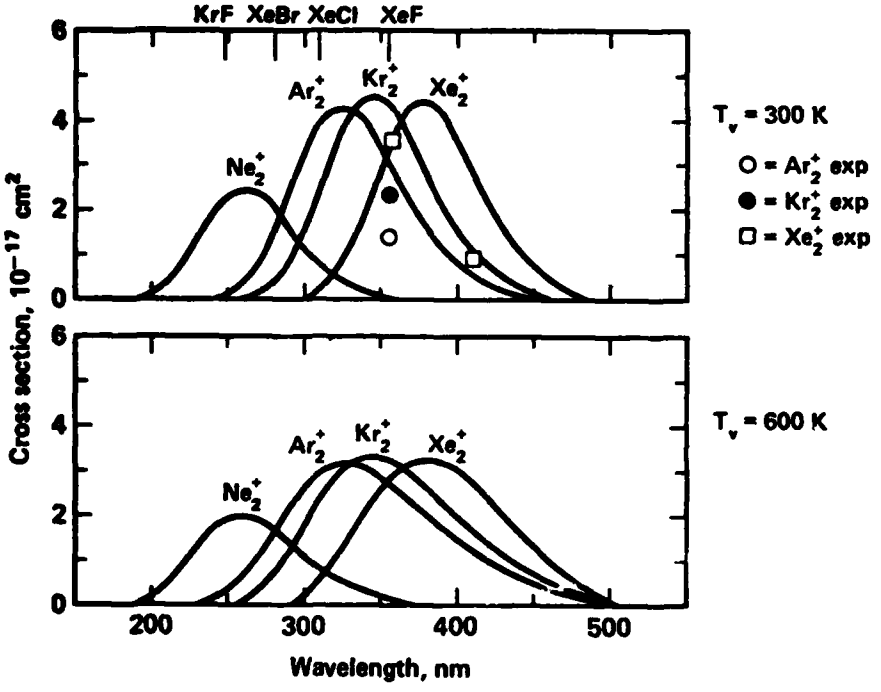

Figure 30. Photoabsorption cross sections of positive molecular ions Ne_2^+, Ar_2^+, Kr_2^+ and Xe_2^+ (adapted by Ewing[1] from Wadt and Hay[14]).

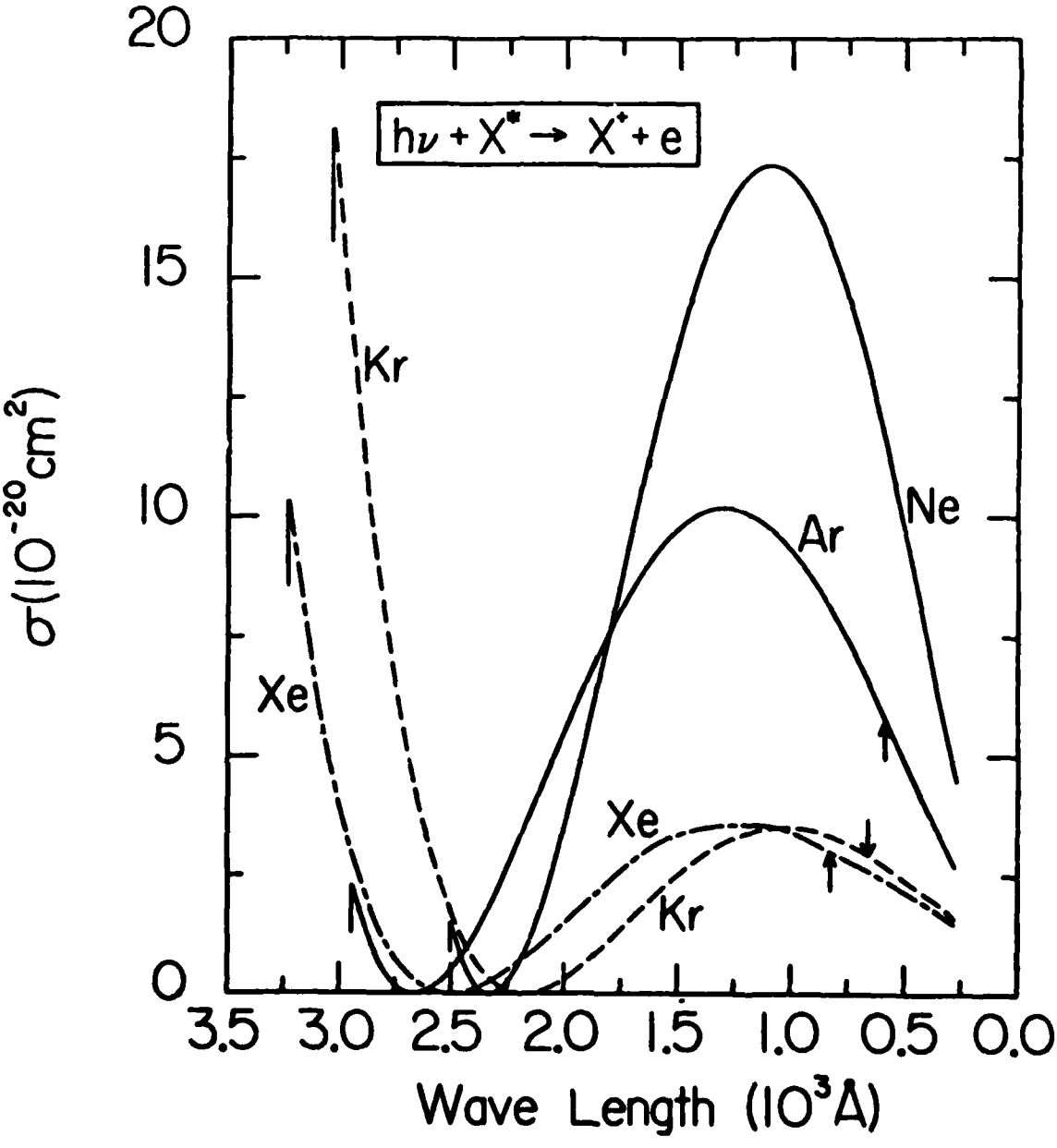

Figure 31. Cross sections for photoionization of metastable rare gas atoms Ne^*, Ar^*, Kr^* and Xe^* (after McCann and Flannery[15]).

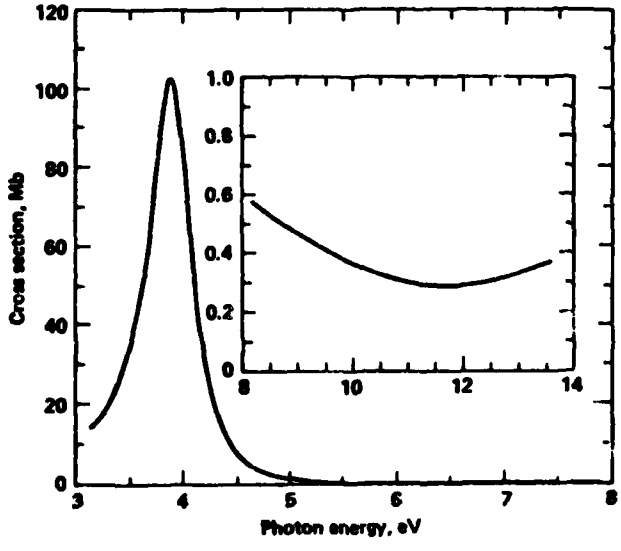

Figure 32. Cross sections for photoionization of the $^1\Sigma_u^+$ state of Ar_2^* (after Resigno et al.[16]).

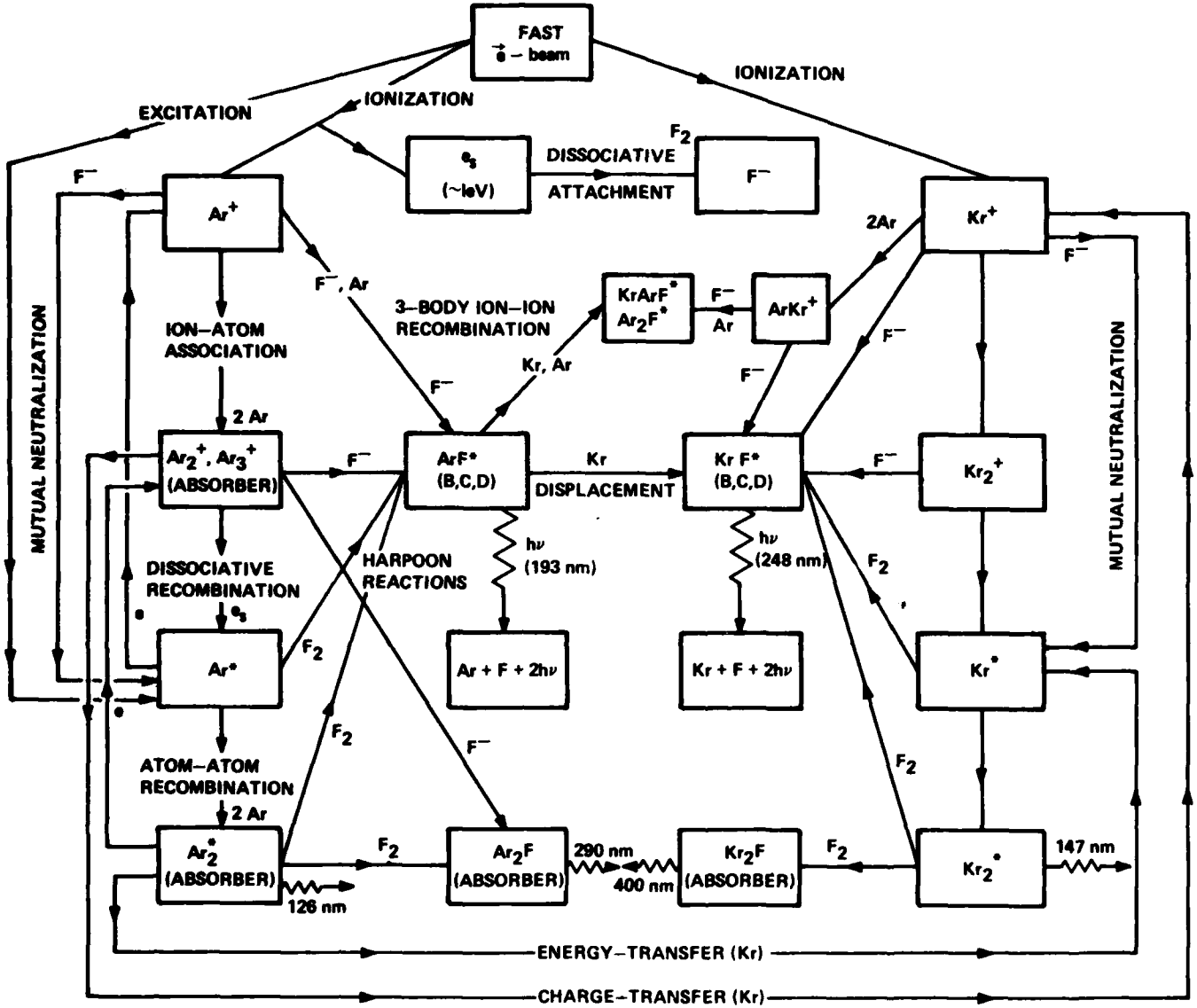

Figure 33. Dominant Mechanisms for KrF^* formation in $\vec{e}$-beam excited mixture (Ar > 90%/Kr < 10%/F_2 ∿ 0.2%) at pressures (1-4) atm.

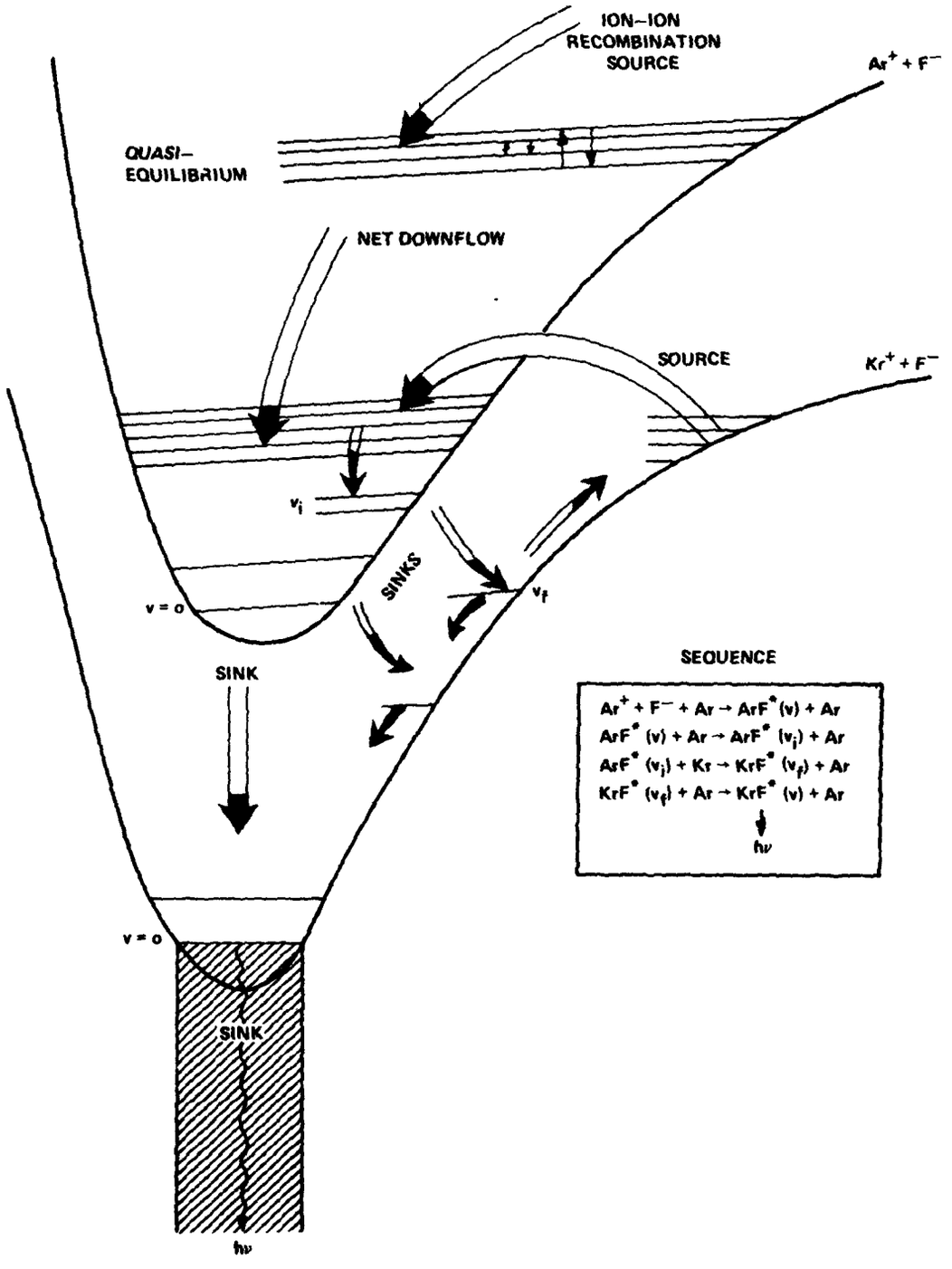

Figure 34. Schematic diagram illustrating vibrational relaxation and excitation with displacement reactions (after Flannery and Winter[17]).

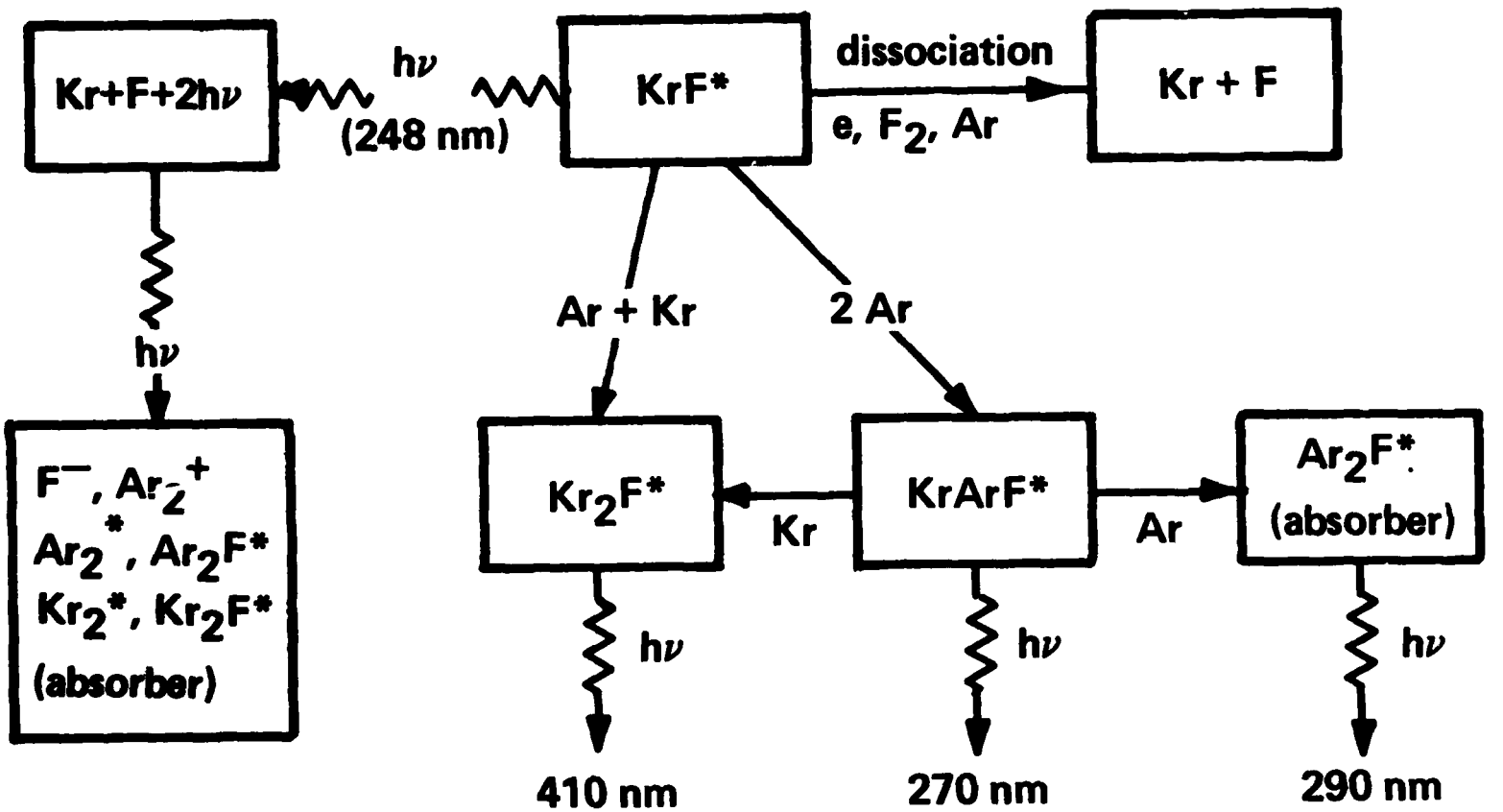

Figure 35. Dominant Mechanisms for KrF^* quenching in $\vec{e}$-beam excited mixtures ($Ar/Kr/F_2$) at pressures (1-4) atm.

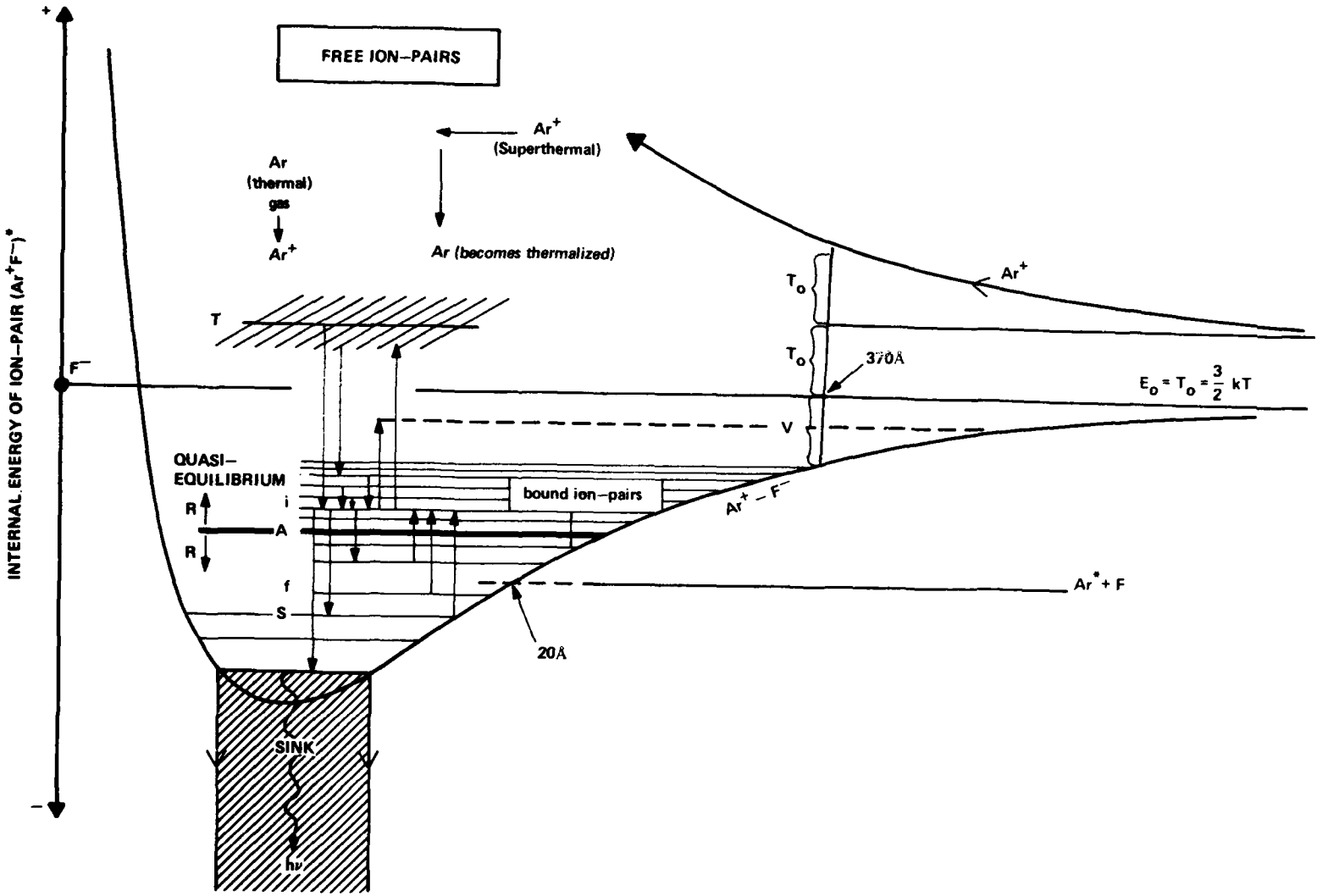

Figure 36. Schematic diagram illustrating the mechanism of ion-ion recombination into ArF^* and mutual neutralization to $Ar^* + F$ occurring in a gas.

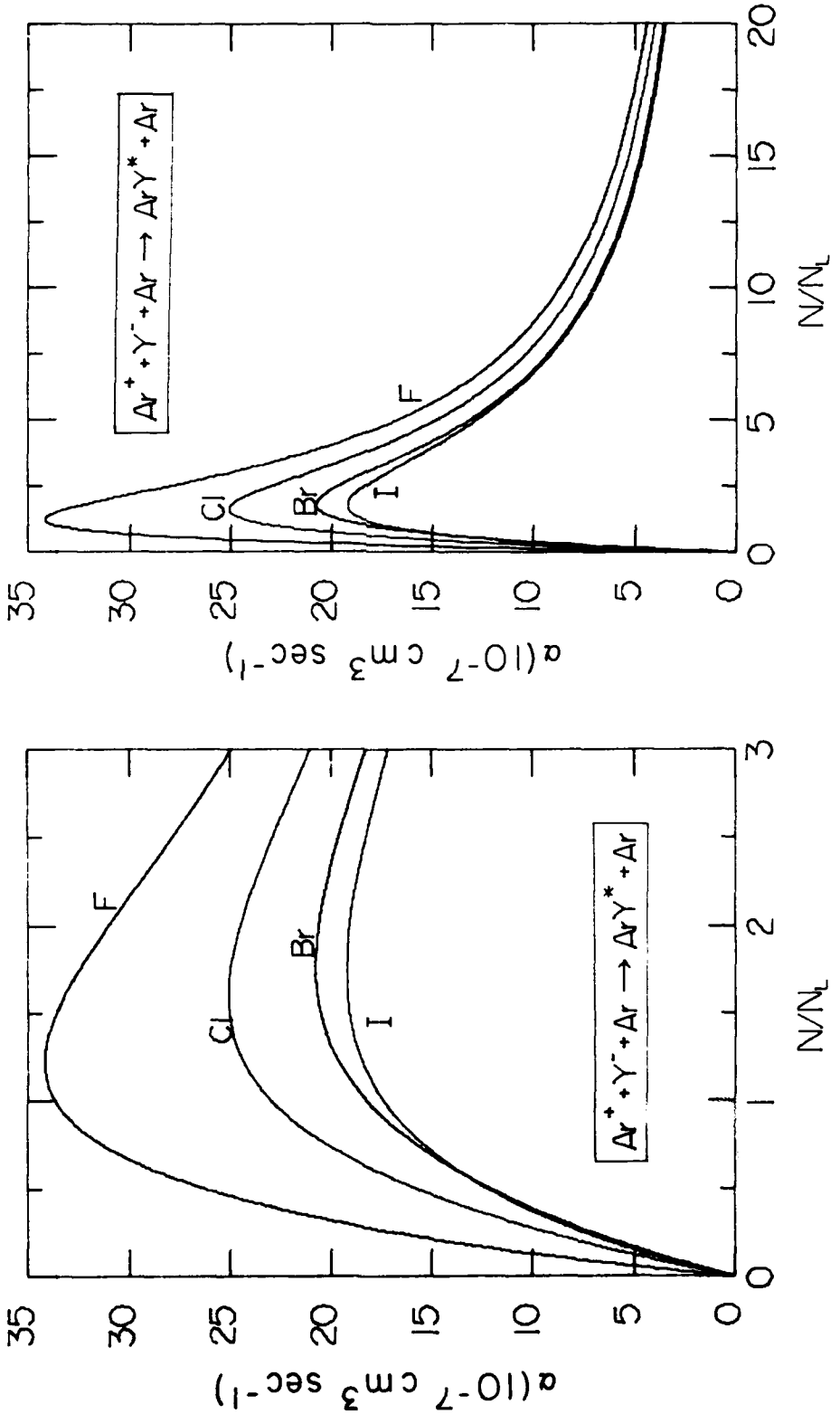

Figure 37. Three-body ion-ion recombination coefficients $\alpha(cm^3\ S^{-1})$ for $Ar^+ + Y^- + Ar \rightarrow ArY^* + Ar$, ($Y^- = F^-$, Cl^-, Br^-, I^-), as a function of neutral-gas density N (in units of Loschmidt's number $N_L = 2.69 \times 10^{19}$ cm^{-3}). Negative ion denoted in each curve (after Flannery[6]).

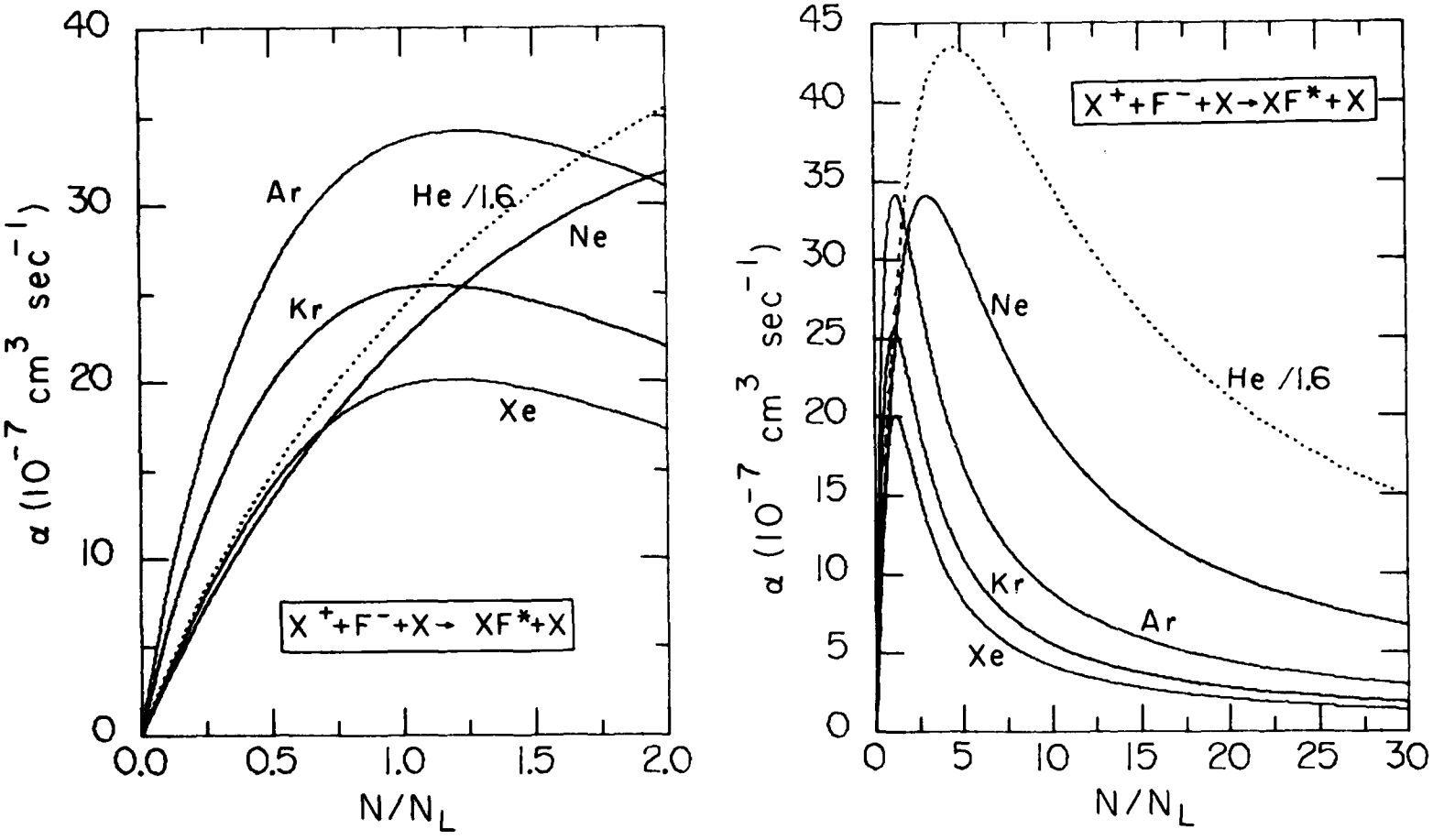

Figure 38. Ionic recombination coefficients $\alpha(cm^3\ sec^{-1})$ for the processes $X^+ + F^- + X \rightarrow XF^* + X(X \equiv He, Ne, Ar, Kr, Xe)$ as a function of neutral-gas density N (in units of Loschmidt's number N_L, $(2.69 \times 10^{19}\ cm^{-3})$. Gas X as indicated on each curve. Note the rates for the He case have been divided by 1.6. (After Flannery and Yang[7]).

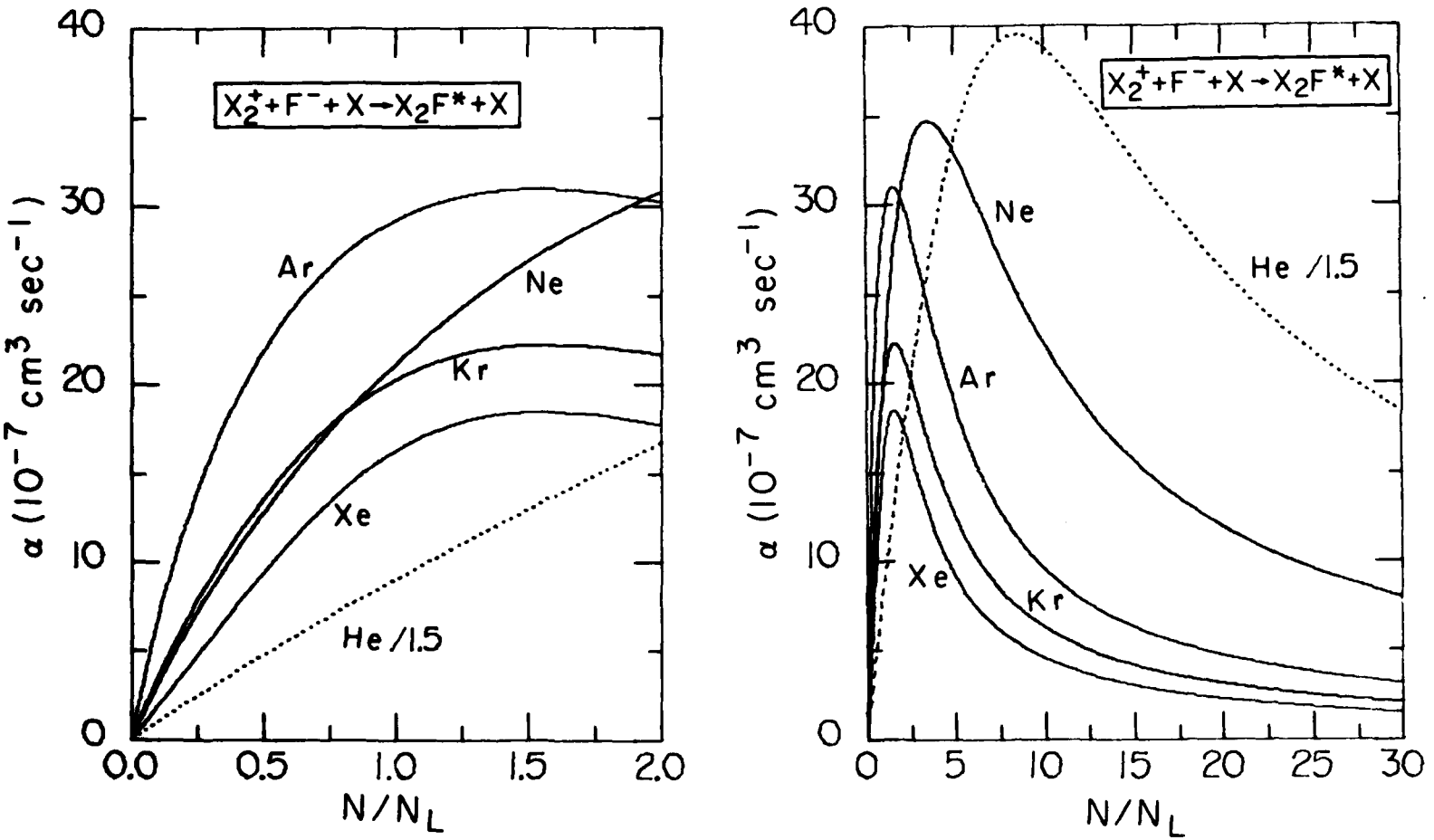

Figure 39. Ionic recombination coefficients $\alpha(cm^3\ sec^{-1})$ for the processes $X_2^+ + F^- + X \rightarrow [X_2F]^* + X$ (X ≡ He, Ne, Ar, Kr, Xe) as a function of neutral-gas density N (in units of Loschmidt's number N_L, $2.69 \times 10^{19}\ cm^{-3}$). The square brackets indicate that the molecule $[X_2F]^*$ may not remain bound. Gas X is as indicated on each curve. Note the rates for the He case have been divided by 1.5. (After Flannery and Yang[8]).

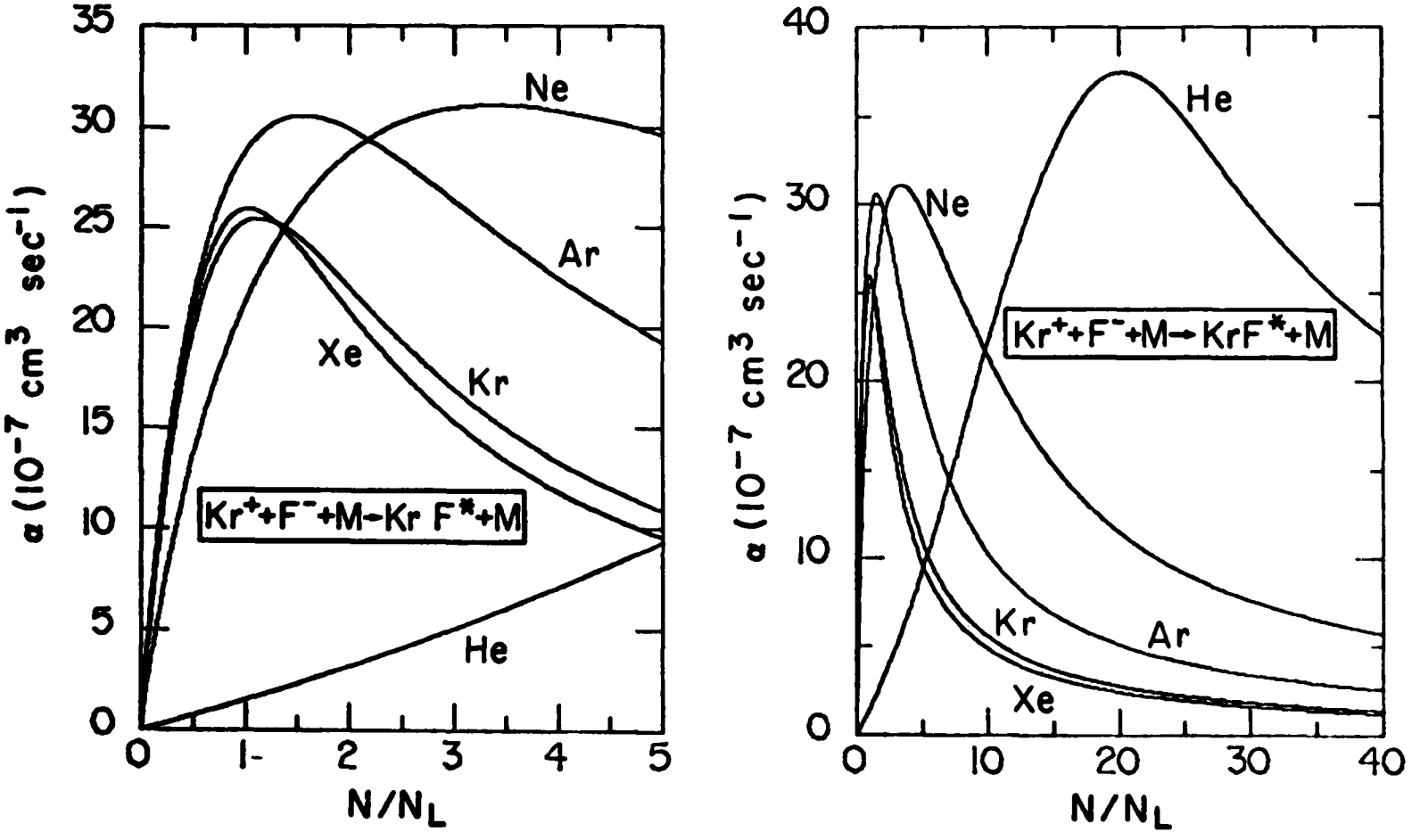

Figure 40. Ionic recombination coefficients $\alpha(cm^3\ sec^{-1})$ at 300 K for $Kr^+ + F^- + M \rightarrow KrF^* + M$ (M ≡ He, Ne, Ar, Kr, Xe) as a function of neutral-gas density N, in units of Loschmidt's number 2.69×10^9 cm^{-3}. Buffer gas M as indicated on each curve. (After Flannery and Yang[9]).

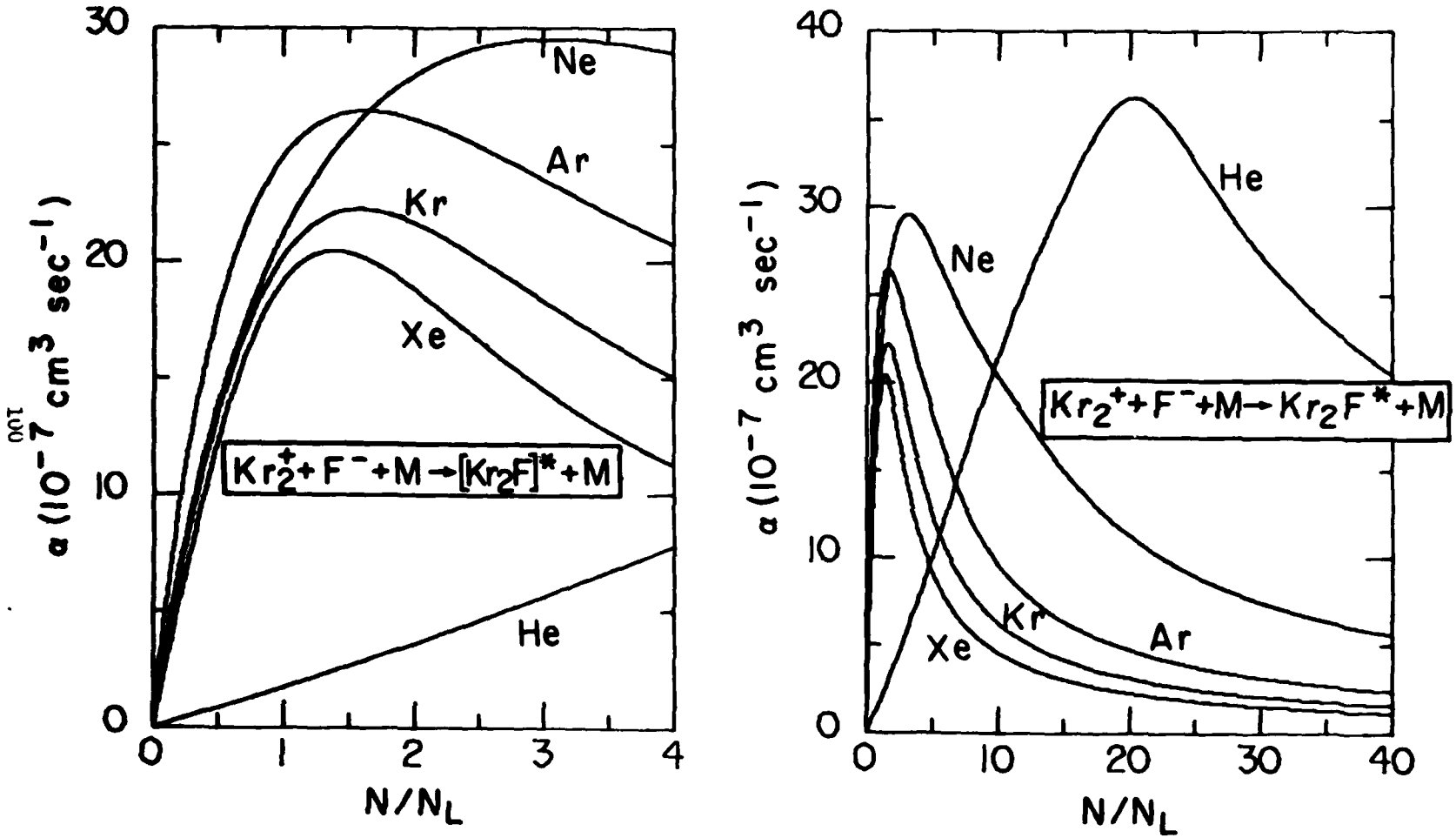

Figure 41. As in Fig. 15 except for the process $Kr_2^+ + F^- + M \rightarrow [Kr_2^+ F^-]^* + M$, where the brackets indicate that the product molecule may not remain bound. (After Flannery and Yang[9]).

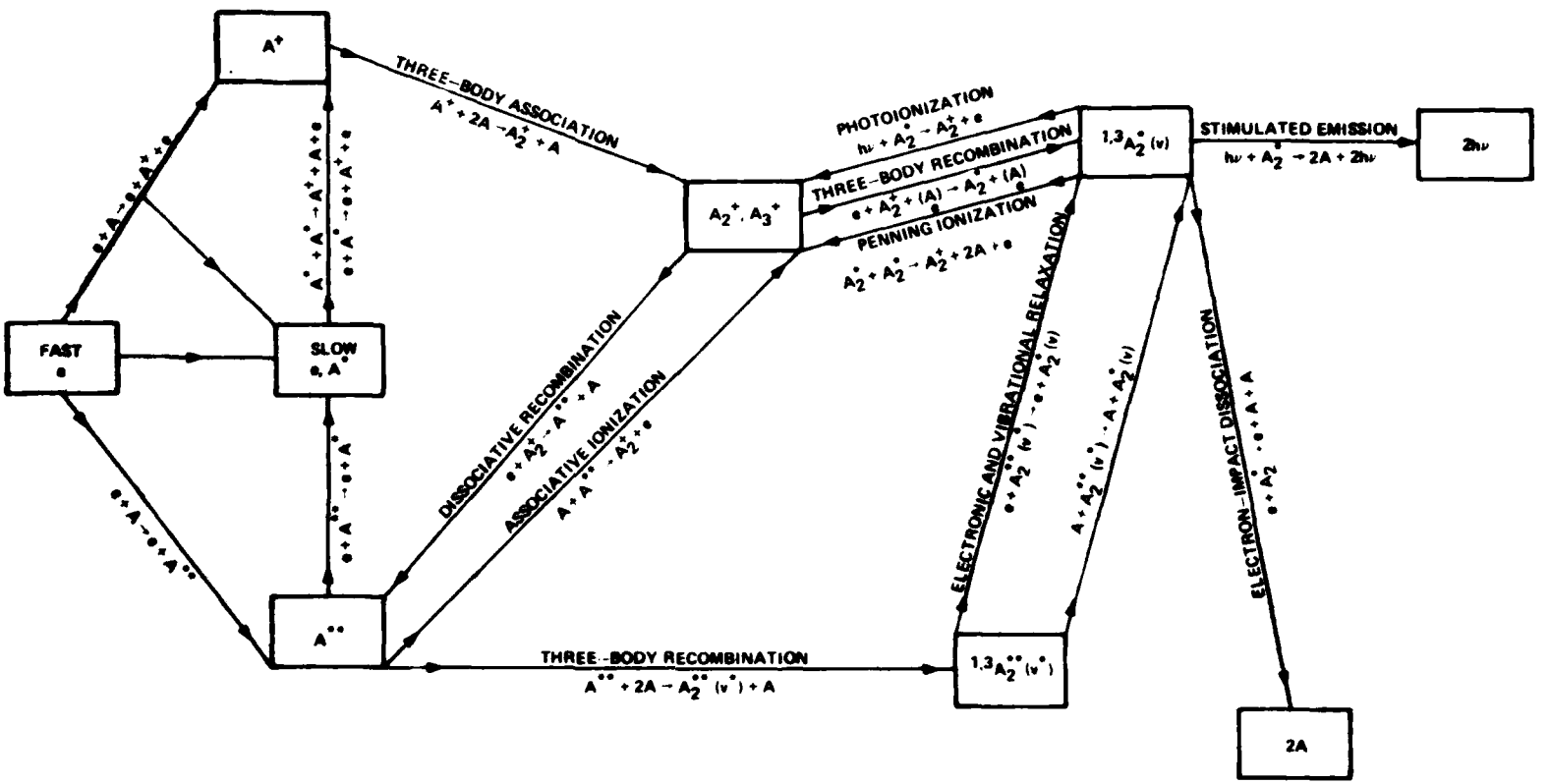

Figure 42. Atomic and Molecular processes important in the formation and destruction of rare gas excimers.

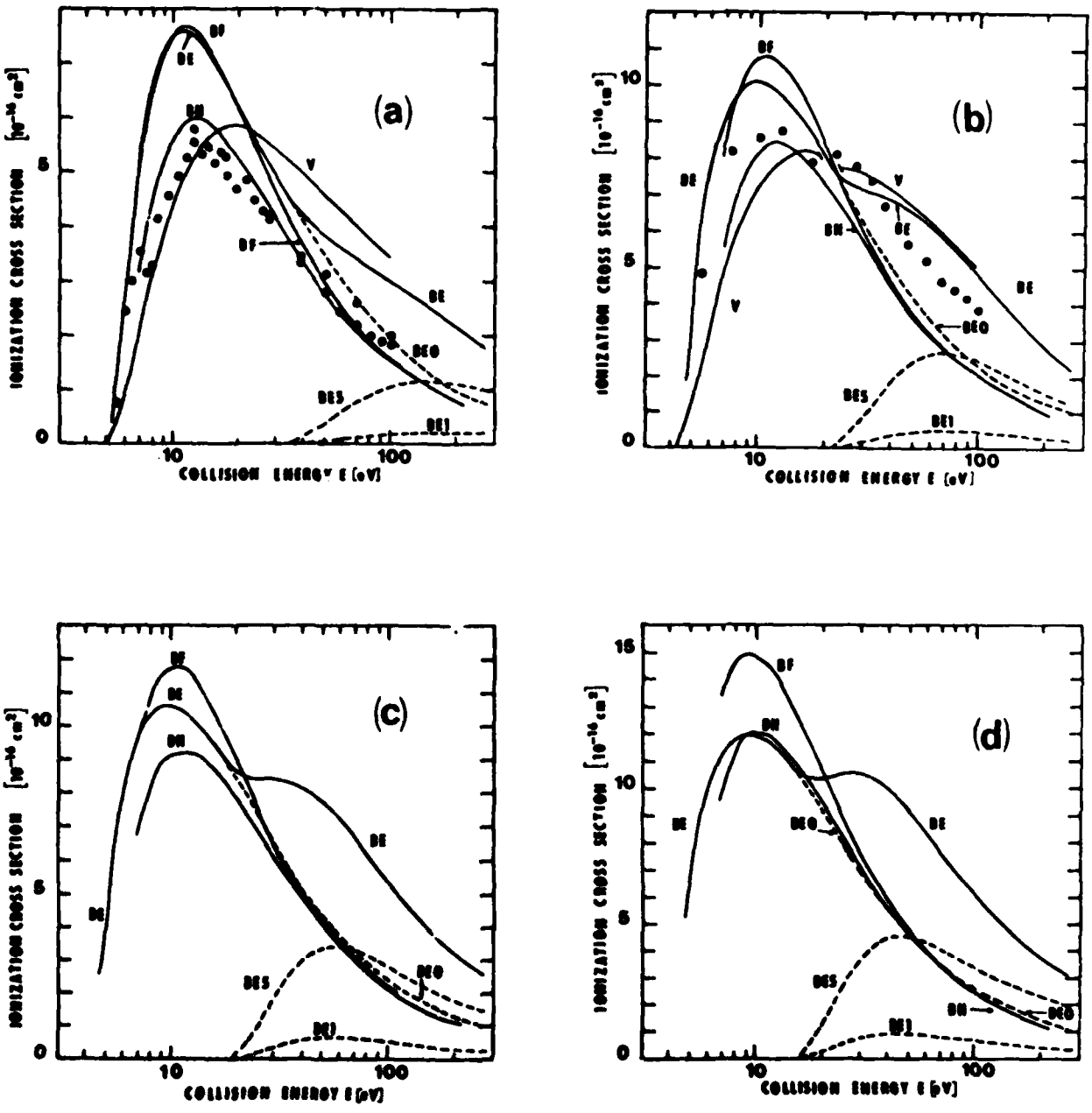

Figure 43. Cross sections (10^{-16} cm^2) for collisional ionization of metastable (a) Ne*, (b) Ar*, (c) Kr*, and (d) Xe* by electrons with impact energy E (eV). BF and BH are Born results for outer-shell ionization obtained from integrations over the full and lower-half ranges of energy ε of the ejected electron. The binary encounter (quantal distribution) cross sections are denoted by BEO for outer-shell ionization, by BE1 for ionization of one of the electrons in the np^5 shell, by BE5 for the total ionization of the np^5 shell and by BE for the sum of BEO and BE5. Previous binary encounter (exponential distribution) results of Vriens[30] are represented by V. ●: measurements of Dixon, Harrison, and Smith[31]. (After Ton-That and Flannery[18]).

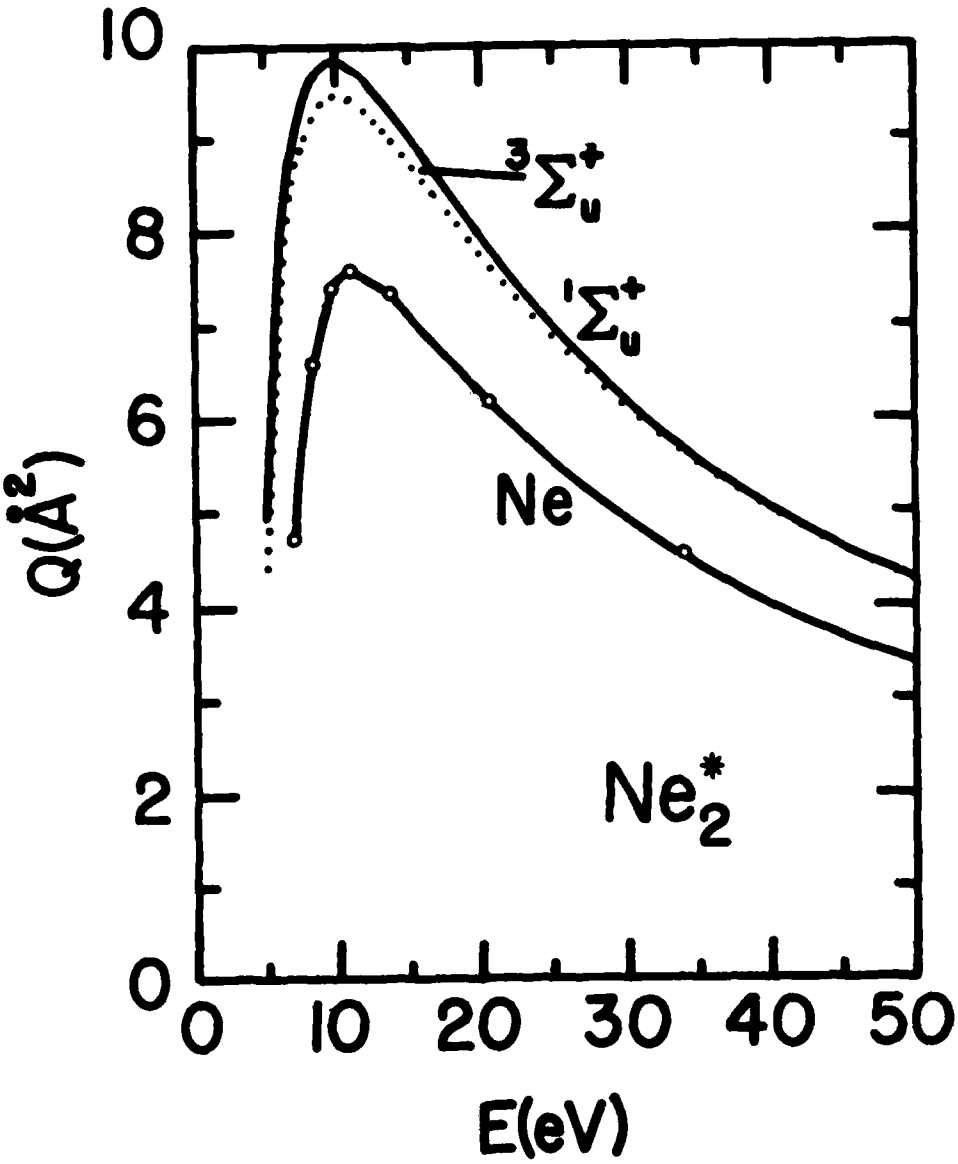

Figure 44. Cross sections for electron impact ionization of metastable ($^{1,3}\Sigma$) excimer states of Ne_2^*, and of the atomic metastable level. (After McCann, Flannery and Hazi[32]).

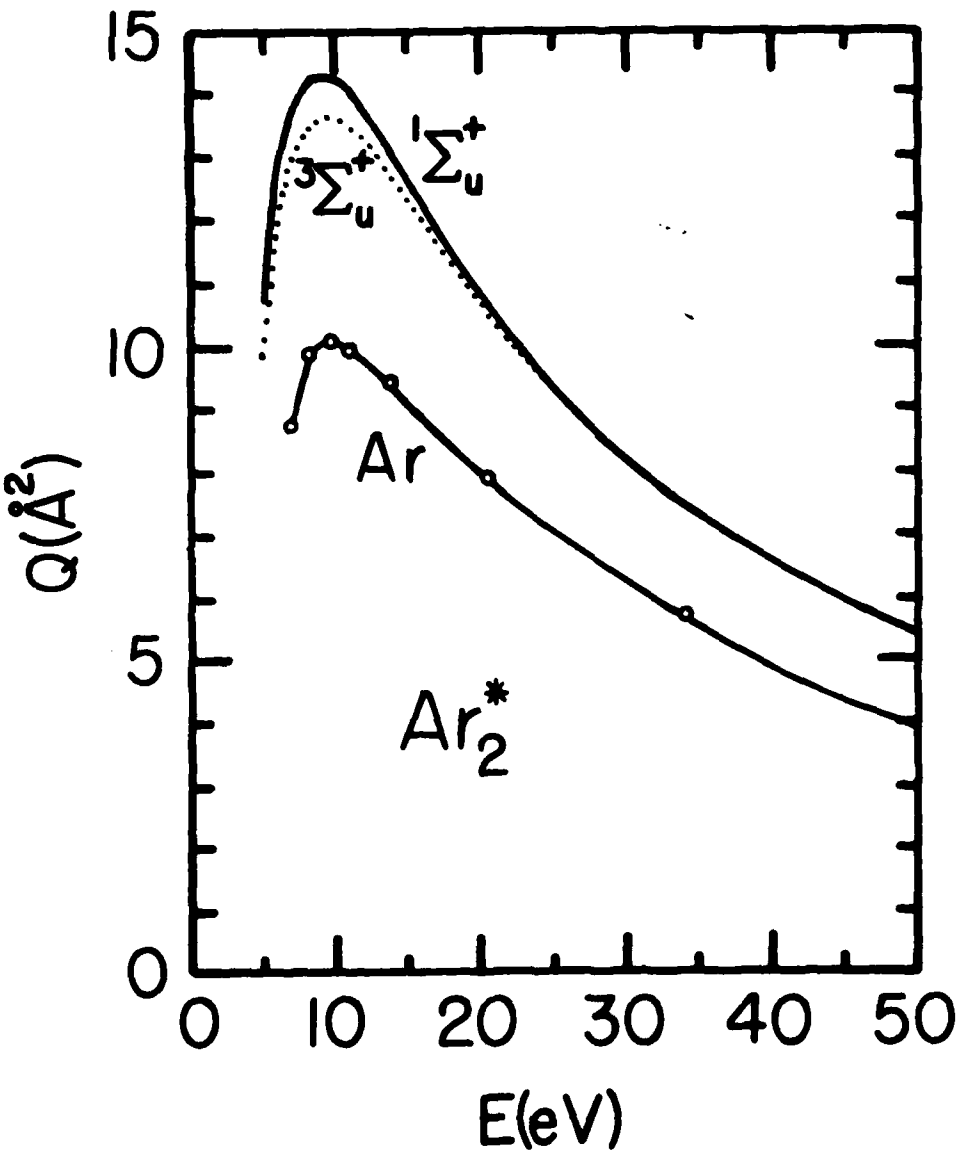

Figure 45. As in Fig. 19 except for Ar_2^* and Ar^* (after McCann, Flannery and Hazi[32]).

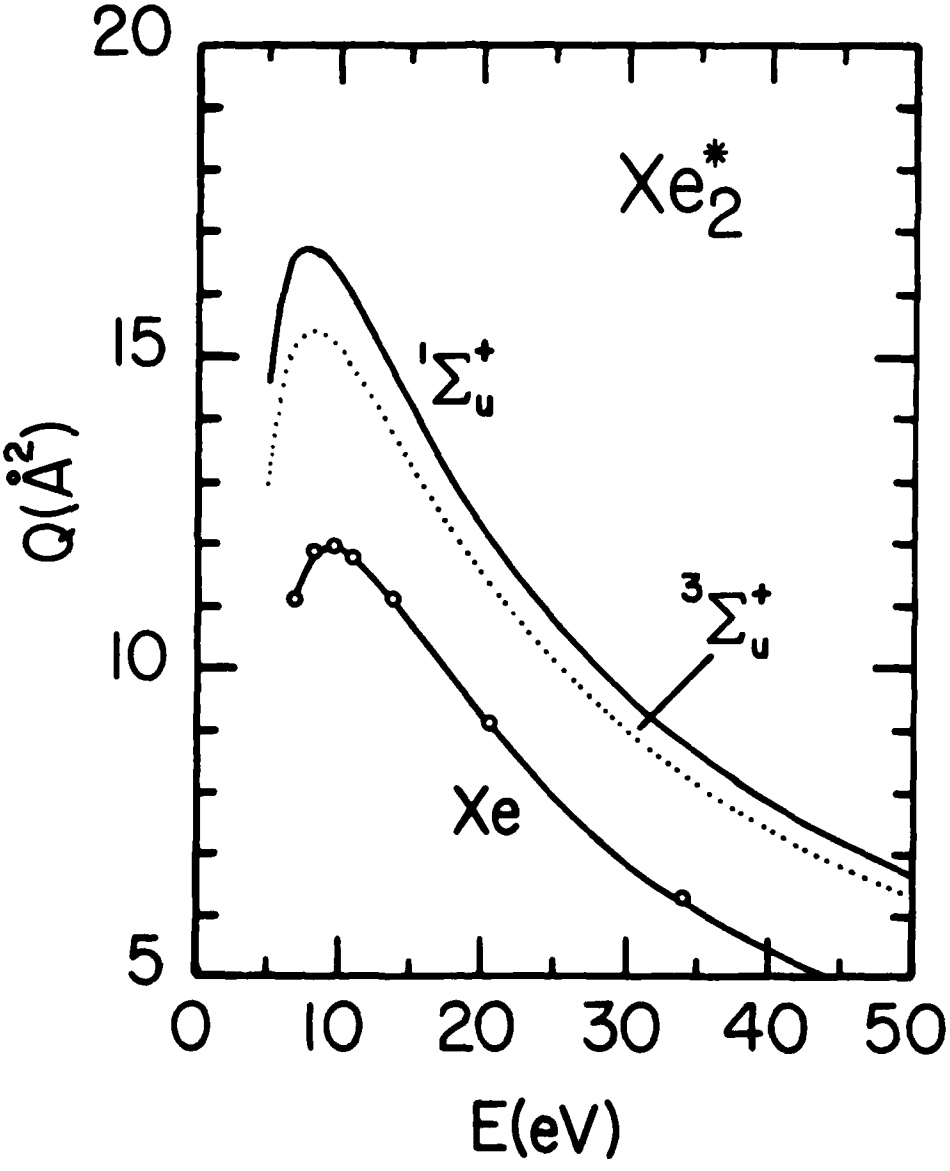

Figure 46. As in Fig. 20 except for Xe_2^* and Xe^* (after Flannery and McCann[33]).

References

1. "Compilation of Data Relevant to Rare Gas-Rare Gas and Rare Gas-Monohalide Excimer Lasers," E. W. McDaniel, M. R. Flannery, H. W. Ellis, F. L. Eisele, W. Pope, and T. G. Roberts, Technical Report H-78-1 (U.S. Army Missile Research and Development Command), Vol. I; pp. 1-427; Vol. 2; pp. 429-892.
2. "Compilation of Data Relevant to Nuclear Pumped Lasers," E. W. McDaniel, M. R. Flannery, E. W. Thomas, H. W. Ellis, K. J. McCann, S. T. Manson, J. W. Gallagher, J. R. Rumble, E. C. Beaty and T. G. Roberts, Technical Report H-78-1 (U.S. Army Missile Research and Development Command), Vol. III; pp. 893-1348; Vol. IV; pp. 1349-1916; Vol. V; pp. 1917-2401.
3. D. Ton-That and M. R. Flannery, Phys. Rev. A 15, 517 (1977).
4. L. Vriens, Case Studies in Atomic Collisions Physics I, edited by E. W. McDaniel and M. R. C. McDowell (North-Holland, Amsterdam, 1969), p. 337.
5. M. R. Flannery, J. Phys. B 4, 892 (1971).
6. H. F. Schafer III, The Electronic Structure of Atoms and Molecules (Addison-Wesley, Reading, Mass., 1972).
7. A. U. Hazi, T. N. Rescigno, A. E. Orel (unpublished).
8. T. N. Rescigno, A. U. Hazi, and A. E. Orel, J. Chem. Phys. 68, 5283 (1978).
9. W. C. Ermler, Y. S. Lee, K. S. Pitzer and N. W. Winter, J. Chem. Phys. 69, 976 (1978).
10. D. Ton-That, S. T. Manson, and M. R. Flannery, J. Phys. B 10, 621 (1977).
11. K. J. McCann, M. R. Flannery and A. Hazi, Appl. Phys. Letts. 34, 543 (1979).
12. Dupree, A. K., and Goldberg, L., 1970, Ann. Rev. Astron. Astrophys. 8, 231.
13. Flannery, M. R., 1970, Ann. Phys., New York 61, 465.
14. Flannery, M. R., 1971, J. Phys. B 4, 892.
15. Flannery, M. R., 1973, Ann. Phys., New York 79, 480.

16. Flannery, M. R., 1975, J. Phys. B 8, 2470.

17. Flannery, M. R., and McCann, K. J., 1975, Phys. Rev. A 12, 846.

18. Flannery, M. R., and McCann, K. J., 1979, J. Phys. B 12, 427.

19. Flannery, M. R., Morrison, W. F., and Richmond, B. L., 1975, J. Appl. Phys. 46, 1186.

20. Ton-That, D., and Flannery, M. R., 1976, Bull. Am. Phys. Soc. 21, 1247.

21. Ton-That, D., and Flannery, M. R., 1977a, Phys. Rev. A 15, 517.

22. Ton-That, D., and Flannery, M. R., 1977b, preprint.

23. Ton-That, D., Manson, S. T., and Flannery, M. R., 1977, J. Phys. B 10, 621.

24. For extensive bibliography and experimental details see J. J. Ewing in Excimer Lasers, Chapt. A 4, Laser Handbook edited by M. L. Stitch (North-Holland, Amsterdam, 1979); C. A. Brau, in Excimer Lasers edited by C. K. Rhodes (Springer, Berlin, to be published); C. W. Werner, E. V. George, P. W. Hoff and C. K. Rhodes, IEEE Journ. Quant. Electron. QE 13, 769 (1977).

25. E. W. McDaniel, M. R. Flannery, H. W. Ellis, F. L. Eisele, W. Pope, and T. G. Roberts, "Compilation of data relevant to rare gas-rare gas and rare gas-monohalide excimer lasers," Vols. I and II, 1978, Technical Report H-78-1, U.S. Army Missile Research and Development Command.

26. E. W. McDaniel, M. R. Flannery, E. W. Thomas, H. W. Ellis, K. J. McCann, S. T. Manson, J. W. Gallagher, J. R. Rumble, E. C. Beaty, and T. G. Roberts, "Compilation of data relevant to nuclear pumped lasers," Vols. III - V, 1979 (to be published).

27. W. C. Ermler, Y. S. Lee, K. S. Pitzer and N. W. Winter, J. Chem. Phys. 69, 976 (1978).

28. This subject has been reviewed by M. R. Flannery in Atomic Processes and Applications edited by P. G. Burke and B. L. Morseiwitsch (North Holland,

Amsterdam, 1976) Ch. 12; D. R. Bates in Case Studies in Atomic Physics edited by E. W. McDaniel and M. R. C. McDowell (North Holland, Amsterdam, 1974) Vol. 4, p. 57; B. H. Mahan in Advances in Chemical Physics, edited by I. Prigogine and S. A. Rice (Wiley, New York, 1973) Vol. 23, p. 1; M. R. Flannery in Case Studies in Atomic Physics edited by E. W. McDaniel and M. R. C. McDowell (North Holland, Amsterdam, 1972) Vol. 2, p. 1.

29. M. R. Flannery, Chem. Phys. Letts 56, 143 (1978).
30. M. R. Flannery and T. P. Yang, Appl. Phys. Letts. 32, 327 (1978).
31. M. R. Flannery and T. P. Yang, Appl. Phys. Letts. 32, 356 (1978).
32. M. R. Flannery and T. P. Yang, Appl. Phys. Letts. 33, 574 (1978).
33. M. Rokni, J. H. Jacob and J. A. Mangano, Phys. Rev. A 16, 2216 (1977).
34. M. Polanyi, Atomic Reactions (Williams and Norgate, London, 1932).
35. A. Mandl, Phys. Rev. A 3, 251 (1970).
36. D. E. Rothe, Phys. Rev. 177, 39 (1969).
37. W. R. Wadt and P. J. Hay, J. Chem. Phys. 68, 3850 (1978).
38. K. J. McCann and M. R. Flannery, Appl, Phys. Letts. 31, 599 (1977).
39. T. N. Rescigno, A. U. Hazi and A. E. Orel, J. Chem. Phys. 68, 5283 (1978).
40. M. R. Flannery and N. W. Winter, (in preparation).
41. D. Ton-That and M. R. Flannery, Phys. Rev. A 15, 517 (1977).
42. W. L. Nighan, Appl. Phys. Letts 32, 297 (1978); 32, 424 (1978).
43. D. R. Bates and Mendas, Proc. R. Soc. Lond. A 359, 287 (1978).
44. D. R. Bates, A. E. Kingston, and R. W. P. McWhirter, Proc. R. Soc. London A 267, 297 (1962).
45. D. R. Bates and R. J. Moffett, Proc. R. Soc. London A 291, 1 (1966).
46. D. R. Bates and M. R. Flannery, Proc. R. Soc. London A 302, 367 (1968).
47. M. R. Flannery and T. P. Yang (in preparation).
48. D. R. Bates and Mendas, Proc. R. Soc. London A 359, 275 (1978).

49. J. J. Thomson, Phil. Mag. 47, 337 (1924).

50. P. Langevin, Ann. de Chim. et de Phys. 28, 433 (1903).

51. D. R. Bates, J. Phys. B 8, 2722 (1975).

52. G. L. Natason, Sov. Phys.-Tech. Phys. 4, 1263 (1959).

53. L. Vriens, Phys. Lett. 8, 260 (1964).

54. A. J. Dixon, M. F. A. Harrison, and A. C. H. Smith, Abstracts of Papers of Eighth International Conference on the Physics of Electronic and Atomic Collisions, edited by B. C. Cobic and M. V. Kurepa (Institite of Physics, Belgrade, Yugoslavia, 1973), Vol. 1, p. 405; and private communication.

55. K. J. McCann, M. R. Flannery and A. Hazi, Appl. Phys. Letts. 34, 543 (1979).

56. M. R. Flannery and K. J. McCann, Appl. Phys. Letts. (in press).

*U.S.Government Printing Office: 1980 — 657-084/701

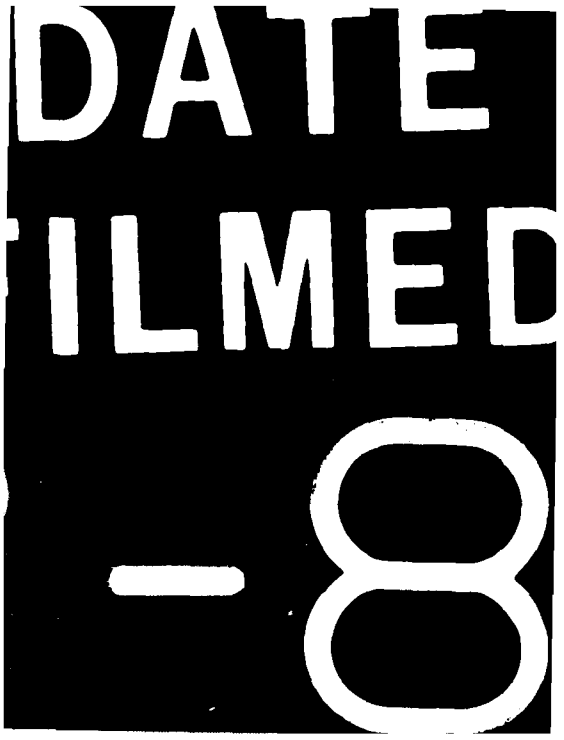
DATE
ILMED
-8